Analysis of the Sensing Region of a PZT Actuator-Sensor

by

Jaime Esteban

Dissertation submitted to the faculty of the

Virginia Polytechnic Institute and State University

in partial fulfillment of the requirements for the degree of

DOCTORATE

IN

MECHANICAL ENGINEERING

APPROVED:

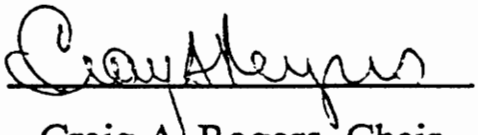

Craig A. Rogers, Chair

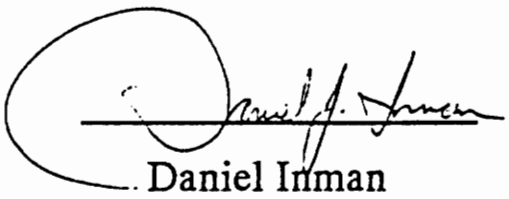

Daniel Inman

Mehdi Amadian

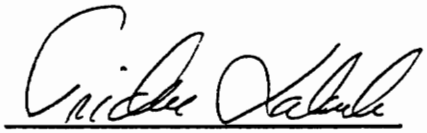

Frederic Lalande

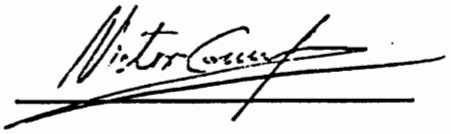

Victor Giurgiutiu

July, 1996

Blacksburg, Virginia

Keywords: NDE, PZT, joints, high frequency

ANALYSIS OF THE SENSING REGION OF A PZT ACTUATOR-SENSOR

by

Jaime Esteban

Committee Chairman: Dr. Craig A. Rogers

Mechanical Engineering

(ABSTRACT)

A high frequency impedance-based qualitative non-destructive evaluation (NDE) technique has been successfully applied for structural health monitoring at the Center for Intelligent Material Systems and Structures (CIMSS) [1-3]. This new technique uses piezoceramic (PZT) patches as actuator-sensors to provide a low-power driven constant voltage dynamic excitation, and to record the modulated current flow through the structure. Therefore, it relies on tracking the electrical point impedance to identify incipient level damage. The high frequency excitation provided by the PZT, ensures the detection of minor changes in the monitored structure. It also limits the sensing area to a region close to the PZT source, therefore only changes in the near field of the PZT are detected, enhancing the ability of this technique to localize incipient damage.

The phenomena of the PZT's sensing region localization has been the driving motivation for this research. More fundamental analytical research should be performed before full application of this technique is possible. Thereby, a wave propagation continuum mechanics based approach has been applied to model the high frequency vibrations of one dimensional structures. Energy dissipation mechanisms, such as bolted connections and internal friction, are considered to have a major role in the attenuation of the PZT's induced wave, therefore these mechanisms has been extensively studied.

To analyzed bolted connections, linear and nonlinear joint models have been used to describe the wave interaction with such nonconservative discontinuities. Also, with the use of an impedance based model, the electromechanical coupling of the PZT and the host structure is added into the formulation. The wave interaction and energy dissipated at the bolted discontinuity has been assessed with energy flux computations of the incident, transmitted, and reflected waves. The effect of loosening the bolted joint has been also analyzed by reducing the spring stiffness and increasing the damping in the dash pots for the linear joint model, and reducing the Coulomb stiffness and shearing force at the interface for the nonlinear case.

A scheme based on the correspondence principle has been applied to calculate the specific damping capacity of a system, at any given frequency, as a quantification of the energy dissipated through the system. The material damping was added into the formulation assuming the modulus to have a complex representation, and therefore the corresponding loss factors were found with active measurement of the material properties of the specimen via a wave propagation method, that monitories the wave's speed at two locations.

Once the bases of the analytical model have been set up and corroborated with experiments, a parametric study has been developed to account for the various factors that can affect the sensing range of the PZT's induced wave, and therefore to have a "rule of thumb on how to go about" when bonding PZTs to structures to monitor them. Apart from the energy dissipation mechanisms, other parameters responsible for the reflection of the incoming wave, and its consequent attenuation, has also been reconstructed. With the extensive analysis of these parameters, an impedance damage metric, based on the undamaged and damaged impedance, has been developed for various factors that can be the source of incipient damage. An attenuation metric has also been introduced to identify the degree of transmission of the propagating wave at certain discontinuities. The analysis

of the case scenarios reproduced in this parametric study will aid in the knowledge about the number of PZTs needed to be placed in the monitored structure, the most critical locations, and when a monitored member in a system need to be replaced.

Acknowledgments

I would like to acknowledge Dr. Rogers and all my committee members for their help, advice and time, with a special appreciation to Dr. Lalande. I will also like to acknowledge the help provided by Dr. Chaudhry for his comments at the early stage of my research.

A very special thank to all my friends and the staff at CIMSS, for making my work so enjoyable.

I would also like to gratefully acknowledge the funding support of the National Science Foundation.

But, above all, thank you Ruth.

Table of Contents

List of Figures

List of Tables

Chapter 1

Introduction

1.1 *Motivation*

A new health monitoring technique capable of in-situ on-line incipient damage detection in complex structures is under investigation at the Center for Intelligent Material Systems and Structures (CIMSS) [1-3]. The basic concept of this qualitative non-destructive evaluation (NDE) technique is to monitor the variations in the structural mechanical impedance caused by the presence of incipient damage in the structure. If damage like cracks, corrosion, debonding, or loose connections are present in the structure, the structural mechanical impedance will be modified. By integrating the measured impedance variations over a dynamically active frequency band, a scalar damage metric is obtained, and damage is detected when the damage metric reaches a predetermined threshold value. The problem with this approach is that structural mechanical impedance measurements can be difficult to obtain. In this NDE technique, this problem is solved by measuring the electrical impedance of a low power driven piezoceramic (PZT) actuator-sensor bonded on a complex structure. Because of the electromechanical coupling property of piezoelectric materials, the measured electrical impedance is directly related to the mechanical impedance, and will also be affected by the presence of damage. This NDE technique has been applied to several complex structures successfully. In order to ensure high sensitivity to incipient damage; the electrical impedance is measured at high frequencies, at which the wave lengths are shorter than the damage to be detected.

It has been shown that the sensing area is localized to a region close to the PZT actuator-sensor, therefore enhancing the ability of this technique to detect damage without

being affected by far field boundary conditions, external loading, or normal operational vibrations of the system. This localization phenomena has only been observed experimentally, and it was attributed to energy dissipation and multiple reflections of the PZT's induced wave in the system at high frequency. Even though this new NDE technique has been shown to be very performant, more fundamental research is needed before a broad use of the technique is possible. The fundamental research to be performed is geared towards a better understanding of the energy dissipation and reflections that occur in structures at high frequency.

1.2 *Objectives*

The localization of the actuation-sensing area of the collocated PZT is due primarily to energy dissipation mechanisms, such as nonconservative joint discontinuities and material damping in the structure. Since the excitation is at high frequency, the effect of these mechanisms on the attenuation of the PZT's induced wave, is further magnified. Also, very significant attenuation of the propagating wave is brought about by structural discontinuities acting as sources of multiple reflections. The aim of this research is to investigate the various parameters responsible for the wave localization phenomena, in order to have a better understanding on the sensing region of a PZT actuator-sensor bonded to a structure for qualitative health monitoring. For this purpose, an analytical procedure will be developed to model the high frequency dynamics of one dimensional structures, accommodating for the electromechanical coupling of the PZT-structure and the various attenuation mechanisms responsible for the wave's attenuation.

With this modeling effort, a better understanding of the various energy dissipation and reflection based factors needed to be most closely considered when attaching the PZT patches to real structures, for health integrity purposes, will be attained. The study of these factors will aid to understand the structural dynamic behavior recorded by the PZT actuator-sensor under real field conditions, and therefore to have a better insight of the critical areas needed to be more closely inspected in the monitored structure, as well as the

elaboration of an impedance damage metric that can be used to asses the level of damage in the structure.

1.3 *Dissertation Organization*

This dissertation is a collection of papers presented, and to be submitted, at various conferences, focusing on intelligent material systems and structures. Because of this layout, the reader will find repetitions on some of the chapters. The dissertation begins with a review on the different areas that will be expose in this research. The work previously done on these areas will be supplemented with the new findings added into the literature after the completion of the work here presented.

Then, a preliminary model of high frequency vibrations of one-dimensional structures is done with the use of a wave propagation approach, based on continuum mechanics, to derive the dynamic stiffness matrix that contains the inertial, stiffness and damping properties of the structure. This analytical procedure is enriched with an electromechanical coupling of the PZT's impedance-based model to relate mechanical calculations with electrical readings. Also, linear and nonlinear models of bolted joints has been added into the formulation to describe its dynamics and to study its influence on the attenuation of the propagating wave. With this analytical procedure, an implicit function, describing the dynamics of a structure, is implemented to obtain the specific damping capacity of a system, as well as the interaction of the propagating wave at dissipative discontinuities through measurements of its energy flux. To complete this work, a parametric study on the various factors to consider when attaching PZT actuator-sensors to a structure, for health monitoring purposes, will follow.

Chapter 2

Literature Review

2.1 *Non-Destructive Evaluation Techniques*

The use of vibration pattern information for nondestructive evaluation (NDE) is a field of increasing interest. A brief description of some of the approaches to the vibration based health monitoring techniques will follow.

An extensive effort has been applied to detect changes in the dynamics of a structure by examining the vibration signatures of the response using a modal-analysis approach and therefore looking at the natural frequencies and mode shapes [4]. Damage produces a decrease in the stiffness coupled with an increase in damping [5]. Since the stress distribution along the structure is different for each natural frequency, any macroscopic damage would affect each mode differently depending on the location of the damage [6]. In Reference [7] the authors use a time-domain identification approach to create a mathematical model from recorded measurements and then compared this to an undamaged model. Another method [8] uses a modal parameter identification technique and the system response to observe damage at a macroscopic level. Reference [9] takes an experimental approach using measured mass and stiffness matrices from modal parameters to observe damage on a structure without any analytical model. Another experimental modal analysis based technique has been implemented to the dynamic analysis of cracked beams [10].

A technique using a laser doppler vibrometer and an interferometer to create a modal analysis scheme and obtain the response at high frequencies (upto 10 kHz) was developed by Nokes and Cloud [11]. Increasing the excitation frequency used to evaluate

the dynamics of the monitored structure, enhances the ability for this technique to localize internal damage.

Detection of cracks in structures have been elegantly tackled by using a wave propagation approach [12]. The structure is impacted using a force transducer at a frequency less than 10 kHz, and the presence of a crack is detected by changes in the structural stiffness, which is obtained from a spectral model of the structural response. This analytical tool uses a finite element post processor in which the exact equations of motion are used to reconstruct the dynamic stiffness of the system.

Another approach for NDE and damage location independent of modal information, has recently been presented by Banks et al. [13], where changes in stiffness are detected by using the time histories of the input and vibration response of the structure. These variations in stiffness properties will correspond to alterations or damage on the structure.

Other techniques that use transducers to both send and received waves are ultrasonic detection and ultrasonic imaging [14-16]. Most of the work done in this area has been on nondispersive waves (such as ultrasonic surface waves), which show no change in shape as they propagate and can be used to detect flaws at remote sensing locations. Generally, waves in structures are dispersive, which means that different frequency components travel at different speeds. The research done on dispersive waves using this technique is very narrow and with some limitations when there are multiple reflections, as the ones encountered with multiple joints in structures [17].

An efficient method for qualitative health monitoring of structures, that uses piezoceramic (PZT) actuator-sensors to detect incipient level damage [1-3], has been developed at the Center of Intelligent Material Systems and Structures, and introduced in chapter 1. The PZT patch is bonded to the structure and wired to an impedance analyzer, which feeds a constant voltage to the low-power driven PZT actuator-sensor and

measures the electrical impedance of the PZT, coupled with the mechanical impedance of the structure. Measurements are first recorded for the healthy structure, any alteration due to damage in the configuration of the system will change the impedance measurements, and damage will be measured on a metric scale. Using piezoceramic elements as actuator-sensors is a great alternative for NDE of complex structures, and due to their compactness and easy applicability, offers a clean method to use for in-situ health monitoring.

2.2 *Modeling of Joints*

The damping capacity of a bolted joint is an important parameter in the calculation of the dynamic behavior of structures, but some difficulties have been experienced with their analysis because the forces occurring at the matting section are nonlinear and therefore mathematically difficult to describe. Much attention has been given to the capability of a structure to dissipate vibratory energy and to establish the levels of the structural response to excitation. Several authors [18-24] have explained the damping occurring in such joints by the analysis of friction damping influenced by interfacial pressure. Depending on the tightness of the bolts at the joint, the friction or slip damping is classified as [18]:

- Macro-slip: Occurs at low clamping pressures, and Coulomb's law of friction is assumed valid;
- Micro-slip: At increasing bolt pressure, very small displacements take place and roughness appears relative to the matting surfaces;
- Plastic-deformation: Extremely high clamping pressure causes plastic deformations of the roughness.

The energy dissipation arising from the relative motion of the matting surfaces is influenced by the clamping pressure. At relatively low clamping pressures, Coulomb's law of friction holds, but as the pressure is increased, microslip is initiated. At this stage the losses occurring are very small and difficult to measure. In this study, only work at the

macroscopic level will be considered because it carries the greatest energy dissipation potential. Masuko et al. [21] studied the damping capacity of a jointed cantilever beam with the inclusion of the microslip to calculate the energy loss. Earles [20] concluded that the damping capacity is maximum when force transference is only by friction for any pressure distribution imposed in the bolts. An analysis to observe the rate of energy dissipated in a lap joint, done by Metherell et al. [23], showed an important discrepancy from the linear behavior.

Due to the difficulties that arise when micro-slip behavior is taken into consideration and the inherit nonlinear response of the system having dry friction, most of the work done on the modeling of energy dissipation considers macro-slip friction and solves the nonlinear problem by either linearization techniques or by equivalent linear systems. A first single degree of freedom model proposed by Den-Hartog [24], studied the stick-slip behavior of the dry friction at the contact surface with at most two time intervals of no relative motion (lock-ups) per cycle. Other authors extended the work by Den-Hartog [25-28]. Among them, Pratt et al. [27] studied the multiple lock-ups per cycle possible in the motion of two masses with dry friction, and they obtained an equivalent viscous system which dissipates the same amount of energy per cycle. Also, Ferri et al. [25] studied dry friction damping with three models having different types of damping characteristics, and they showed that it is possible for such systems to exhibit viscous damping properties. An extensive study of nonlinearities in structures is given by Crandall [26] who included relations of the friction force as a function of slip velocity and of rods connected by pins having clearance fit nonlinearity. Initially, Menq et al. [28] presented a method for approximating the response of frictionally damped structures with the use of finite element analysis, and a harmonic Fourier expansion of the nonlinear friction force solved in a separate algorithm.

Many methods are widely used for approximating the frequency response of nonlinear systems at low frequencies and some of them can be found in the literature [29-31]. Earles [29] analyzed a structure excited by m synusoidally varying forces having a

single frictional damper linking two coordinates, where the coefficient of friction was assumed to be linearly proportional to the slip amplitude. Another approach was presented by Dowell [31], in which the dry friction was approximated by the first harmonic and the mode analysis was carried out with the use of Lagrange multipliers and constraint conditions. An interesting method based on the minimization of the difference average between linear and nonlinear systems was developed by Iwan [30]. Also, the scattering of waves traveling in a linear medium and interacting with discrete nonlinear elements was investigated [32-35]. Vakakis [34] concluded that a single incident wave gives rise to an infinite number of reflected waves upon encountering a nonlinear joint. Nayfeh et al. [35] examined the scattering of nondispersive waves by nonlinear joints and found that the nonlinear distortions were found at low frequencies, but were negligible at high frequencies.

The frictional behavior of bolted joints has also been approximated with the use of equivalent linear systems. Wang et al. [36] developed a method to identify equivalent spring-dash pot systems' coefficients to model bolted joints by iterative procedures and experimental verification. Also, Yoshimura [37,38] examined experimentally the characteristics of bolted joints, slide way and welded joints, and created a method to quantify the rigidity and damping coefficients at the joint surface. It was assumed that a horizontal spring-dash pot system to model joints in rods, and a vertical spring-dash pot system to model beams, can employ the simplex method to obtain an optimum combination of coefficient values to match the experimental results. All the above mentioned references computed results of the first two or three mode shapes of the joint model of the case in study.

In this work, the joint is modeled as an energy dissipation mechanism acting as a retarding force proportional to the relative velocity of the incident wave at the joint and, consequently, linear and nonlinear system models for the joint are studied and implemented. Upon encountering a joint, a portion of the wave's energy is transmitted, some is reflected, and some will be dissipated. This is believed to be the first effort to

model structural joints at high frequency; the previous efforts to analyze the dynamics of bolted connections were done with a frequency range corresponding only to the first few modes of vibration. Thereby, the need to model bolted structures under high frequency excitation led us to a unique and clean method to describe the dynamics of bolted systems. Moreover, the nonlinear model of the bolt, derived in this research, presents a unique and readily applicable way to describe the dynamic characteristics of bolted joints. A description of the analytical procedure to model the joint, linearly and nonlinearly, will be presented in chapter 3.

2.3 *Modeling of Material Damping*

Internal friction is a phenomena caused by combinations of physical mechanisms and has been subjected to an extensive research. The history on this subject could be divided into three broad periods: A philosophical approach from 1784 to 1920, industrial applications from 1920 to 1940 and the last period from 1940 to date, in which mechanical principles have been applied to study the influence of damping in structures. For a broad historical review and perspective, the reader can refer to the bibliography [39]. Recent studies emphasizes in the development of mathematical models that can be used to analyze the rheological behavior of a specimen and study a realistic model that characterized the solid structure under investigation. A brief review of some of the most widely used methods to account for lightly damped materials will be here presented.

The amplitude of vibration of a specimen would increase indefinitely in the absence of internal friction when excited by an external alternating force at its resonant frequency [40]. This behavior is found to vary quite considerably depending on the nature of the solid. Three types of materials have been studied in detail in the literature [41]:

- Viscoelastic materials: When a force is applied for times long compared with the relaxation time of the solid, the specimen behaves like a viscous liquid. This is the

simplest mathematical model of rheological systems, which consists of linear dissipation functions (spring and dash pots) in series, parallel or a combination of both.

- Structures at high levels of stress: The linear behavior of viscoelastic materials become insufficient to characterize the significant nonlinearities of structural materials. Therefore the assumption of stability assumed for viscoelastic materials may not be applicable to real structures.
- Material coating: Mainly used in acoustic noise control, this device consists in the application of coating to enhance energy dissipation by increasing the losses associated with fluid flow.

The study of viscoelastic models are the most widely used due to their applicability in most vibration analysis, and they will be considered in this research to model internal friction. A brief description of viscoelastic models will follow: In discussing the viscosity in solids, Maxwell [40] suggested a stress-strain relation dependent on the relaxation time of the solid. When an applied force is acting for times shorter than the relaxation time, the material could be considered to be elastic, on the other hand if the time is long compared to the relaxation time, the solid behaves more like a viscous liquid. He developed a model consisting of a spring in series with a dash pot. Later, Voight [42] assumed two sets of equations to express the stress components in a solid, the first one proportional to the strain and the second one to the rate of change of the strain. Variations of these models have been done considering three or more parameter models, such as Morrison [44], who studied wave propagation in rods with three parameter models. Also, Arenz [45,46] studied the propagation of waves in viscoelastic solids for rods and plates using the models developed by Morrison. Valalis [47] proposed a variational method to reduce a general viscoelastic wave propagation problem into a static problem plus an eigenvalue problem. The reader can refer to the bibliography [43] for an extensive discussion on viscoelastic waves.

Many experimental techniques have been used in the measurement of material damping, they could be classified as [40,48,49,50]:

- Decay of free vibration: These methods are applicable to systems in which the mechanical properties are linear and independent of the amplitude. As an example the reader could refer to the Le Rolland pendulum [40]. More recently Bishop et al. [41] have successfully applied this technique.
- Resonant methods: They are based on obtaining the resonant frequencies of the system, which gives a measurement of the dissipation forces. Kimball et al. used this approach to measure the internal friction of a revolving rod [42].
- Direct stress-strain methods: By this method the shape of the hysteresis loop associated with the system is obtained. A classical example of this method is the Davies-Hopkinson bar [50].
- Wave propagation methods: When a wave propagates through a specimen, some of the energy is dissipated. This attenuation is a result of the internal friction. The work in this area has been related to low frequency, nondispersive waves [50].

Using vibration signature information to measured material damping from test data, modal testing techniques are the most widely used in both, the time and frequency domain. A brief description of modal analysis techniques will be given hereafter, for further reference the reader should refer to the bibliography [52-55]. Assuming a priori a linear structural system, the governing equations of motion describing the dynamics of the system are given by: $[M]\{\ddot{u}\}+[C]\{\dot{u}\}+[K]\{u\}=\{F\}$. Where u is the displacement vector, M is the mass matrix, C is the damping matrix, K is the stiffness matrix and F is the force vector. In the modal testing scheme, only the damping ratio, $\xi = C/2\sqrt{KM}$, is defined. The most commonly used time domain methods in modal analysis are the logarithmic decrement and the curve fitting techniques. The logarithmic decrement is a way to estimate the damping coefficients associated with a particular mode. This is done by exciting the structure at that particular mode and then suddenly removing the force applied, then by measuring the amplitude at the first decay cycle and at the nth decay cycle, the decay of the time history curve can be measured. The curve fitting method assumes the response to be complex and to depend on the exponential of the damping

coefficient. The frequency domain methods can be divided into single degree of freedom and multiple degree of freedom. In the first category are the most commonly used methods in modal testing, such as half power method and methods using co-quad plots. The multiple degree of freedom methods applied the least square curve fitting techniques to obtained the frequency response function using damping ratios.

As an alternative to modal testing damping schemes, Banks et al. [56-58] developed a method to study the transverse vibration of a beam with a tip mass under four damping mechanisms, both internal and external. These damping models are incorporated into the Euler-Bernoulli beam equation as boundary conditions, the resulting differential equations are approximated using cubic splines. This method has been shown to produce more consistent estimates of the Kelvin-Voight damping parameter when compared to modal damping methods. The method is also applicable to hysteretic damping, not treatable by modal methods. In the same line of discussion, Nakao et al. [59] included the internal damping into the differential equations for the rotational and transverse motion of an element, by introducing the corresponding damping parameter as a boundary condition into the Timoshenko's equation of motion.

There are many methods that include damping using semi-discretization methods, such as the finite element formulation, to solve for the dynamics of the system, these methods are classified as frequency dependent viscous damping techniques, and they have taken root in the structural engineering community. Due to the similarity of these methods with the wave propagation methodology used in this study to include the internal friction of structures, a brief description of semi-discretization methods to include material damping will follow. Lesiutre [60,61] has introduced the augmenting thermodynamic fields (ATF) to interact with the displacement field of continuum mechanics. The partial differential equations governing the damped dynamic behavior of the structure are solved using the finite element method and the so-called ATF-damped elements are thereby obtained. Similarly, Golla et al. [62] developed a time domain finite element formulation that expands the canonical form of the mass and stiffness matrices of the undamped system

to include viscoelastic damping with the use of dissipation coordinates. Also, Padovan [63] introduced an algorithm for finite element formulation with fractional operators to include viscoelastic behavior in structures. Another technique [64] uses fractional derivatives to construct stress-strain relationships for viscoelastic materials, and then to apply these relationships in the finite element analysis of the damped structures.

Under low load conditions, typical of the dynamic loads used in this study, the dissipation of energy of vibration through the specimen has little dependency on the frequency of damping cycles. Therefore, the frequency independent methods to measure material damping are also very widely used. The root of these methods originated in a study by Bock and Shlippe [55], they modified the Voight linear viscoelastic model with the introduction of the frequency independent absorption coefficient, which would make the complex stiffness to be frequency independent. Other models of frequency independent complex stiffness are Sorokin's [65] and Reznikov's [66]. More recently, Gaul et al [67] integrated viscoelastic constitutive equations over the volume of the structural member and show that the frequency dependent properties of a vibrating system can be fully described with the frequency independent model, referred as constant hysteric.

The introduction of material damping into the formulation is essential to avoid infinite transmissibility and to obtain meaningful results. Due to the materials used for the modeling of wave propagation in this research (metals), internal friction is added into the analytical formulation by assuming the material to be a Kimball-Lovell solid, and thereby introducing the modulus of elasticity and shear modulus as complex quantities. In chapter 5, an experimental procedure to obtain the viscoelastic properties of lightly damped materials, and an analytical formulation to evaluate the damping in a structure will be presented.

2.4 *Wave Localization*

The phenomena of wave localization is of major importance in the study of wave propagation in structures and has recently received considerable attention by the structural dynamics community. The primary study on localization, or concentration of excitation near the point source, has almost been exclusively dedicated to the effects of structural irregularities. The structures were considered to be periodic, that is constructed of cells acting as filters for the propagating waves and connected in an array. Brillouin [68] was the first to investigate these structures and defined distinct frequency bands, or propagation zones, to carry the wave motion. This fact led to the conclusion that periodic structures have alternate wave passage and wave stoppage bands, from which infinite undamped structures could propagate waves indefinitely in the wave passage band and diminished in the wave stoppage band. An extensive study on periodic structures has been carried by several authors [69-75].

Based on manufacturing irregularities in the material, structures cannot be exactly periodic, but are disordered, reducing the ability to transmit waves from one location to the next. The first work done in disordered periodic structures is accredited to Soong et al. [76], who studied the frequency response of a chain composed of spring-mass-damper units and the variability observed due to changes in these units. Also, Roy et al. [77] studied the effects of attenuation bands in test structures with attached ribs. Since the test structures were considered to be nondissipative, the decay was solely due to multiple reflections at the ribs. A transfer matrix approach was used to relate the state vector (displacements and tractions) at one end to that of the other end. By calculating the eigenvalues of the transfer matrix obtained from this relation, a distinction between pass band and decaying frequencies, depending on whether the modulus of the eigenvalue is one or less than one, was possible. However, for large structures, this analysis could be an incredible task. Pierre et al. [78,79] developed a perturbation analysis to predict the accuracy of localized modes of disordered multispan beams without an eigenvalue

analysis. The modes were calculated using a Rayleigh-Ritz formulation and considered the structure to have small irregularities (to perform perturbation analysis), reducing the computational effort to obtain the disordered structure modes of vibration. In later work, Pierre et. al. [80] extended this method to a twelve span beam to demonstrate the localization of vibration in nearly periodic structures where the span lengths are randomly introduced. Assuming small irregularities on the structure, Cai et al. [81] calculated the decay of wave propagation with respect to the distance of transmission and verified the results using Monte Carlo simulations. Implementation of this decay rate to several periodic systems was done by Wei et al. [82]. Also, Yong et al. [83] described a new perturbation method, which employs the matrices of the wave reflection and transmission to overcome the problem encountered in long structures when the decaying wave appears to grow if viewed from the opposite direction.

To quantify the amplitude attenuation, a localization factor based on the spatial decay of the propagating wave has been introduced and considered to be the inverse of the localization length [84]. This factor is widely used to measure the effect of either strong or weak localization in disordered periodic structures. Li et al. [85] used a transfer matrix approach and a perturbation scheme, similar to the one implemented by Yong et al. [83] and Kissel [84], to prove that wave localization in slightly disordered periodic laminates is typical of high frequency dynamics. The calculation of transfer matrices has been obtained for a Timoshenko beam and mathematically manipulated to give the smallest localization factor based on a Lyapunov exponent [86,87] relation. Studies of the localization factor show that the degree of localization depends mainly on the ratio of the disorder to the internal coupling of the cells forming the periodic structure.

The first approach to consider the magnitude and type of damping in the study of wave localization was recently done by Wei et al. [88] They analyzed a periodic structure with coupling and disorder, but took into consideration the effects of dry friction and viscous damping on the degree of forced vibration localization at low frequency, where dry friction forces are large. Therefore, stick-slip motions can occur in periodic structures,

and a multi harmonic technique is needed to model the nonlinearities. Continuous bladed disks were studied, and tuned and mistuned systems were considered, leading to the conclusion that dry friction is more likely to lead to localization than viscous damping. Moreover, to study the effects of localization in a tuned system, the one harmonic approximation is sufficient to provide good accuracy. In later work, Langley [89] studied the combined effect of damping and irregularities in a one dimensional periodic structure on the localization of vibrational energy. The same conditions that favor localization due to imperfections are also the cause of concentrations due to damping, that is, the occurrence of stoppage pass bands. A transfer matrix approach was used to obtain the attenuation factor, including damping, by considering a complex modulus and thereby introducing a loss factor due to internal friction. The conclusions drawn from this work were that significant degrees of concentration can be observed in slightly damped periodic structures and are comparable to that arising from irregularities.

In this research, damping is considered as the only factor responsible for the attenuation of the propagating wave generated by a PZT source. For health monitoring purposes, the manufacturing irregularities are very difficult to account for due to their probabilistic nature and difficulty to identify. Moreover, the assumption of periodicity to real structures is very limited, and mostly not applicable to the structures on which nondestructive inspections are usually carried on. Nevertheless, structural damping is the most important factor in the localization of the sensing region and it is largely responsible for the attenuation of the propagating wave in a structure. Also, the present work will study the wave localization at high frequencies, while previous work was limited to low frequencies.

2.5 *Dynamic Viscoelastic Modulus Measurement*

Information on material damping properties available from the manufacturers is standard for each specimen, therefore, it does not account for all external and internal

conditions that one could encountered at the experimental site. Therefore, there is a need to measure the dynamic properties of the material, and various techniques are given in the literature [90]; they could be classified as time domain, such as creep and relaxation [91], and frequency domain, such as resonance methods [91], beam methods [91], determination of velocity of propagation [92], and impedance methods [93]. Material properties vary with environmental conditions and manufacturing variability. It is well established [94] that viscoelastic properties of the material have a large scatter and it can not be accounted for by the manufacturer. By measuring the modulus of the material under study in lab conditions, we could obtained a value of the material properties that takes into account viscoelastic effects at the expense of other factors, such as temperature and air, which would be assumed to be fixed for the laboratory site conditions.

In this research, the modulus are obtained using a technique based on the measurement of the velocity of the propagating wave, for this purpose a unique and clean experimental procedure has been implemented and it will be discussed in detail on chapter 6.

Chapter 3

Theoretical Modeling of Wave Propagation and Energy Dissipation in Joints

3.1 *Introduction*

As mentioned previously, a new qualitative non-destructive evaluation (NDE) technique based on a modification of the high frequency impedance measured with an integrated piezoelectric actuator-sensor, has been successfully demonstrated at the Center for Intelligent Material Systems and Structures (CIMSS) [1-3]. An important characteristic of this NDE technique is the localization of the PZT's sensing area due to energy dissipation. For a better understanding of this phenomena, this chapter will present an analytical method to determine the energy dissipated through joints at high frequency and its relation to the localized actuation-sensing region. The structure used for this analysis consists of two beams connected with a bolted joint and having free-free boundary conditions. Due to the high frequency range employed, theoretical assessments are made using a wave propagation approach. For the same reason, the Timoshenko beam theory is used to model the structure. Using the equations of motion, the dynamic stiffness matrix is assembled in the frequency domain. Then, the energy dissipated in the joint is modeled linearly using mass-spring-dash pot systems and nonlinearly with the application of nonconservative friction clearance systems. This work is the first effort in the high frequency modeling of structural joints: other work was only concerned with the modeling of the few first modes of vibration. Case studies and experimental verification of this analytical model will be presented in chapter 4.

The structure used for this analysis consists of two beams overlapped and connected together with two bolts (Figure 3.1). First, the wave propagation model for this particular case is derived. Then, the dynamics of the bolted section is identified with linear spring-dash pot systems: viscous dampers to provide the necessary flow of energy out of the system, and springs to provide the necessary support in the connection. Finally, an extended nonlinear model will be derived to accommodate for the nonlinear behavior of the bolted joint.

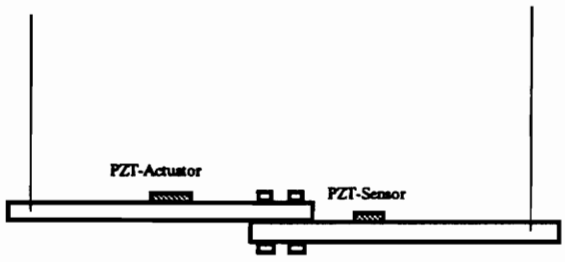

Figure 3.1 Schematic drawing of the bolted beam used in the analysis.

3.2 *Wave Propagation Model*

Due to the high frequency range of the analysis (upto 25 kHz), the research herein presented uses a wave propagation approach, and the one dimensional structure (Figure 3.1) is treated as waveguides along which a wave can travel without spreading in all directions. The wave amplitude decreases less rapidly with distance traveled in a guide than when the wave is unguided. Nonuniformities in guides, such as junctions and discontinuities, are characterized by reflected and transmitted waves due to incident waves. Previous studies [95-101] have been done in the reflection and transmission of stress waves at a discontinuity in order to fully understand the dynamic behavior of structures, but the frequency range used was much lower than the frequency range of interest for this study. In developing the analytical model, only one dimensional

waveguides will be considered. This is because the study of wave propagation under more complicated conditions involves two independent spatial variables, and much study concerned with the dynamic response in this area needs to be done [102-104]. Therefore, by providing an analysis of the well known one dimensional equations, our attention can be focused on the energy dissipation mechanisms of the structure.

Because the dispersive nature of the transverse waves traveling in a one dimensional medium, the response obtained at different locations along the structure would be different, which makes the analysis in the time domain a tremendous task. Consequently, the characterization of waves will be made in the frequency domain. A methodology using a formulation similar to that of the finite element method, but in which no finite set of displacement is assumed in polynomial form and no mass is approximately represented, has already been applied successfully [105-110]. This method, referred to as spectral formulation [109,110] or dynamic stiffness matrix formulation [105-108], treats the distribution of mass and rotational inertia exactly, extending each element from discontinuity to discontinuity. This has the advantage of reducing the number of elements used when compared to finite element formulation. For the bolted beam shown in Figure 3.1, a total of only eight elements is needed to approximate the dynamics of the system. Also, the representation of the beam elements with assumed shape function in the finite element method becomes inexact because a large number of elements are required to model the short wavelength deformation that occurs at high frequency. In the spectral method, the displacements assume the following spectral representation:

$$\upsilon(x,t) = \sum_{n} Y_n \exp[-i(k_n x - \omega_n t)] \qquad (3.1)$$

where n is the particular mode, Y is the wave amplitude, k is the wavenumber (1/length) and ω is the radial frequency of the wave (radians/time). For each mode n, the spectrum

relation, which relates k and ω, is determined. Once the modes are found, their amplitudes are calculated for various sources of excitation.

For thin beams, the vibrations of lower modes are sufficiently described by the Euler-Bernoulli beam theory. However, for higher modes at which the wavelength, $\lambda = 2\pi / k$, is short compared to the radius of curvature of the beam's cross-section, or for deep beams where the effects of transverse shear and rotational inertia become significant, the Euler-Bernoulli beam theory is no longer valid. A theory that accommodates these factors is the Timoshenko beam theory, which occupies a position intermediate to Euler-Bernoulli and the exact theory of elasticity. The Timoshenko beam theory is a good tradeoff for energy dissipation analysis and is expected to give satisfactory results at high frequencies. The governing coupled equations of motion of the Timoshenko beam theory, for total deflection w and bending slope ϕ, are given below for no applied loads [110]:

$$\begin{aligned} GA\kappa \frac{\partial}{\partial x}\left[\frac{\partial w}{\partial x} - \phi\right] &= \rho A \frac{\partial^2 w}{\partial t^2} \\ EI \frac{\partial^2 \phi}{\partial x^2} + GA\kappa \left[\frac{\partial w}{\partial x} - \phi\right] &= \rho I \frac{\partial^2 \phi}{\partial t^2} \end{aligned} \tag{3.2}$$

where E is the modulus of elasticity, G is the modulus of rigidity, I is the moment of inertia of the cross section, A is the cross-sectional area, ρ is the mass density and κ is the Timoshenko's shear coefficient, which is the ratio of the average shear strain in a section and the shear strain at the centroid. Numerical values for κ can be found in the literature [111,112]. For rectangular cross sections, the shear coefficient is $10(1+\nu)/(12+11\nu)$, where ν is the Poisson's ratio of the material. The shear force and bending moment are given by [111]:

$$V = GA\kappa\left(\frac{\partial w}{\partial x} - \phi\right)$$
$$M = EI\frac{\partial \phi}{\partial x} \tag{3.3}$$

respectively.

Using the equations of motion, Equation (3.2), assuming a spectral representation of the displacements, Equation (3.1), and applying the corresponding boundary conditions; the assemblage of the dynamic stiffness matrix containing the damping, stiffness and inertial properties of the beam is constructed and solved at each frequency. The spectral representation of the two independent variables, $w(x,t)$ and $\phi(x,t)$, is:

$$w(x,t) = \sum_n W_{0n} \exp[-i(k_n x - \omega_n t)]$$
$$\phi(x,t) = \sum_n \Phi_{0n} \exp[-i(k_n x - \omega_n t)] \tag{3.4}$$

Upon substitution in the equations of motion, Equation (3.2), it can be shown:

$$\begin{bmatrix} C_I k^2 - \omega^2 & -iC_I k \\ iC_I k & C_{II}k^2 + C_I - C_{III}\omega^2 \end{bmatrix} \begin{Bmatrix} W_0 \\ \Phi_0 \end{Bmatrix} = 0 \tag{3.5}$$

where $C_I = G\kappa / \rho$, $C_{II} = EI / \rho A$, and $C_{III} = I / A$. The solution of Equation (3.5) gives the spectrum relation, which contains four possible modes:

$$k(\omega) = \pm\left[\frac{1}{2}\left(\frac{C_{III}}{C_{II}} + \frac{1}{C_I}\right)\omega^2 \pm \frac{\omega}{2}\left[\left(\frac{C_{III}}{C_{II}}\right)^2\omega^2 + \left(\frac{1}{C_I}\right)^2\omega^2 + \frac{4}{C_{II}} - \frac{2C_{III}}{C_I C_{II}}\omega^2\right]^{\frac{1}{2}}\right]^{\frac{1}{2}} \tag{3.6}$$

two forward moving and two backward moving. Equation (3.6) is the spectrum relation. The phase velocity, $c = \omega / k(\omega)$, gives the dispersive relation, which is dependent on the frequency and therefore dispersive (different frequency components travel at different speeds). The transverse deflection and rotations are related from Equation (3.5), by:

$$W_0 = \left[\frac{iC_I k_j}{C_I k_j^{\,2} - \omega^2}\right]\Phi_0 = R_j \Phi_0 \qquad j = 1,\ldots,4 \tag{3.7}$$

and the solution in the frequency domain is:

$$\begin{aligned} \phi(x) &= C_1 e^{-ik_1 x} + C_2 e^{-ik_2 x} + C_3 e^{ik_1 x} + C_4 e^{ik_2 x} \\ w(x) &= R_1 C_1 e^{-ik_1 x} + R_2 C_2 e^{-ik_2 x} - R_1 C_3 e^{ik_1 x} - R_2 C_4 e^{ik_2 x} \end{aligned} \tag{3.8}$$

where R_1 and R_2 are given by Equation (3.7), with the proper value of k_j, and $\{C_1 C_2 C_3 C_4\}$ is the vector of coefficients.

Incorporation of the longitudinal displacement, *u(x,t),* is established from the rod's equation of motion:

$$EA\frac{\partial^2 u}{\partial x^2} = \rho A \frac{\partial^2 u}{\partial t^2} \tag{3.9}$$

The axial motion is similarly expressed as:

$$u(x) = C_5 e^{-ik_3 x} + C_6 e^{ik_3 x} \tag{3.10}$$

where the spectrum relation is given by, $k_3 = \omega\sqrt{\rho / E}$. The axial force is defined as:

$$F = EA\frac{\partial u}{\partial x} \tag{3.11}$$

The longitudinal, Equation (3.10), transverse, and rotational displacements, Equation (3.8), are then written in terms of the coefficients as:

$$\begin{Bmatrix} u \\ w \\ \phi \end{Bmatrix} = \left[R_{ij}(x,\omega)\right] \begin{Bmatrix} C_1 \\ C_2 \\ C_3 \\ C_4 \\ C_5 \\ C_6 \end{Bmatrix} \tag{3.12}$$

where $i=1,2,3$ and $j=1,...,6$. Similarly, upon substitution of displacements, the axial force, shear force and bending moment are expressed as:

$$\begin{Bmatrix} F \\ V \\ M \end{Bmatrix} = \left[R_{ij}(x,\omega)\right] \begin{Bmatrix} C_1 \\ C_2 \\ C_3 \\ C_4 \\ C_5 \\ C_6 \end{Bmatrix} \tag{3.13}$$

where $i=4,5,6$ and $j=1,...,6$. Therefore by defining the displacement vector as $\upsilon = \{u,w,\phi\}^T$ and the force vector by $\mathcal{F} = \{F,V,M\}^T$, Equation (3.12) and Equation (3.13) are combined to give:

$$\begin{Bmatrix} \upsilon \\ \mathcal{F} \end{Bmatrix} = \left[R_{ij}(x,\omega)\right]\{C\} \tag{3.14}$$

$i=1,...,6$ and $j=1,...,6$, where $\{C\}$ is the vector of coefficients.

The vector of coefficients is solved on the basis of the displacements and forces at the ends of each element. Solving Equation (3.14) at $x = 0$, node 1 of the beam element, and after inversion:

$$\{C\} = [R(0,\omega)]^{-1} \begin{Bmatrix} \upsilon \\ \mathcal{F} \end{Bmatrix}_1 \tag{3.15}$$

and solving Equation (3.14) at $x = L$, node 2 of the beam, and upon substitution of Equation (3.15), we obtain:

$$\begin{Bmatrix} \upsilon \\ \mathcal{F} \end{Bmatrix}_2 = [R(L,\omega)][R(0,\omega)]^{-1} \begin{Bmatrix} \upsilon \\ \mathcal{F} \end{Bmatrix}_1 \tag{3.16}$$

After matrix multiplication, Equation (3.16) is expanded to give:

$$\begin{Bmatrix} \upsilon \\ \mathcal{F} \end{Bmatrix}_2 = \begin{bmatrix} R_{11} & R_{12} \\ R_{21} & R_{22} \end{bmatrix} \begin{Bmatrix} \upsilon \\ \mathcal{F} \end{Bmatrix}_1 \tag{3.17}$$

With expansion of the terms and some mathematical manipulation, the force vector is expressed in terms of the nodal displacements in the form $\{\mathcal{F}\} = [\mathbf{K}]\{\upsilon\}$, where $[\mathbf{K}]$ is the local dynamic stiffness matrix, which is the reciprocal of the transfer function:

$$\begin{Bmatrix} F_1 \\ V_1 \\ M_1 \\ F_2 \\ V_2 \\ M_2 \end{Bmatrix} = \begin{bmatrix} -[R_{12}]^{-1}[R_{11}] & [R_{12}]^{-1} \\ [R_{21}]-[R_{22}][R_{12}]^{-1}[R_{11}] & [R_{22}][R_{12}]^{-1} \end{bmatrix} \begin{Bmatrix} u_1 \\ w_1 \\ \phi_1 \\ u_2 \\ w_2 \\ \phi_2 \end{Bmatrix} \tag{3.18}$$

The local stiffness matrix is obtained at each frequency and then assembled into the global stiffness matrix, which is symmetric and banded, but complex. Thus Equation (3.18) is expressed as:

$$[\mathbf{K}]\{\upsilon\} = \{\mathcal{F}\} \tag{3.19}$$

where $[\mathbf{K}]$ is the global dynamic stiffness matrix. The compatibility of the local stiffness matrix is satisfied at the assembly stage by constraining the beam displacements to match the displacements at the nodes. After application of the boundary conditions, the nodal displacements are found using LU factorization and back substitution. Then, the coefficients are obtained and, therefore the displacement at any location along the beam is determined.

3.3 *Joint Model*

3.3.1 *Linear joint model*

The linear analysis of the joint is made with the use of spring-dash pot systems placed at the matting section and acting in the directions of the degrees of freedom used to describe the motion of the structure. In this system, the dash pots model the viscous damping in the joints, while the springs provide the appropriate rigidity for the connection.

The mathematical model as shown in Figure 3.2a is therefore assumed for computer simulation.

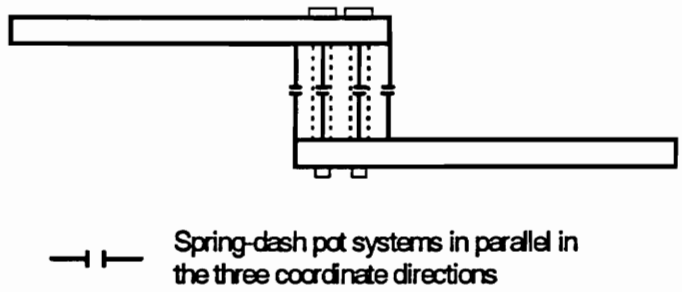

Figure 3.2a Mathematical model used for the linear system of the bolted section.

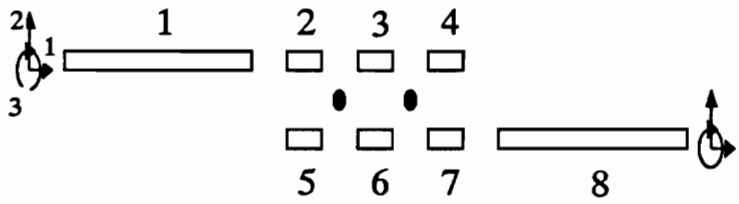

Figure 3.2b The bolted beam is divided into eight elements and three DOF per node.

The matting section is discretized into three elements per beam, extending from discontinuity to discontinuity. The nodes that coincide between the upper and lower beam elements (see Figure 3.2b) are appropriately assembled through a transformation matrix, L, containing 1's or 0's to effectively relate the vector, υ_o, that contains all the displacements, with the vector, υ, which contains only the operating coordinates. This relation is as follows:

$$\upsilon_o = L\upsilon \tag{3.20}$$

The global dynamic stiffness matrix obtained in Equation (3.19) is accordingly transformed as:

$$[\mathbf{K}] = L^T[\mathbf{K}]_0 L \tag{3.21}$$

In the matting section, the bolts are represented by lumped masses and spring-dash pot systems at the corresponding locations, while the outer nodes are simulated with spring-dash pot systems having coefficient values lower than the ones used for the bolts, but allowing for sufficient connectivity of the section and dissipation of energy. These added masses and the forces at the joints, produced by the springs and dash pots, impose boundary conditions on the nodal forces corresponding to their location:

$$\begin{aligned} F &= -\left(K_{B1} + i\omega\eta_{B1} - m_{B1}\omega^2\right) \\ V &= -\left(K_{B2} + i\omega\eta_{B2} - m_{B2}\omega^2\right) \\ M &= -\left(K_{B3} + i\omega\eta_{B3} - m_{B3}\omega^2\right) \end{aligned} \tag{3.22}$$

where K_B is the linear spring coefficient, η_B is the dash pot coefficient, and m_B is the mass of the bolt (mass moment of inertia for subscript 3). The numbering subscripts correspond to the coordinate directions in which these parameters operate (see Figure 3.2b). The forces in Equation (3.22) are included in the dynamic stiffness matrix by balancing the boundary conditions at the corresponding nodal locations.

The associated derived coefficients for the spring-dash pots are obtained with the use of computer simulation and experimental identification. The approach taken in this study assumes initial values similar to those already obtained by Yoshimura [113,114], then identifies the values of the equivalent coefficients for the springs and dash pots with a mathematical simulation to search for the optimum combination of such parameter values. The spring and dash pot coefficients are searched until experimentally obtained resonant frequencies are in good agreement with the measured values, for a certain frequency range and a preset convergence criteria.

3.3.2 *Nonlinear Joint Model*

As already mentioned, the dynamic characteristics of bolted joints are nonlinear and depend on preloading, external loads, matting surfaces and other conditions. In this study it is assumed that these nonlinear nonconservative systems account for all the nonlinearities in the analysis of the structure. Therefore, the nonlinear analysis will consist on calculating the response of the structure at the joint with discrete piece-wise local nonlinearities. The nonlinearities will be approximated with the concept of describing function; containing the nonlinear behavior of the bolted joints, but simplifying the treatment of the piece-wise differential equations of motion representing its dynamics.

The most widely used method to determine the nonlinear characteristic of a vibrational structure is the numerical integration of the equations of motion [115]. However, the step of integration must be very small in order to attain accurate results, therefore making this method very slow for steady state response analysis. For structures under external periodic forcing functions, the frequency domain methods are more suitable for steady state response. One of these methods is the describing function technique [116], which will be used to describe the local nonlinearities of the joint by quasi-linearizating the equations of motion. Hereafter, a brief description of this technique applied to the bolted beam under study will follow.

The equation of motion describing the nonlinear bolted structure vibrating due to a harmonic forcing function is given by:

$$[\mathbf{K}]\{v\} + \{\mathcal{F}_{nl}\} = \{\mathcal{F}\} \tag{3.23}$$

where $\{\mathcal{F}_{\mathcal{NL}}\}$ is the vector of nonlinear internal forces concentrated at the joint; and the rest of the terms have been introduced in Equation (3.19). Because the structure vibrates periodically due to the forcing function, the displacements can be represented by Fourier series as:

$$\upsilon = \sum_{r=0}\left(a_r \cos r\omega t + b_r \sin r\omega t\right) \tag{3.24}$$

Since the nonlinearities of the joint are symmetrical and superharmonic terms are much smaller than the fundamental term, it is safe to neglect higher harmonics, and therefore consider only the first term of the Fourier expansion, when $r = 1$. Similarly, the symmetric internal nonlinear forces acting at the joint undergo harmonic motion, and are expressed as:

$$\mathcal{F}_{\mathcal{NL}} = a\cos\omega t + b\sin\omega t = K_{eq}\bar{\upsilon} + \eta_{eq}\dot{\bar{\upsilon}} \tag{3.25}$$

Displacement with a bar indicates first harmonic approximation as in Equation (3.28). Identification of the parameters of the bolted joint leads to the equivalent spring coefficient:

$$K_{eq} = \frac{a}{\bar{U}} = \frac{\omega}{\pi\bar{U}}\int_0^{2\pi/\omega}\mathcal{F}_{\mathcal{NL}}\cos\omega t dt \tag{3.26}$$

and to the equivalent damping coefficient:

$$\eta_{eq} = -\frac{b}{\omega\bar{U}} = -\frac{1}{\pi\bar{U}}\int_0^{2\pi/\omega}\mathcal{F}_{\mathcal{NL}}\sin\omega t dt \tag{3.27}$$

The spring and damping coefficients depend on the amplitude and frequency of the relative interface deflection and on the nonlinearity of the joint model. The relative displacements at the matting section are also approximated with the first harmonic of Fourier series expansion, that is:

$$\begin{aligned} \bar{v} &= \bar{a}\cos\omega t + \bar{b}\sin\omega t \\ \bar{U} &= \sqrt{\bar{a}^2 + \bar{b}^2} \end{aligned} \tag{3.28}$$

By substituting the assumed displacement field vector into Equation (3.23), the system of equations is solved for different kinds of nonlinearities once their describing equivalent stiffness and damping coefficients are found. Note that to simplify the solution of Equation (3.23), the displacement vector can also be expressed in an exponential form and the system of equations can be solved using complex arithmetic accordingly.

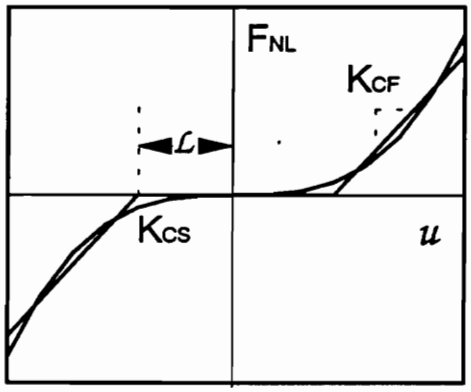

Figure 3.3a. Clearance fit nonlinearity. Approximation with cubic stiffness nonlinearity.

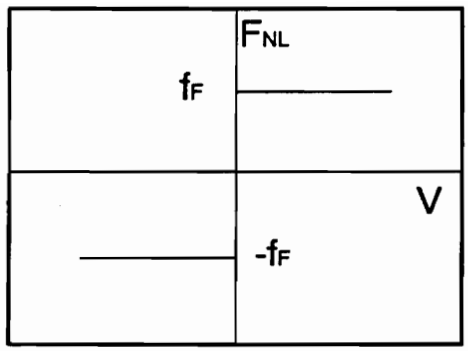

Figure 3.3b. Coulomb damping (V is the relative velocity of the matting nodes at the bolted connection).

Within a bolted joint, bolts may be subjected to the bypass loads on the hole. This effect becomes significant when bolt-hole clearance is measurable. Even though the effects of clearance fit nonlinearities are very small, they will be included in the model since the presence of clearance leads to a region around the bolt hole section that behaves nonlinearly and influences the stresses in the hole and thereby, the dynamic response of the system. The mathematical model of the nonlinear joint at the bolt is shown in Figure 3.4. The stiffness characteristic of joints having clearance fit nonlinearity is shown in Figure 3.3a, where $\mathcal{L}$ is the small bolt hole gap. The piece-wise linear representation of the nonlinear force is given by:

$$\mathcal{F}_{\mathcal{NL}} = \begin{cases} K_{CF}\left(\overline{\upsilon} - \mathcal{L}\right) & \overline{\upsilon} \geq \mathcal{L} \\ 0 & |\overline{\upsilon}| < \mathcal{L} \\ K_{CF}\left(\overline{\upsilon} + \mathcal{L}\right) & \overline{\upsilon} \leq -\mathcal{L} \end{cases} \tag{3.29}$$

Since the clearance is very small, the nonlinear effect shown in Figure 3.3a is approximated with a cubic stiffness fit in order to simplify the real piece-wise behavior of the clearance nonlinearity without loss of accuracy in the model. The force generated by a cubic spring joint is given by:

$$\mathcal{F}_{NL} = K_{CS}\bar{v}^3 \tag{3.30}$$

Thus, the corresponding describing coefficient for this internal nonlinear force has a much simpler expression than that of Equation (3.29) [114], and it is given by:

$$\begin{aligned} K_{eq} &= \frac{3}{4}K_{CS}\bar{U}^2 \\ \eta_{eq} &= 0 \end{aligned} \tag{3.31}$$

The nodes in contact at the matting section are modeled with Coulomb damping, which approximates the behavior of dry friction occurring at the interface. The symmetrical nonlinear behavior of such a model is shown in Figure 3.3b, and the internal nonlinear force is given by:

$$\mathcal{F}_{NL} = f_F Sgn\left(\dot{\bar{v}}\right) \tag{3.32}$$

where *Sgn* is the algebraic sign and f_F is the force of friction defined as the product of the coefficient of friction, μ, and the normal clamping force of the interface, f_N, which is directly proportional to the parabolically distributed bolt pressure over the interface area. The mathematical model of the nonlinear joint at the matting section is also shown in Figure 3.4. Following the describing function formulation, equivalent quasi-linearization of Equation (3.32), leads to an equation having the form of Equation (3.25), where the stiffness and damping coefficients are, respectively, given by:

$$\begin{aligned} K_{eq} &= K_j \\ \eta_{eq} &= \frac{4\mu}{\omega\pi\bar{U}} f_N \end{aligned} \tag{3.33}$$

Once the internal pie-wise nonlinear forces are approximated with describing functions, they are substituted in Equation (3.23), to give the following expression:

$$[[\mathbf{K}]+[\mathcal{F}_{\mathcal{DF}}]]\{\bar{v}\} = \{\mathcal{F}\} \tag{3.34}$$

where $[\mathcal{F}_{\mathcal{DF}}]$ contains the describing functions of the internal forces of the nonlinear elements at the joint, which are placed in matrix form and arranged in accordance to the relative displacement location at which they act. Equation (3.34) is solved at each frequency by approximating the displacement field by the first harmonic. The system of equations given by Equation (3.34) are then evaluated using a Newton-Raphson iteration procedure to solve for the nodal displacements. A first guess is assumed by solving the system when it is considered to be ideally not influenced by the nonlinear elements used to describe the dynamics of the bolted joint. With the use of a relaxation criteria to aid convergence, the set of equations yield the nodal solution as a function of the frequency. The nonlinearities described in this section to model the nonlinear behavior of the bolted joint, present an innovative and simple alternative to account for the complicated dynamics of the connection.

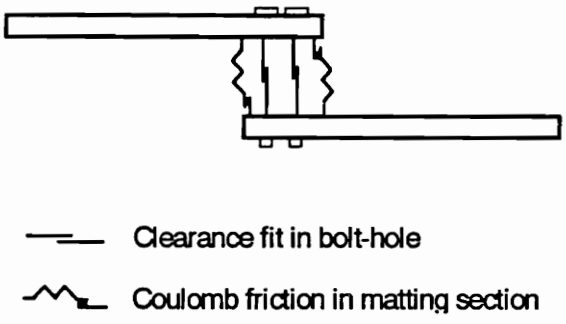

Figure 3.4. Mathematical model used to model the nonlinear behavior of the bolted section.

3.4 *Energy Dissipation Through the Bolted Joints: Power Flux Considerations*

To interpret the energy associated with the propagating wave, it is necessary to define the transmission and reflection coefficients, which are associated with the amount of energy that has been transmitted and reflected after the incident wave encounters the bolted joint. These coefficients are associated with the power flux, which can be derived from the Timoshenko beam theory. Therefore, a derivation of Equation (3.2) is necessary to obtain an expression for the power flux, and it will be briefly presented here. Assuming the displacement field components for a beam as:

$$\begin{aligned} U_x &= -z\phi(x,t) \\ U_y &= 0 \\ U_z &= w(x,t) \end{aligned} \tag{3.35}$$

The strain field can then be derived as:

$$\begin{aligned} &\varepsilon_{xx} = -z\phi',\ \varepsilon_{yy} = 0,\ \varepsilon_{zz} = 0 \\ &\varepsilon_{xz} = \left(w' - \phi\right),\ \varepsilon_{xy} = 0,\ \varepsilon_{zy} = 0 \end{aligned} \tag{3.36}$$

From Hooke's law, the strain-stress relation is given by:

$$\begin{aligned} E\varepsilon_{xx} &= \sigma_{xx} - \nu\left(\sigma_{yy} + \sigma_{zz}\right) \\ G\varepsilon_{xz} &= \sigma_{xz} \end{aligned} \tag{3.37}$$

and the stress field can then be obtained from:

$$\sigma_{xx} = -Ez\frac{\partial \phi}{\partial x}$$
$$\sigma_{xz} = G\left(\frac{\partial w}{\partial x} - \phi\right) \tag{3.38}$$

For an elastic isotropic continuum and considering small motions, the kinetic and potential energy are:

$$T = \frac{1}{2}\int_0^l \int_A \rho\left(\dot{U}_x^2 + \dot{U}_y^2 + \dot{U}_z^2\right) dx dA$$
$$P = \frac{1}{2}\int_0^l \int_A \left(\sigma_{xx}\varepsilon_{xx} + \sigma_{yy}\varepsilon_{yy} + \sigma_{zz}\varepsilon_{zz} + \sigma_{xy}\varepsilon_{xy} + \sigma_{xz}\varepsilon_{xz} + \sigma_{yz}\varepsilon_{xz}\right) dx dA \tag{3.39}$$

respectively. Substituting Equations (3.35), (3.36), and (3.38) into Equation (3.39), the kinetic and potential energy can be defined as:

$$T = \frac{1}{2}\int_0^l \int_A \rho\left(z^2\dot{\phi}^2 + \dot{w}^2\right) dx dA$$
$$P = \frac{1}{2}\int_0^l \int_A \left(-\sigma_{xx} z\phi' + \sigma_{xz}\left(w' - \phi\right)\right) dx dA \tag{3.40}$$

Define the moment of inertia and the cross sectional area as:

$$I = \int_A z^2 dA$$
$$A = \int_A dA \tag{3.41}$$

Also the bending moment and the shear are defined as:

$$M = -\int_A \sigma_{xx} z dA$$
$$V = \int_A \sigma_{xz} dA \tag{3.42}$$

Thereafter, Equation (3.40) could be written as:

$$T = \frac{1}{2}\int_0^l \rho\left(I\dot{\phi}^2 + \dot{w}^2 A\right)dx$$
$$P = \frac{1}{2}\int_0^l \left(M\phi' + V\left(w' - \phi\right)\right)dx \tag{3.43}$$

Extended Hamilton's principle states that:

$$\int_{t_1}^{t_2} \left(\delta T - \delta P + \delta W\right)dt = 0 \tag{3.44}$$

where the infinitesimal increment of the kinetic and potential energy are given by:

$$\delta T = \int_0^l \left(\rho I\dot{\phi}\delta\dot{\phi} + \rho A\dot{w}\delta\dot{w}\right)dx, \qquad \delta\dot{w} = \frac{\partial}{\partial t}\delta w$$
$$\delta P = \int_0^l \left(M\delta\phi' + V\delta\left(w' - \phi\right)\right)dx, \qquad \delta\phi' = \frac{\partial}{\partial x}\delta\phi \tag{3.45}$$

The virtual work done by the applied loads per unit area, moment and shear supscripted with a bar, is given by:

$$\delta W = \int_0^l \left(\overline{M}\delta\phi + \overline{V}\delta w\right)dx \tag{3.46}$$

Substituting these terms into Hamilton's equation:

$$\int_{t_1}^{t_2}\left\{\int_0^l\left(\rho I\dot{\phi}\frac{\partial}{\partial t}\delta\phi+\rho A\dot{w}\frac{\partial}{\partial t}\delta w\right)dx-\int_0^l\left(M\frac{\partial}{\partial x}\delta\phi+V\left(\frac{\partial}{\partial x}\delta w-\delta\phi\right)\right)dx+\int_0^l\left(\begin{matrix}\overline{M}\delta\phi+\\ \overline{V}\delta w\end{matrix}\right)dx\right\}dt=0 \tag{3.47}$$

Integrating each term separately and noting that:

$$\int_{t_1}^{t_2} f\left(f_k,\dot{f}_k\right)\frac{\partial}{\partial t}\delta q_k dt=\left(f\delta q_k\right)\Big|_{t_1}^{t_2}-\int_{t_1}^{t_2}\frac{\partial f}{\partial t}\delta q_k dt \tag{3.48}$$

where the first term of the right hand side is negligible for the time interval, and by grouping terms, we obtain Timoshenko's equations of motion inside the time and spatial integral and the boundary conditions inside the time integral, which must be specified at $x=0$ and $at\ x=l$:

$$\int_{t_1}^{t_2}\left\{\int_0^l\left(-\rho A\ddot{w}+\frac{\partial V}{\partial x}+\overline{V}\right)\delta w dx+\int_0^l\left(-\rho I\ddot{\phi}+\frac{\partial M}{\partial x}+V+\overline{M}\right)\delta\phi dx\right\}dt-\int_{t_1}^{t_2}\left(M\delta\phi+V\delta w\right)dt \tag{3.49}$$

The bending moment and shear force are defined from Equations (3.38) and (3.42). Taking the Timoshenko's correction factor into account, they are given by:

$$\begin{aligned} M&=EI\frac{\partial\phi}{\partial x}\\ V&=GA\kappa\left(\frac{\partial w}{\partial x}-\phi\right)\end{aligned} \tag{3.50}$$

The power flux, $\hat{P}$, is defined as the rate of change of energy dissipation, that is:

$$\hat{P} = \frac{\partial}{\partial t}(T + P) \tag{3.51}$$

Substituting the kinetic and potential energy and integrating, it could be shown that three terms are derived; but for zero applied loads, the power flux is given by:

$$\hat{P} = \left(\dot{\phi}M + \dot{w}V\right) \tag{3.52}$$

Therefore the power flux of the incident, transmitted and reflected waves could be further defined as:

$$\begin{aligned} \hat{P}_I &= \mathrm{Re}\left(M_I\dot{\phi}_I + V_I\dot{w}_I\right) \\ \hat{P}_T &= \mathrm{Re}\left(M_T\dot{\phi}_T + V_T\dot{w}_T\right) \\ \hat{P}_R &= \mathrm{Re}\left(M_R\dot{\phi}_R + V_R\dot{w}_R\right) \end{aligned} \tag{3.53}$$

where the subscripts are self explanatory. The transmissibility coefficient, τ, relates the power flux transmitted of the forward moving wave in beam element 8 (see Figure 3.2b), to the power flux of the forward moving wave in beam element 1:

$$\tau = \frac{\hat{P}_T}{\hat{P}_I} \tag{3.54}$$

The reflection coefficient, $\mathcal{R}$, relates the power flux of the backward moving wave of beam element 1 to the power flux of the incident wave:

$$\mathcal{R} = \frac{\hat{P}_R}{\hat{P}_I} \tag{3.55}$$

For a conservative system, the sum of the transmissibility coefficient and the reflection coefficient must be equal to one. Therefore, for a dissipating system, the power dissipation coefficient, α , is defined as:

$$1 - \alpha = \tau + \mathcal{R} \tag{3.56}$$

These coefficients will be used in chapter 4 to estimate the energy losses that occur at the bolted connection.

3.5 *Conclusions*

A methodology to model one dimensional bolted structures' high frequency vibrations has been developed. Following a wave propagation approach by assuming a spectral representation of the displacements, an assembly of the equations of motion is made on the basis of continuum mechanics. The linear and nonlinear energy dissipation of the bolted joint was then derived. Material damping is added into the formulation by considering the Kelvin-Voight model.

The aim of this work is to investigate the energy dissipated through structural joints and its effect on the localization of the sensing region in the impedance-based health monitoring technique. In chapter 4, a comparison of the results obtained analytically with those of the experimental verification will be presented.

Chapter 4

Supporting Results on the Modeling of Wave Propagation and Energy Dissipation in Joints

4.1 *Introduction*

A methodology to model one dimensional bolted structures at high frequency vibration, was developed in chapter 3. Following a wave propagation approach by assuming a spectral representation of the displacements, an assembly of the equations of motion was made on the basis of continuum mechanics. The linear and nonlinear models of the bolted joint were then derived and included into the formulation to solve for the dynamics of the system. In this chapter, the fully developed analytical model will be applied to the bolted structure previously introduced in chapter 3 and shown in Figure 4.1, consisting of two beams overlapped and bolted together. To study the dynamics of this system, the bolted beam is excited by a PZT-actuator before the joint and the response is recorded by a PZT-sensor after the bolted connection, in order to measure the gain of the structure across the joint.

To account for material damping in the beam specimens, which was modeled assuming the material to be a Kelvin-Voight solid, and also to demonstrate the validity of the analytical method, an analysis of a single beam will first be explored. Then, two models of the bolted joint are considered: a linear system and a nonlinear system. The analytical results obtained from these two models, as well as the experimental results, will be compared. Thereafter, energy assessments can be made based on the values of the optimum set of coefficients used in the analytical model that best fit the experimental results. The energy flow across the joint can then be obtained in terms of the power flux of

the incident, reflected, and transmitted waves at the overlapping section. Evaluation of the energy dissipated by loosening the bolts at the connection will also be presented.

4.2 *Experimental Set-up*

The experimental set-up used to correlate the analytical an experimental results is shown in Figure 4.1: A single PZT-actuator of (20x19x0.19) mm and a PZT-sensor of (22x19x0.19) mm are bonded to the structure and wired to the HP4194A analyzer (Gain-Phase feature) into the input and output slots, respectively. A sine sweep frequency is applied to the PZT-actuator at a constant voltage to excite the system with a coupled axial force-bending moment loading over various frequency ranges, and the signal is recorded by the PZT-sensor across the structural joint. The gain-phase data is then transferred to a PC through a HPIB bus for processing and graphic display of the dynamic response. A constant excitation level of 1 volt rms. is used to excite the structure, and to obtain the gain across the bolted section, as the ratio between the output voltage, measured by the PZT-sensor, and the constantly applied input voltage. Only the bolted structure is shown in Figure 4.1, but the same set-up will be used for the single beam preliminary experiment.

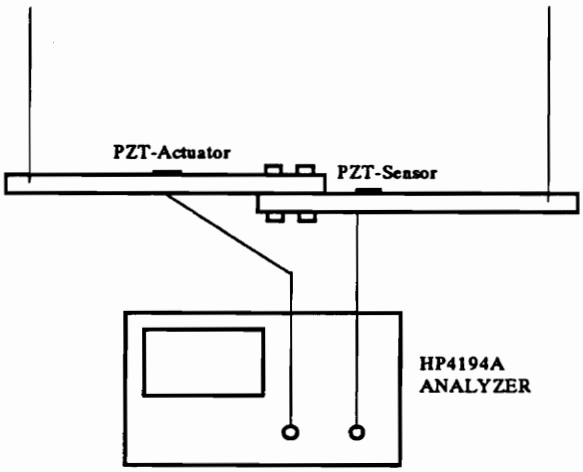

Figure 4.1. Schematic of the experimental set-up consisting of a bolted beam wired to a gain-phase analyzer.

The single aluminum beam and bolted aluminum beam were cut from the same specimen, for material properties homogeneity. They have the same total length of 392 mm and cross sectional area of 19x3 mm. The material used was Al 2024-T4. The bolted structure, as shown in Figure 4.1, consists of two beam elements, 240 mm and 202 mm long, overlapped and bolted together for a total matting section of 50 mm. The bolted joint is made with two equidistant steel bolts, with nuts and spring washers to provide the necessary tension, having a total weight of 17 g per bolt. The PZT-actuator is bonded to the structure at a distance of 63 mm before the joint, and the PZT sensor is located at a distance of 16 mm after the joint.

4.3 *Single Beam Preliminary Results*

To verify the validity of the analytical method presented in chapter 3 and to determine the material damping coefficients, a single beam aluminum specimen is first studied. The analytical model for the single beam gives the gain, as the ratio between the displacement at a given location and the input force, for frequencies of up to 20 kHz. On the other hand, the experimental procedure gives the gain as the ratio between the voltage applied to the PZT actuator and the voltage read by the PZT sensor. Thus, in order to be able to compare the analytical gain with the experimental gain, the input force and output response of the analytical procedure will be transformed to electrical quantities to obtain the voltage ratio, as the experimental reading, through the piezoelectric electromechanical constitutive equations. Also, the material damping is added into the formulation with the use of frequency dependent complex modulus, using a Kelvin-Voight model, typical of viscoelastic materials with low damping.

4.3.1 *Electro-Mechanical Coupling*

The low-power driven PZT actuator-sensor patch, when bonded to a structure, produces a high frequency excitation level at constant voltage and acquires the electrical

impedance, given as the ratio of the voltage source and the current flow modulated by the response of the structure. In this manner knowledge about the mechanical impedance of the monitored structure can be recorded. Due to the high frequency content of this technique minor changes of the structure's configuration are accordingly recorded and detected, before further and more catastrophic failure can occur. Areas in the structure difficult to access can be monitored with this technique due to the small size and easily applicability of the PZT actuator-sensor. Moreover, changes in the structure's configuration close to the PZT's sensing area are only detected, optimizing the detection of incipient damage.

In the theoretical model, calculations of the structural properties are given in terms of the mechanical response of the structure due to any given forcing function. To make this information compatible with the electrical readings, there is a need to account for the electromechanical coupling of the PZT-structure configuration. In this study, measurements of the electrical gain (ratio of the voltage recorded by a PZT sensor and the voltage source of a PZT actuator) and electrical impedance (ratio of the voltage source and the current flow) are made in order to acquire useful information about the attenuation of the PZT's driven wave. Measurements of the electrical gain are necessary to observe the wave's decay at a discontinuity, or several discontinuities, between segments of the structure, while measurements of electrical impedance reproduce the actual readings recorded by the PZT actuator-sensor bonded to a structure for health integrity purposes, and they will be extensively used in chapter 7. In what follows a derivation of the electromechanical coupling of the PZT-structure to implement in the analysis of the theoretical model will be presented.

A previously derived impedance-based model able to describe the dynamic electromechanical interaction between the driven low-power PZT-actuator and the base structure gives the excitation forcing function as:

$$F_x = \frac{Z_s}{Z_a + Z_s} F_{xb} \tag{4.1}$$

where Z_s is the mechanical impedance of the structure; Z_a is the impedance of the PZT-actuator; and F_{xb} is the PZT blocking force; which is a constant value depending on the PZT material properties and the excitation voltage. An extensive derivation of these equations can be found in the literature [117,118]. Since a single PZT is used to excite the structure, a coupled axial force-bending moment loading is generated from the PZT-actuator. The axial force is F_x and the bending moment is $F_x(t_a + t_b)/2$, where t_a is the thickness of the PZT-actuator and t_b is the thickness of the beam element.

The PZT-actuator is added to the analytical procedure by assembling its dynamic properties at the corresponding location in the dynamic stiffness matrix. The modeling of the PZT-actuator patch has been done with the use of Euler-Bernoulli beam theory and the procedure to obtain the desire element matrix is similar to the one described in chapter 3 for Timoshenko beams. The forcing terms at the corresponding node location represent the actuation of the PZT-actuator on the beam.

After assembling the global dynamic stiffness matrix, the system is solved by LU factorization and back substitution and the nodal displacements are then obtained. If desired, the displacements at any location along the beam could also be calculated by solving the spectral coefficients of the displacements. Then, the mechanical strain at the PZT-sensor location can be readily calculated from the following relation:

$$\varepsilon = \frac{t_b}{2}\frac{d\phi}{dx} + \frac{du}{dx} \tag{4.2}$$

where $d\phi / dx$ is the derivative of the rotational displacement and du / dx is the derivative of the axial displacement. Furthermore, the electric field of the PZT-sensor acting in the thickness direction, E_3, is given by:

$$E_3 = g_{31} T_1 \tag{4.3}$$

where g_{31} is the piezoelectric voltage constant, and T_1 is the stress acting on the PZT. Alternatively the electric field could also be defined as the voltage reading over the thickness of the PZT, V/t_a . Therefore, after substituting this expression and the stress of the PZT into Equation (4.3), the voltage reading can be expressed as:

$$V_{out} = g_{31} t_a \overline{Y}_{11} \varepsilon \tag{4.4}$$

where $\overline{Y}_{11}$ is the complex modulus of the PZT. Thus, with the analytical gain based on the voltage ratio of the PZT, a direct correlation of the analytical and experimental results can be made. The material properties of the PZTs used in this study correspond to PSI-5A-S2.

On the other hand, to acquire information about the electrical impedance there is a need to know the current flow through the PZT as modulated by the structural mechanical properties. This can be derived by differentiating the flux density, D_3, with respect to time, and integrating over the electroded area, one could obtain the current flow as:

$$I_3 = i\omega \iint_A D_3 dxdy \tag{4.5}$$

The flux density is governed by the following constitutive equation:

$$D_3 = d_{31} T_1 + \overline{\varepsilon}_{33} E_3 \tag{4.6}$$

where d_{31} is the piezoelectric constant at zero stress, and $\overline{\varepsilon}_{33}$ is the complex dielectric constant. Substituting Equation (4.3) into Equation (4.6) and then further substitute into Equation (4.5), an expression for the current flow is given by:

$$I_3 = i\omega\left[d_{31} + \bar{\varepsilon}_{33} g_{31}\right] \bar{Y}_{11} w_a l_a \varepsilon \tag{4.7}$$

where w_a and l_a are the width and thickness of the PZT, respectively. Then, the electrical impedance is given by:

$$Z = \frac{V_{in}}{I_3} \tag{4.8}$$

With the expressions of the electrical gain and electrical impedance, a direct correlation of the analytical and recorded results could be successfully made.

4.3.2 *Analytical and Experimental Results: Correlation*

After including the electro-mechanical coupling into the analytical formulation, the resonant frequencies and amplitude of the response (gain) for the single aluminum beam were calculated. The resonant frequencies analytically obtained were compared to those obtained experimentally, and the Kelvin-Voight coefficients (η_E and η_G) were modified accordingly, until the analytical and experimental gain coincided closely. The results are given in Table 4.1. The matching of the natural frequencies shows the validity of the dynamic modeling method. Also, the amplitude of the resonant peaks gave a good approximation for the material damping coefficients, which values will be also included in the bolted beam modeling analysis.

Table 4.1. Natural Frequencies of the single beam corresponding to the bending modes.

Natural Frequency No.	Experimental Results (Hz)	Analytical Results (Hz)
1	108	105
2	292	295
3	575	580
4	954	960
5	1,418	1,435
6	1,990	2,005
7	2,650	2,660
8	3,400	3,415
9	4,248	4,255
10	5,193	5,185
11	6,235	6,215
12	7,345	7,330
13	8,553	8,530
14	9,873	9,810
15	11,245	11,170
16	12,738	12,735
17	14,300	14,325
18	15,920	15,945
19	17,620	17,645
20	19,410	19,420

4.4 *Modeling of the Joint*

The quantitative analysis of bolted joints is at present an impossible task, therefore assumptions and estimates have to be made in order to approximate its dynamics. As explained in great detail in chapter 3, the identification of the parameters describing the behavior of the bolted joint under active loading has been carried out by many researchers and very good models have been developed. The aim of this paper is to provide an useful tool to approximate the dynamics of the joint as an integrated part of the structure, and be able to obtain accurate results at relatively high frequency content (upto 25 kHz) with the proposed models. The parameters used to describe these models will give further insight into the interaction of a propagating wave at the joint and the consequent energy losses that occur. The bolted joint is modeled using linear and nonlinear systems.

4.4.1 *Linear Model of the Joint*

The bolted beam is divided in a total of ten elements, as shown in Figure 4.2: There are three degrees of freedom (DOF) per node and the assembling is done following similar procedures as that for finite element methods. Although, care need to be taken along the matting section due to the overlapping of the beam elements. Thereby, a transformation of the local DOF to global coordinates is been done in the program routine, with the use of a transformation matrix containing 1's or 0's accordingly to the nodal position in the global coordinates.

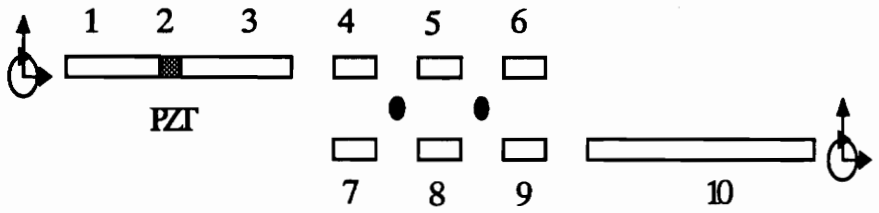

Figure 4.2. The bolted beam is divided into ten elements and the dynamics of the PZT are included accordingly.

The vibration analysis of the bolted beam is first approximated with the use of linear mass-spring-dash pot systems acting as boundary conditions at appropriate locations in the assembling of the global system of equations. These systems act as nodal forces and nodal lumped masses in the three coordinate directions at their corresponding position in the force vector. A first guess of the spring and dash pot coefficients are obtained from the bibliography [119], this values are included in the formulation at the appropriate nodal positions. A frequency range containing only the bending mode of interest is chosen: Experimentally, the 19th mode, corresponding to a resonant frequency of 17.4 kHz, provided the largest deflection at the bolted section and therefore was taken as reference to adjust the joint parameters of the bolted joint. The resonant frequency and amplitude of the response, corresponding to this set of coefficients, are calculated and compared to the experimental values. The coefficients are iterated until the convergence, for that particular

mode, is attained. An optimal set of values for the coefficients thus found is such that they most closely describe the pattern of the vibrating structure, and they are selected to further investigate the dynamics of the system and to solve for all the modes in the frequency range of interest. Similar iterative procedures have been carried out in the bibliography [113,114], in which the coefficients of the springs are solved independently of the damper coefficients for the first two modes of vibration. This procedure gives an estimate on the analysis of the complex behavior of bolted joints. A flow chart of this numerical procedure is outlined in Figure 4.3.

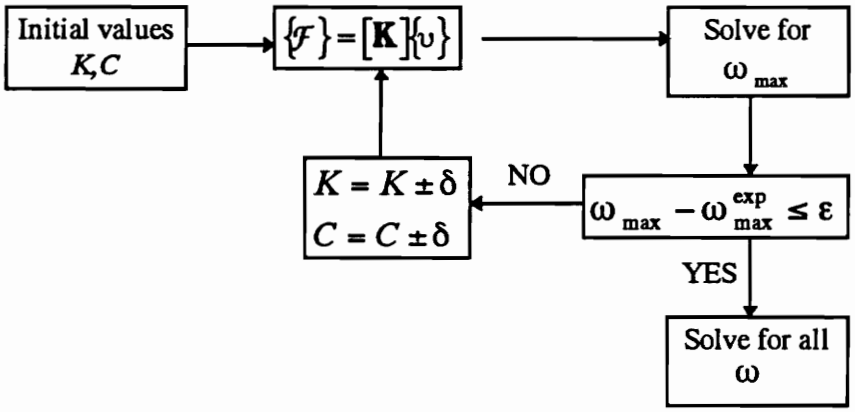

Figure 4.3. Flow chart of the numerical procedure used to analyze the dynamics of the bolted joint.

The results of the resonant frequencies corresponding to the first 23 bending modes (torsional modes are not accounted for in the analytical procedure) are presented in Table 4.2. It should be noticed that the 19th mode, corresponding to the largest deflection, is in very good agreement with the experimental results because it was taken as reference to adjust the joint system's coefficients. Moreover, in the experimental results were found two torsional modes, which, for the frequency range used in this study, were not considered reliable for incipient damage detection purposes, due to their high instability to the slightest variations on the structure's configuration not considered as damage. Experimentally, these modes were isolated from torsional modes using a laser technique.

Table 4.2. Natural Frequencies of the bolted beam corresponding to the bending modes.

Natural Frequency No.	Experimental Results (Hz)	Linear Results (Hz)	Nonlinear Results (Hz)
1	100	100	100
2	284	260	230
3	540	500	485
4	921	910	860
5	1,345	1,300	1,320
6	1,993	2,010	2,085
7	2,468	2,470	2,505
8	3,528	3,550	3,555
9	3,940	4,180	4,210
10	5,337	5,340	5,380
11	6,350	6,190	6,250
12	7,275	7,140	7,265
13	8,037	8,000	8,035
14	9,162	9,080	9,100
15	10,400	10,320	10,340
16	12,075	12,180	12,205
17	13,037	13,210	13,290
18	15,987	15,010	15,650
19	17,400	17,390	17,390
20	18,975	19,160	18,910
21	21,710	21,180	21,760
22	22,360	21,960	21,990
23	22,740	22,220	23,020

We will briefly outline this laser procedure; the experimental set-up is shown in Figure 4.4. The bolted structure is excited at the resonant frequency of the mode to be analyzed through the PZT-actuator by a signal generator at 15 volts. The laser vibrometer reads the response of the excited structure through a multipurpose voltmeter. As the laser scans through, a maximum voltage coincides with a maximum amplitude for the mode, and a minimum voltage coincides with a node. This way the number of nodes could be measured for any given mode and we could easily corroborate whether a natural frequency corresponded to a bending mode. Those frequencies experimentally obtained and suspected to be torsional modes were further investigated by measuring the voltage along the width of the beam at any location, to observe a logical pattern of a torsion with the

voltage recorded. For the sake of completeness, the bending modes corresponding to the analytical model were also calculated and plotted by computing the displacements along the bolted beam, and they were found to resemble closely those obtained from the laser procedure described above.

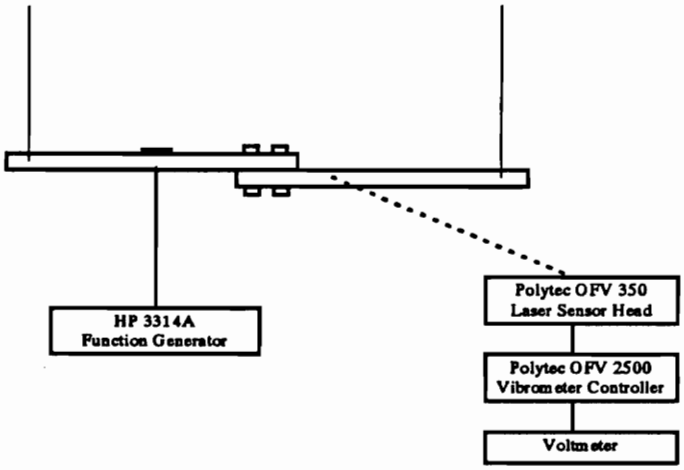

Figure 4.4. Experimental set-up used to track the modes of vibration for the bolted beam shown, and to isolate bending and torsional modes.

With the optimal set of spring and dash pot coefficients, the linear analytical model is now able to give a good approximation of the bolted beam dynamic response. Based on this linear model, the energy dissipation mechanisms will now be studied and a comparison of the power flux of the propagating waves at the joint will be considered. The expression of the power flux of a propagating wave, $\hat{P}$, was given in chapter 3 as:

$$\hat{P} = \left(\dot{\phi}M + \dot{w}V\right) \leq 0 \tag{4.5}$$

Note that the power flux must be negative to dissipate energy at the joint. One could similarly define the power flux of the incident wave, $\hat{P}_I$, transmitted wave, $\hat{P}_T$, and the reflected wave, $\hat{P}_R$, at the joint. Thereafter, the transmissibility coefficient, which relates the energy of vibration of the transmitted wave to that of the incident wave at the bolted connection, is defined as:

$$\tau = \frac{\hat{P}_T}{\hat{P}_I} \tag{4.6}$$

And the reflection coefficient is similarly expressed as:

$$\mathcal{R} = \frac{\hat{P}_R}{\hat{P}_I} \tag{4.7}$$

Since the joint is an energy dissipation mechanism, we could define the energy dissipation factor, δ, as:

$$1 - \delta = \tau + \mathcal{R} \tag{4.8}$$

In the same line of discussion, the energy flow across the bolted joint can be also assessed from the difference of the energy flux before the joint, beam element 3 in Figure 4.2, and the energy flux after the joint, element 10, that is the rate of change of energy across the bolted section could be defined as:

$$\frac{d\mathbf{E}}{dt} = \left(\dot{\phi}_3 M_3 - \dot{\phi}_{10} M_{10} + \dot{w}_3 V_3 - \dot{w}_{10} V_{10}\right) \tag{4.9}$$

For a single resonant frequency, the pattern of the response was plotted, both, analytically and experimentally when the bolted joint was fully tight, total torque of 25 Nm. Then, by slightly loosening the bolts in the connection to 22 Nm, the pattern was also recorded experimentally and calculated analytically by decreasing the stiffness in the springs and increasing the damping in the dash pots. The behavior of loosening the bolts is shown in Figure 4.5 for the 19th mode of bending vibration, at which the bolted section has maximum deflection for the frequency range of interest. By loosening the bolts, the pattern of vibration (gain of the structure) would shift down, due to the decrease in

amplitude of the propagating wave and therefore, a clear indication that energy has been dissipated through the bolted connection.

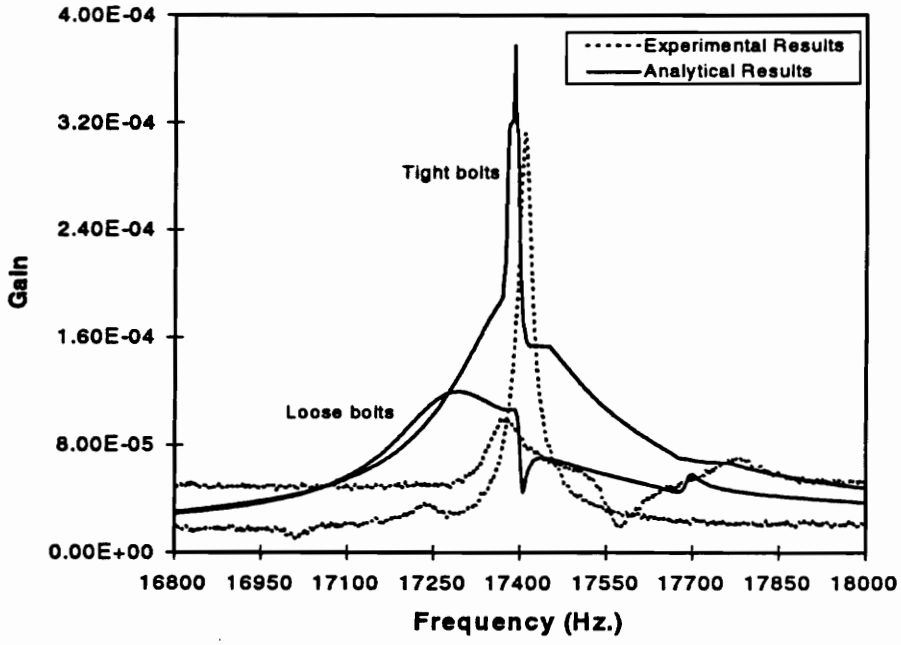

Figure 4.5. Effect of loosening the bolts in the structure under study. Comparison of analytical results using the linear model and experimental results for the 19th mode of vibration.

Reproducing the dynamics of the structure with a set of optimal coefficients to describe the mechanics of the bolted joint and with the use of the introduced energy factors, visualization of the wave's interaction at the overlapped section are made possible. Such interaction is shown in Figure 4.6 for the 19th mode: The comparison is made between the transmitted wave at the jointed section, elements 4 and 7 in Figure 4.2, and the transmitted wave after the joint, elements 6 and 9, when the bolts were fully tight (25 Nm). The transmission at the joint is consistently larger than the transmission after the joint, as a consequence, there is more energy of the incident wave been dissipated after the joint, as it can be seen from the dissipation factors at the joint and after the joint. The proportion of energy transmitted and dissipated at the joint and after the joint is maintained until the bolted beam vibrates at the resonant frequency, at which larger deflections at the matting section occur. At this point the wave interaction at the joint

depends largely on the magnitude of this deflection. For the resonant frequency corresponding to the 19th mode, at which it was observed that the bolted beam is at its maximum deflection, the transmission and dissipation decreases, while the reflection increases at both of the locations monitored in the beam. Following by a jump in transmission and dissipation, coupled with a decrease in reflection at the resonant frequency.

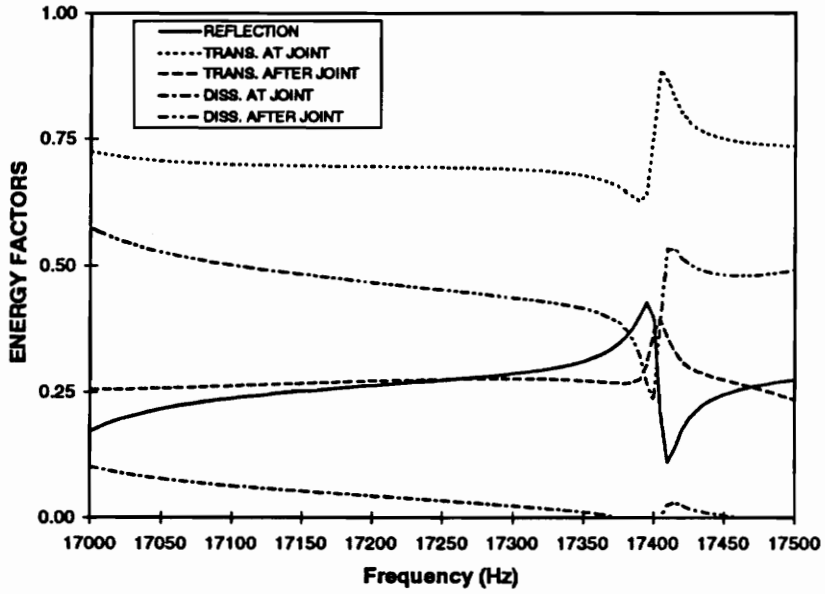

Figure 4.6. Interaction of the propagating wave at the bolted section for the 19th mode.

To support these findings, the wave behavior at the bolted section for a second mode was also studied. Figure 4.7 shows the wave interaction of the 17th mode, at which the deflection is much smaller than for the 19th mode. For this case the transmission at the joint is also consistently larger than after the joint, while the dissipation is also consistently smaller. At the resonant frequency, the transmission and reflection clearly decreases, to increase again after the effect of the resonance has diminished. On the other hand, the dissipation increases at the resonance. This behavior closely resembles the wave interaction observed for the 19th mode, but, nevertheless it should be emphasized that the reaction of the wave at the joint for a given resonant frequency is unique. Such

phenomena can be explained due to the dispersive behavior of the propagating wave, which changes shapes as it travels, and therefore it is highly frequency dependent.

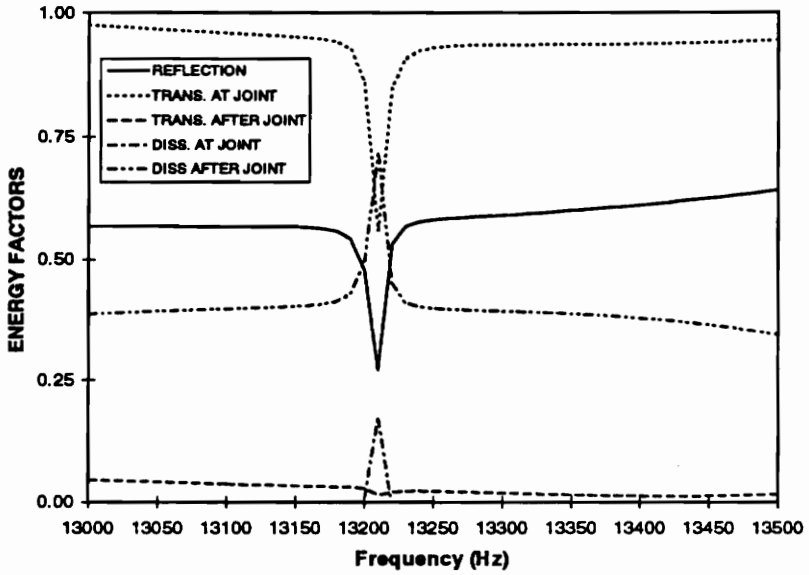

Figure 4.7. Interaction of the propagating wave at the bolted section for the 17th mode.

For the purpose of completeness, the energy dissipated through the joint at each of these two modes was further investigated with the aid of Equation (4.9). The energy dissipated in relation to the maximum energy dissipated at the 19th mode is shown in Figure 4.8: When the bolts are tight (25 Nm), the energy dissipated is approximately 50% of the maximum energy dissipated when the bolts are loosen (22 Nm). By slightly reducing the clamping pressure of the bolts, there is a large increment of energy losses. The effect of loosening the bolts was reproduced using the coefficients obtained from the results shown in Figure 4.5. As a comparison, similar findings were observed for the 17th mode, as shown in Figure 4.9. The energy dissipated when the bolts are tight and when the bolts are loosen were normalized with respect to the maximum energy dissipated for the 19th node, corresponding to the highest deflection. The energy dissipated when the bolts are tight is also approximately 50% that of the maximum energy dissipated when the bolts are loosen. But, since the 17th mode correspond to a smaller deflection of the matting section, the energy dissipated was lesser than the energy dissipated for the 19th mode.

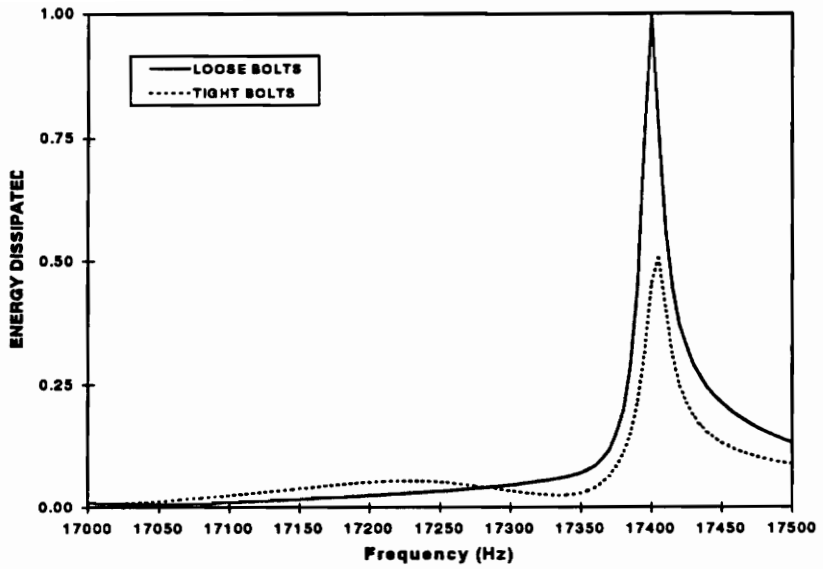

Figure 4.8. Rate of energy dissipated when the bolts are tight and when the bolts are loosen for the 19th mode. Linear model

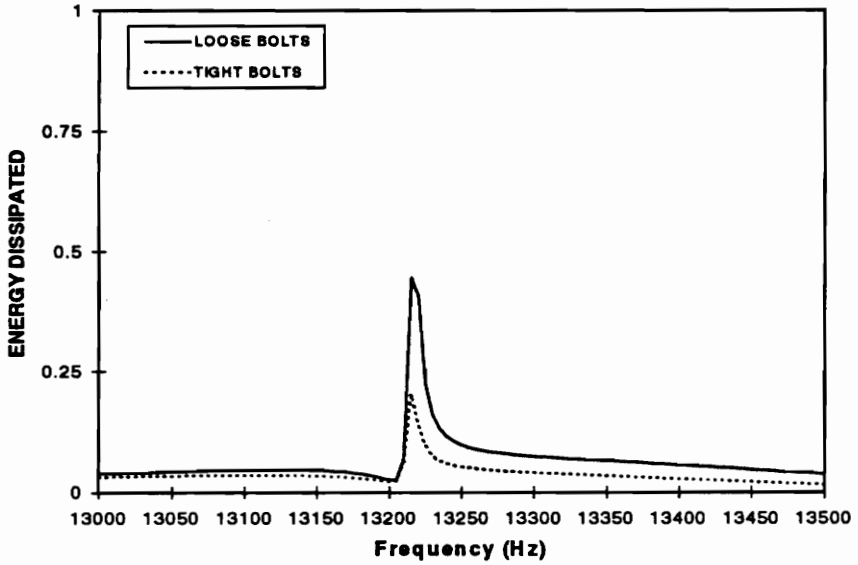

Figure 4.9. Rate of energy dissipated when the bolts are tight and when the bolts are loosen for the 17th mode. Linear model.

4.4.2 *Nonlinear Model of the Joint*

An extended nonlinear model of the bolted joint was done assuming clearance fit nonlinearity at the bolt-hole section and Coulomb friction damping at the matting section.

Both of these elements have a piece-wise nonlinear behavior, approximated for their dynamics using a describing function approach. The clearance fit nonlinearity is further simplified with a cubic nonlinearity, this approximation is made possible because the spacing between the bolt and the hole is very small and the tightness of the bolt is sufficiently large. The nature and mathematical model of these nonlinear elements were described in detail in chapter 3, together with the procedure used to incorporate them into the formulation.

Due to the nonlinearities of these elements, the system of equations obtained is iteratively solved using a Newton-Raphson technique. A first guess of the displacements is numerically obtained by solving the system when it is not influenced by the nonlinearities of the bolted section. Then, a first guess of the coefficients used to model the nonlinear behavior of the bolted joint are assumed by calculating the clamping force at each of the bolts from the measurement of the total torque they exert. Variations of the coefficient of friction make any quantitative assessment an impossible task, therefore, theoretical analysis is done with the use of the tangential force, $F_f = f_N \mu$, as the product of the normal clamping force and the coefficient of friction. The other coefficients used to describe the nonlinear bolt are the stiffness of the clearance approximation, K_{cs}, and the stiffness of the Coulomb friction coefficient, K_j. These coefficients are placed into the formulation at appropriate locations and varied iteratively in a similar way as it was done for the linear case, see the flow chart in Figure 7.4, until convergence, with the used of a relaxation criteria, is attained. The 19th mode was also taken as reference to adjust the joint parameters of the bolted section. The mass and mass moment of inertia of the bolts are also added into the formulation in the same manner as for the linear model.

The incorporation of nonlinear elements into the formulation brings a more realistic behavior of the bolted section into the model under study. The resonant frequencies obtained with the use of nonlinear systems to model the joints are also given in Table 4.2: As expected, higher order modes are better modeled using the nonlinear

systems with a one harmonic approximation than with the linear joint model. But, for the lower modes, the nonlinear model looses accuracy since a multi-harmonic approximation is needed in order to obtained more accurate results. Similar energy analysis, as described for the linear model, was performed for the nonlinear case. The behavior of loosening the bolts for the 19th bending mode is shown in Figure 4.10: As the bolts are loosen, the amplitude of vibration decays due to the energy been dissipated through the bolted region. The effect of loosening the bolts is done by decreasing the stiffness of the Coulomb friction coefficient and the tangential force at the matting nodes.

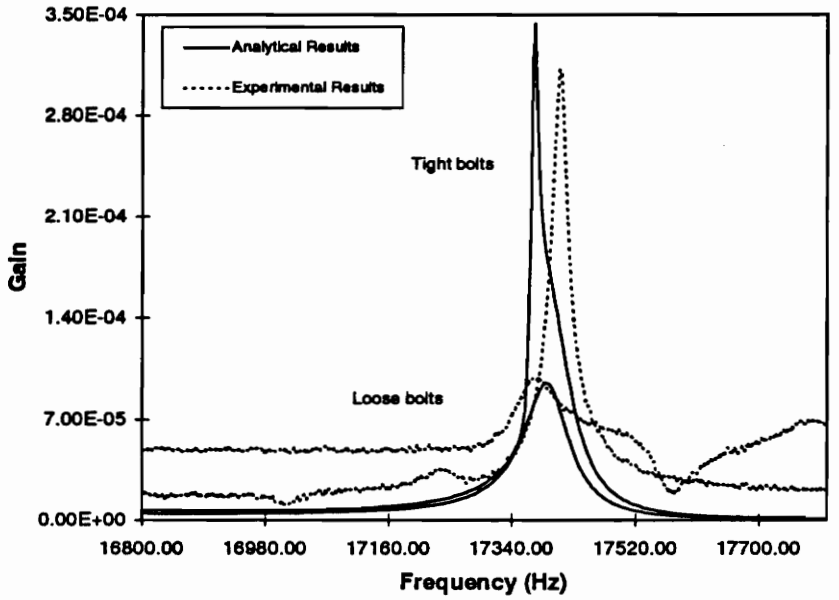

Figure 4.10. Effect of loosening the bolts in the structure under study. Comparison of analytical results using the nonlinear model and experimental results for the 19th mode of vibration.

For the purpose of comparison, evaluation of the rate of energy dissipated by loosening the bolts for the case shown in Figure 4.10, as it was done for the linear model of the joint, was also applied to the nonlinear case. Figure 4.11 shows the effect of loosening the bolts by decreasing the applied torque 3 Nm, as it was shown in Figure 4.8 for the linear case. Similarly, the energy dissipation when the bolts are tight is also approximately 50% of that when the bolts are loosen.

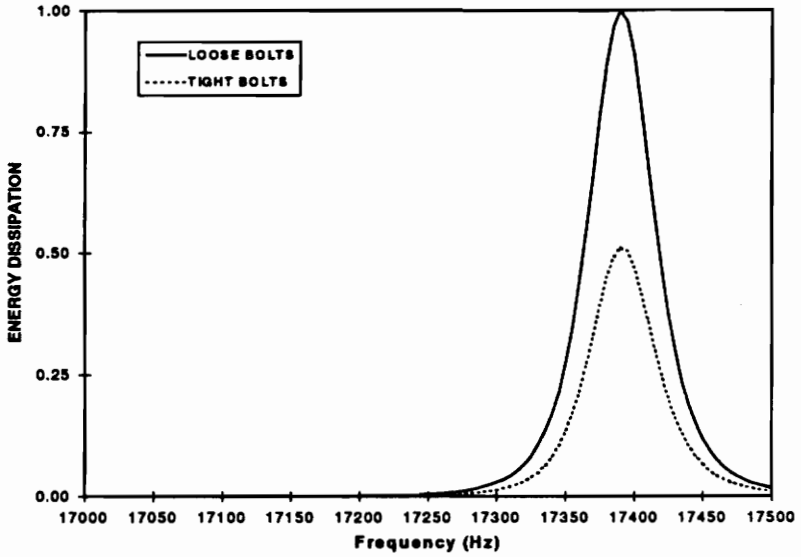

Figure 4.11. Rate of energy dissipated when the bolts are tight and when the bolts are loosen for the 19th mode. Nonlinear model.

4.5 *Conclusions*

A simple method to approximate the dynamics of one dimensional structures with bolted joints at high frequency content has been here presented. Firstly, the validity of the analytical procedure, introduced in chapter 3, was successfully corroborated. Then, this procedure was used to model the bolted beam shown in Figure 4.1. For this purpose two systems were considered to simulate the dynamic behavior of the bolted connection; a linear system consisting of spring-dash pots in parallel and a nonlinear system, which accounts for clearance fit at the bolt-hole section and Coulomb friction at the matting section.

An extensive analysis using the linear system was carried out for a frequency content that included resonant frequencies of upto the 20th bending mode. It was proven experimentally that torsional modes are too sensitive to alterations not considered as damage, and therefore cannot be relied on to track the health condition of the system. With the use of the simple linear system, it was shown that even small changes in the tightness of the bolts cause a large increase in the dissipation of energy. These energy

losses lead to a localization of the propagating wave to the near vicinity of the excitation source. This sharp increase in the rate of energy change is due to the fact that the incident wave decays exponentially after encountering a dissipating bolted joint. The interaction of the incident wave at the bolted section was also presented by comparing the transmission and the dissipation factors at the joint and after the joint. Comparison of such results for the 19th mode, corresponding to the largest deflection, and the 17th mode, shows that the propagation of the wave, as expected, is highly frequency dependent, and therefore it changes shape as it travels, making, any general conclusion on the exact quantification of the energy of vibration an impossible task. Nevertheless, the position of the wave and size of the wavelength with respect to the bolted section, which depends on the frequency, plays a crucial role on the beam's deflection.

The extended nonlinear system used to model the bolted region was also analyzed for its vibrations by showing the effects of loosening the bolts at a given resonance. These effects were similar to those shown for the linear model, but by accounting for the piece-wise nonlinear behavior of the bolted connection with a first harmonic approximation, more accurate results at higher frequencies were obtained. The accuracy of the linear model with respect to the nonlinear model can be explained due to the fact that the clamping forces at the matting section were kept very high. The energy dissipated at the nonlinear model of the bolted joint was also presented, showing similar results to those observed for the linear model.

The behavior of transmission and reflection at the joint, for a given frequency range containing a resonant peak, was well reproduced with the analytical model presented in chapter 3. Furthermore, it was shown that, due to the dispersive relation of bending waves, the interaction of the traveling wave at the joint is unique and therefore, only qualitative theoretical predictions can be made. Also, as expected the largest energy losses coincided with the largest cyclic peak. The results here presented proves the validity of the proposed method to qualitatively asses the interaction of the propagating wave at a bolted joint and the energy losses that occur. The large increase of energy dissipated when

the bolts were slightly untaught was also observed, indicating the importance of bolted joints in the effect of localization on the sensing region.

Chapter 5

A Theoretical Study of Wave Localization due to Structural Damping

5.1 *Introduction*

In order to implement the new impedance-based NDE technique presented at the introduction, it is necessary to have a better understanding of the localization phenomena to establish guidelines for the placement of the PZT actuator-sensors on the complex structure to be monitored; guidelines such as the type of PZT actuator-sensors to be used, the quantity of sensors required to monitor the critical area, or the optimal location of the sensors. Thus, to explain this localization phenomena, there is a need to model the energy dissipated as the wave, generated by the PZT, propagates throughout the structure. The two principal energy dissipation mechanisms causing localization have been attributed to material damping and nonconservative joints. In this chapter, the focus will be stressed on the material damping energy dissipation. Hence, quantification of the energy dissipated due to material damping and its effect on the wave localization will be here presented.

As in chapter 3, and due to the high frequency content of the analysis, a wave propagation approach based on continuum mechanics will be used to model a long beam, bolted at the middle and clamped at its ends (Figure 5.1). For the same reason, the rotational and transverse motion of the system are implemented with the Timoshenko's equation of motion, while the axial motion is described using the rod equation. The material damping will be incorporated into the theoretical model by using the correspondence principle. At the end of this theoretical modelization effort, an implicit expression for the specific damping capacity will be obtained, along with the effect of

energy dissipation in the attenuation of the wave propagating through the structure. The numerical results of this theoretical model, along with experimental verification will be presented in chapter 6.

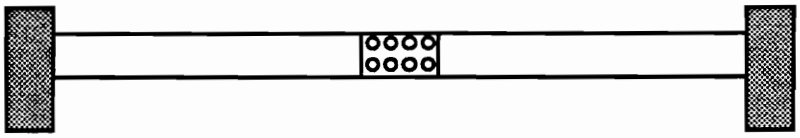

Figure 5.1. Schematic drawing of the Long beam bolted at the mid-span and with clamped-clamped boundary conditions used in this study.

5.2 *Wave Propagation Modeling*

Due to the high frequency employed in the analysis, a wave propagation approach is considered to study the dynamics of one dimensional structures. These structures can be treated as waveguides, along which the wave can travel without spreading in all directions. The Timoshenko beam theory, which accounts for transverse shear and rotational inertia (factors to account for when the wavelength is short compared to the radius of gyration of the beam's cross-section), covers the inadequacies of the Euler-Bernoulli theory for higher modes of vibration and therefore, will be used in this work to study the rotational and transverse motions of the structure. The longitudinal motion will be described with the use of the rod theory. In wave propagation, the displacements assume a spectral representation of the form:

$$v(x,t) = \sum_n Y_n \exp\left[-i\left(k_n x - \omega_n t\right)\right] \tag{5.1}$$

where n is the particular mode, Y is the wave amplitude, k is the wavenumber (1/length) and ω is the radial frequency of the wave (radians/time). For each mode, n, the dispersion

relation, which relates k and ω, can be determined [120]. Once the modes are found, their amplitudes are calculated for various sources of excitation. The wave propagation velocity or phase speed, c, is given by:

$$c = \frac{\omega}{k} = 2\pi\omega\lambda \tag{5.2}$$

where λ is the wavelength. A methodology using a formulation similar to the finite element method, but in which no finite set of displacement is assumed in polynomial form and no mass is approximately represented, has been presented in chapter 3. Since the inertial properties of the specimen are exactly represented, the beam elements can extent from discontinuity to discontinuity. For the purpose of completeness, a brief description of this method will be here presented. The process starts with the well known Timoshenko equations of motion:

$$\begin{aligned} GA\kappa \frac{\partial}{\partial x}\left[\frac{\partial w}{\partial x} - \phi\right] &= \rho A \frac{\partial^2 w}{\partial t^2} \\ EI \frac{\partial^2 \phi}{\partial x^2} + GA\kappa \left[\frac{\partial w}{\partial x} - \phi\right] &= \rho I \frac{\partial^2 \phi}{\partial t^2} \end{aligned} \tag{5.3}$$

where E is the modulus of elasticity, G is the modulus of rigidity, I is the moment of inertia of the cross section, A is the cross sectional area, ρ is the mass density, and κ is the Timoshenko's shear coefficient, which is the ratio of the average shear strain in a section and the shear strain at the centroid. The shear force and bending moment are given by:

$$\begin{aligned} V &= GA\kappa\left(\frac{\partial w}{\partial x} - \phi\right) \\ M &= EI \frac{\partial \phi}{\partial x} \end{aligned} \tag{5.4}$$

respectively. Upon substitution of the spectral representation of the displacements and after some mathematical manipulation, one can obtain the dispersive relation as:

$$k(\omega) = \pm\left[\frac{1}{2}\left(\frac{C_{III}}{C_{II}}+\frac{1}{C_I}\right)\omega^2 \pm \frac{\omega}{2}\left[\left(\frac{C_{III}}{C_{II}}\right)^2\omega^2+\left(\frac{1}{C_I}\right)^2\omega^2+\frac{4}{C_{II}}-\frac{2C_{III}}{C_IC_{II}}\omega^2\right]^{\frac{1}{2}}\right]^{\frac{1}{2}} = \pm\left[E_K^*\right]^{\frac{1}{2}} \tag{5.5}$$

where E_K^* is the elastic stiffness of the structure, $C_I = G\kappa/\rho$, $C_{II} = EI/\rho A$, and $C_{III} = I/A$. Equation (5.5) gives four possible modes: two forward moving and two backward moving. The transverse deflection and rotations are related by:

$$W_o = \left[\frac{iC_Ik}{C_Ik^2-\omega^2}\right]\Phi_o = R_j\Phi_0 \qquad j = 1,2 \tag{5.6}$$

The complete solution in the frequency domain of the rotational and transverse motion, respectively, is given by:

$$\begin{aligned}\phi(x) &= C_1e^{-ik_1x} + C_2e^{-ik_2x} + C_3e^{ik_1x} + C_4e^{ik_2x}\\ w(x) &= R_1C_1e^{-ik_1x} + R_2C_2e^{-ik_2x} - R_1C_3e^{ik_1x} - R_2C_4e^{ik_2x}\end{aligned} \tag{5.7}$$

where R_1 and R_2 are given by Equation (5.6), with the proper value of k. The functions in Equation (5.7) can be written in terms of the nodal displacements of a single beam element at $x = 0$ with a subscript 1, and at $x = L$ with a subscript 2. Then, one could establish a relation between the coefficients $\{C_1, C_2, C_3, C_4\}^T$ and the nodal displacements. Similarly, relation between the coefficients and the global nodal forces can be also derived. After some mathematical manipulation and proper assemblage of the elements, the nodal forces are related to the degrees of freedom with the dynamic stiffness matrix, $\mathbf{K}$, which contains the stiffness, damping and inertial properties of the system, written as:

$$f(\omega,E,G) = [\mathbf{K}]\{\upsilon\} - \{\mathcal{F}\} = 0 \tag{5.8}$$

where $\{\mathcal{F}\}$ is the vector of global nodal forces, and $\{\upsilon\}$ is the vector of global nodal displacement. The longitudinal motion of the system is included with the use of the rod equation in a similar manner and added at appropriate locations. The local stiffness matrix is obtained at each frequency and then assembled into the global stiffness matrix, which has the usual properties of being symmetric and banded, although usually complex. Compatibility is readily satisfied at the assembly stage by constraining the beam displacements to match the displacements of the nodes. After application of the boundary conditions, the global stiffness matrix is inverted and the nodal displacements are found. The displacements at any location along the beam elements could also be readily obtained once the nodal displacements are substituted back and the coefficient vector is calculated.

5.3 *Structural Damping Modeling*

The work here presented focuses on the effect of material damping in the attenuation of the vibrational energy, and the importance of this phenomena on the localization of the sensing region. For this purpose, both longitudinal and transverse waves will be generated, and the dispersion relation reproduced to obtain the dynamic viscoelastic modulus and loss factors for the material. The necessity to add material damping in the dynamic analysis of structures with the use of the Timoshenko equations of motion has been previously addressed [121-124]; this has been done by replacing E by $E(1+i\eta)$ and G by $G(1+i\eta)$, where η is the damping coefficient (assumed the same for E and G). By adding material damping with this simple linear complex modulus relation, the dispersion for the Timoshenko beam becomes continuous at the higher frequency spectrum. That is, the second mode has a cut-off frequency at 268 kHz, below which only the imaginary part becomes zero. By adding damping, both real and imaginary, can propagate without any discontinuity. This way mathematical infinity is avoided in the numerical analysis.

There are several definitions for damping [125], but in this study the specific damping capacity, φ, defined as the ratio between the energy dissipated during one cycle of strain, ΔW, and the maximum strain energy stored in the material, W, will be used:

$$\varphi = \frac{\Delta W}{W} \tag{5.9}$$

For the steady-state solution, the specific damping capacity can be expressed in terms of the tangent of the phase lag, $\tan\phi$, as:

$$\varphi = 2\pi \tan\phi \tag{5.10}$$

where ϕ is the angle by which the response lags the input force. The elastic response of an isotropic material is governed by the modulus of elasticity, E, and the shear modulus, G. Introducing the correspondence principle [126,127], which enables the calculation of the viscoelastic solutions from the elastic solutions, the elastic material properties can be written in terms of the corresponding viscoelastic complex moduli. The basis of this principle resides in the fact that the application of an alternating force produces, in the steady state, a sinusoidal displacement which lags the force by the tangent phase lag. By correlating the displacement with the alternating input force by means of the linear operator $\mathbf{K}$, such $\upsilon = \mathbf{K}^{-1}\mathcal{F}$, where $\mathcal{F}$ is the input force, it can be shown that:

$$U(\omega)\exp\left[i\left(\omega t - \phi(\omega)\right)\right] = K^{-1}F_0 \exp(i\omega t) \tag{5.11}$$

The complex transfer function, $U^*(\omega)$, is defined in terms of the amplitude characteristic and phase-lag characteristic of the response, as:

$$U^*(\omega) = U\exp\left[i\phi(\omega)\right] = U'(\omega) + iU''(\omega) \tag{5.12}$$

where the real and imaginary components are known as the frequency characteristics.

Similarly the elastic natural frequency and the elastic stiffness of the structure, are also expressed in complex form and divided into their real and imaginary parts:

$$\begin{aligned} \omega^* &= \Omega \exp\left[i\phi_\omega(\omega)\right] = \omega' + i\omega'' \\ E_K^* &= E_K \exp\left[i\phi_{E_K}(\omega)\right] = E_K' + iE_K'' \end{aligned} \tag{5.13}$$

To obtain an expression for the specific damping capacity of the structure, the phase lag of the structure's elastic stiffness, ϕ_{E_K}, is expressed in terms of the lag phase angle of the natural frequency, ϕ_ω. Based on Equation (5.2) and Equation (5.5), the wave speed is proportional to the square root of the elastic properties of the structure, E_K^*. Therefore, the natural frequency of the structure is related to its elastic properties by the followings relation:

$$\Omega \exp\left[i\phi_\omega(\omega)\right] = c\sqrt{E_K \exp\left[i\phi_E(\omega)\right]} \tag{5.14}$$

From this expression, it can be easily shown that the phase lag of the elastic stiffness is twice that of the natural frequency phase lag of the system. Upon substitution of the elastic stiffness phase lag into Equation (5.10), one could obtain the expression for the specific damping capacity of the structure in terms of the phase lag of the natural frequency as:

$$\varphi_E = 2\pi \tan 2\phi_\omega = 4\pi \frac{\omega''}{\omega'} \left[\frac{1}{1 - \left(\frac{\omega''}{\omega'}\right)^2} \right] \approx 4\pi \frac{\omega''}{\omega'} \tag{5.15}$$

where the bracketed term can be neglected for small phase lag.

The application of the correspondence principle has already been successfully implemented for modal analysis purposes [128,129]. Hereafter, a formulation based on this concept is derived to obtain an implicit expression of the specific damping capacity of the jointed beam under study, and therefore $\omega' = \omega$ will be assumed. The first step in the calculation of the specific damping capacity of the structure is to calculate ω' by using the implicit expression of the perfectly elastic beam, Equation (5.8), given by:

$$f(\omega, E, G) = 0 \tag{5.16}$$

The next step is to obtain an expression for the imaginary part of the natural frequency in Equation (5.15). The damping is included using the correspondence principle, writing Equation (5.16) in terms of the complex quantities (superscript asterisk) as:

$$f(\omega^*, E^*, G^*) = 0 \tag{5.17}$$

The analysis begins by carrying out a Taylor expansion of Equation (5.17) in terms of ω, E, G as follows:

$$\begin{aligned} f(\omega^*, E^*, G^*) = f(\omega, E, G) + (\omega^* - \omega)\frac{\partial}{\partial \omega} f(\omega, E, G) + \\ (E^* - E)\frac{\partial}{\partial E} f(\omega, E, G) + (G^* - G)\frac{\partial}{\partial G} f(\omega, E, G) \end{aligned} \tag{5.18}$$

Substitution of Equation (5.16) and its complex counterpart, Equation (5.17), into Equation (5.18), gives, after some mathematical manipulation, an expression for the imaginary part of the natural frequency:

$$\omega'' = -\frac{\left(\left(E^{\bullet}-E\right)\frac{\partial f}{\partial E}+\left(G^{\bullet}-G\right)\frac{\partial f}{\partial G}\right)}{\left(\frac{\partial f}{\partial \omega}\right)} \tag{5.19}$$

where the values of $E^{\bullet}$ and $G^{\bullet}$ are found from experimental evaluations, as will be demonstrated in chapter 6. Once Equation (5.8) has been substituted into Equation (5.19), the real and imaginary parts of the resulting matrix are separated and the specific damping capacity of the structure can then be calculated with the use of Equation (5.15). The resulting matrix from Equation (5.19) is solved by computing the determinant at the natural frequencies.

5.4 *Conclusions*

The motivation of this research is to analyze the effect of wave attenuation in structures to yield a better understanding of the localization phenomena of the sensing region of a PZT actuator-sensor. For this purpose, a methodology to study the effect of material damping on the dissipation of vibrational energy in structures has been presented in an effort to correlate the energy dissipation and the phenomena of the local sensing region.

The dynamics of a long bolted beam is modeled at high frequency using a spectral approach based on continuum mechanics. This methodology accounts for structural discontinuities, such as bolted connections and light material damping, which are experimentally derived and added into the formulation. The energy dissipated is given in terms of the specific damping capacity of the structure, from which a quantification of energy dissipation is possible. A scheme based on the correspondence principle for lightly damped materials to obtain an estimation of the specific damping capacity was derived. It makes use of an intrinsic equation that describes the dynamics of the system, and it is expanded in Taylor's series about the correspondent material properties to give an implicit

expression for the energy dissipated. The material damping is introduced using an experimental procedure that will be described in chapter 6.

Chapter 6

A Theoretical Study of Wave Localization due to Structural Damping: Results

6.1 *Introduction*

This chapter will apply the analytical procedure previously derived in chapter 5 to demonstrate the importance of structural damping in the local effect of the sensing region of a PZT actuator-sensor bonded to a structure for health monitoring purposes. The localization of the sensing region is due primarily to energy dissipation mechanisms; structural connectivities and material damping. Other factors, such as defects in assembly or manufacturing of the materials, could also affect the localization of the energy of vibration, but they are not considered in this study. Moreover, the variability in manufacturing are included through experimental investigation of the intrinsic damping properties, while the geometric discontinuities within the specimens are not taken into account due to their probabilistic nature.

In chapter 5, a methodology was derived to calculate the specific damping capacity as a measurement of the energy losses in structures. In the work here presented, analytical and experimental results are jointly performed to corroborate the validity of the method. The one dimensional structure under investigation is shown in Figure 6.1: It consists of two beams bolted together and clamped at both ends. Two pairs of PZT-actuators are bonded to the structure before the connection; one pair is placed in-phase to create a longitudinal extension force and the other pair of actuators are bonded out-phase to generate a couple bending moment. Two PZT-sensors are placed before and after the

joint, at the locations shown, in order to measure the amplitude and phase of the propagating wave. The phase speed or wave velocity is recorded by measuring the amplitude and phase of the response at the PZT-sensors placed before the joint, and thereby reconstructing a dispersive relation curve as a function of frequency. This relation is used to obtain the viscoelastic properties of the medium to be substituted into the formulation derived in chapter 5, and then the energy dissipated in the structure as a measurement of the specific damping capacity could be assessed. A comparison of the energy dissipated due to internal friction and due to structural joints will then follow.

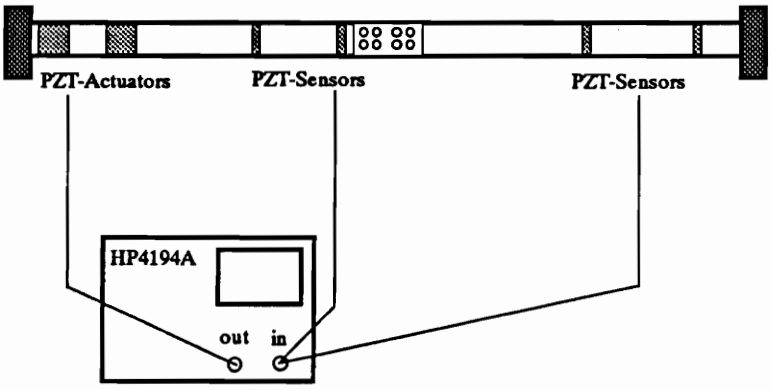

Figure 6.1. Beam used in this study, bolted at the mid-span and with clamped-clamped boundary conditions. The experimental set-up used for the analysis is also shown.

6.2 *Experimental Set-up*

The experimental set-up is shown in Figure 6.1. The structure under study consists of two Al 2024-T4 beams, having each a cross section of 50.84x6.40 mm and butt bolted together with two very thin plates attached to the beam specimens with eight bolts and nuts to create a solid connection. The steel bolts and nuts have each a total weight of 16 gr. per bolt and they are tighten at a torque of 25 Nm. The length of each beam is 91 cm and the total bolted section is 10 cm. The structure is clamped at both ends. This

configuration has a PZT pair acting in-phase and bonded to one end of the structure to generate longitudinal waves, and another pair of PZTs acting out-phase and generating bending waves. Before and after the joint there are two PZT-sensors, bonded at the locations shown in Figure 6.1, to measure the amplitude and phase of the propagating wave. The PZT-actuators have dimensions 38x50.84x1.9 mm and the PZT-sensors have dimensions 6x50.84x1.9 mm. These PZTs are alternatively wired to a multipurpose HP4194A gain-phase analyzer: A sine sweep frequency is used to excite a pair of PZT-actuators at a selected frequency range, the response is recorded by a PZT-sensor at 401 time steps. The recorded data is transfer to a PC for processing via a GPIB bus.

6.3 *Dynamic Viscoelastic Modulus Measurements*

Information on material damping properties available from the manufacturers is standard for each specimen. It does not account for all external and internal conditions that one could encountered at the experimental site. Therefore, there is a need to measure the dynamic properties of the material under laboratory conditions. Various techniques have been reviewed in chapter 2. As it was mentioned, by measuring the modulus of the material under study in laboratory conditions, we could obtained a value of the material properties that takes into account viscoelastic effects at the expense of other factors, such as temperature and air friction, which would be assumed to be constant throughout the experiment. In this work, the modulus of the material are obtained using a technique based on the measurement of the propagating wave's velocity dispersive relation. For this purpose a unique and clean experimental procedure has been implemented and it will be here underlined.

The dispersive relation can be stated as the link between the phase speed and frequency. The phase speed, c, is defined as:

$$c = \frac{\omega}{k(\omega)} \tag{6.1}$$

where $k(\omega)$ is the wavenumber (1/length). Expressions for the wavenumber for both, longitudinal and bending waves were derived in chapter 3, and for the purpose of completeness they are given here. For longitudinal waves, the wavenumber is expressed as:

$$k_L(\omega) = \omega\sqrt{\frac{\rho}{E}} \tag{6.2}$$

while for bending waves, described by the Timoshenko equations of motion, there are two distinct wave numbers, given by:

$$k_T(\omega) = \left[\frac{1}{2}\left(\frac{\rho}{E} + \frac{\rho}{G\kappa}\right)\omega^2 \pm \frac{\omega}{2}\left[\left(\frac{\rho}{E}\right)^2\omega^2 + \left(\frac{\rho}{G\kappa}\right)^2\omega^2 + 4\left(\frac{\rho A}{EI}\right) - 2\left(\frac{\rho^2}{EG\kappa}\right)\omega^2\right]^{\frac{1}{2}}\right]^{\frac{1}{2}} \tag{6.3}$$

where E is the modulus of elasticity, G is the shear modulus, ρ is the mass density and κ is the Timoshenko correction factor.

By substituting independently Equation (6.2) and Equation (6.3) into Equation (6.1), the expressions for the phase speed of both longitudinal and transverse waves can be respectively obtained. When the phase speed is constant with respect to the frequency, the wave is said to be nondispersive, that is the case for longitudinally propagating waves, while if the phase speed varies as a function of frequency the wave is said to be dispersive, such as for bending waves. For dispersive waves, the propagating wave travels at different

speeds depending on the frequency component, and therefore the wave would appear to change shape as it goes through the medium.

There are typical values of phase speed calculated from the available theory of wave propagation to obtain the speed at which a wave travels through different materials, and this is obviously calculated with the values of standard elastic material properties. Due to internal friction in the specimens, the values of the modulus vary from those given by the manufacturer. By experimentally obtaining these values under the present conditions of the structure, one could obtain the true viscoelastic properties of the system, which could then be incorporated into the equation describing the dynamics of the structure:

$$f(\omega, E, G) = [\mathbf{K}]\{\upsilon\} - \{\mathcal{F}\} = 0 \tag{6.4}$$

Estimation of the viscoelastic complex modulus properties of the medium is made with interpolation values taken from the experimentally obtained dispersive curve. Therefore, one need to calculate the phase velocity of the propagating wave. This is done with the aid of the experimental set-up shown in Figure 6.1: The beam is excited by a pair of PZT-actuators at one end, and the amplitude of the gain, as well as, the phase of the structure are recorded at the two PZT-sensors placed before the bolted connection via the HP4194A gain-phase analyzer. The phase velocity and amplitude ratio of these two measurements are calculated with the following relationship [130]:

$$c = \frac{\omega(x_2 - x_1)}{\phi_2 - \phi_1 + 2n\pi}$$
$$Amplitude\ Ratio = \left|\frac{\mathbf{G}_2(\omega, x)}{\mathbf{G}_1(\omega, x)}\right| \tag{6.5}$$

where x is the distance from the pair of PZT-actuators to the first PZT-sensor, for subscript 1, and to the second PZT-sensor, for subscript 2. The phase, ϕ, is defined to be the arctangent of the ratio between the imaginary and the real parts of the wave motion, $\mathfrak{G}$. The term $2n\pi$ is the spectrum phase lag, where n is an increasing even number chosen so the phase velocity and frequency relationship are continuous. The amplitude ratio must be less than 1 in order to process the measured data, which is recorded at selected frequencies, and the dispersive relation for longitudinal and transverse waves can then be reconstructed.

Since the phase speed of the wave is directly related to the structural properties of the system, one could obtain accurate assessment of the viscoelastic behavior of the structure as a whole from the dispersive curve using the measured wave motion. With the use of Equation (6.5), the wave velocity can be measured as a function of frequency, taking the value of the wave velocity at frequency 0 as that given by the theory.

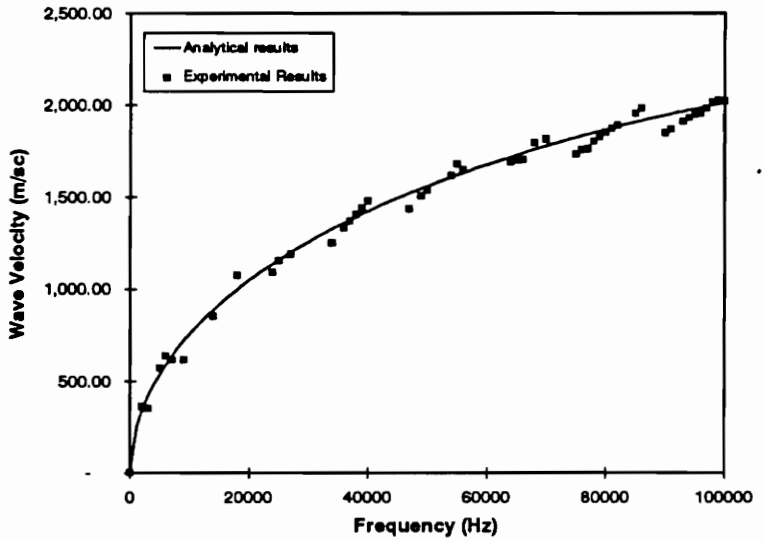

Figure 6.2. Dispersive relation of bending waves. Experimental data is obtained by reproducing the wave velocity as a function of frequency, while the analytical results are obtained from Timoshenko's beam theory.

For the sake of brevity, results for the nondispersive behavior of bending waves are only given; they are shown in Figure 6.2. The structure is excited with the use of a pair of PZT-actuators out phase to generate a bending wave that propagates through the beam. The gain and phase are measured at the two PZT-sensors located before the bolted connection. The theoretical curve is obtained with the use of Equation (6.1) and Equation (6.3). But, as it was stated in chapter 5, only the real part of the first mode of the Timoshenko beam behaves continuously dispersive, and therefore it is the only one considered. The experimental results of the dispersive curve are plotted by measurements of the phase velocity as a function of frequency. The material parameters are determined by picking any two arbitrary wave speed values and their corresponding frequencies, and substituting them into Equation (6.1) and Equation (6.3), then the nonlinear set of equations are solved for the viscoelastic modulus considering the mass density to be a standard constant value for aluminum specimens (2715 kg/m^3). This procedure is repeated to complete all the data points experimentally obtained. By averaging the so determined values one could obtained the material properties through the dispersive curve of Figure 6.2. The results are shown in Table 6.1.

By assuming the linear viscoelastic response of an isotropic material, the modulus of elasticity and shear modulus could be represented by:

$$\begin{aligned} E^* &= E' + iE'' \\ G^* &= G' + iG'' \end{aligned} \tag{6.6}$$

respectively. Where $(\,)'$ is the real part of the complex quantity or storage, and $(\,)''$ is the imaginary part or loss. The complex modulus and corresponding loss factor for the modulus of elasticity are given by:

$$\left|E^*\right| = \sqrt{E'^2 + E''^2}$$
$$\tan\phi = \frac{E''}{E'} \tag{6.7}$$

respectively. Similar expressions for the shear modulus also apply. The loss factor represents a measurement of the rate of energy dissipated by the material, and could be readily obtained once the viscoelastic values of the material properties are experimentally measured, and noting that for low damped materials, such as aluminum, $\tan\phi \approx \phi$. Therefore Equation (6.6) could be written, for the modulus of elasticity, as:

$$E^* = E(1 + i\phi_E) \tag{6.8}$$

The values for the loss factors of the material properties are also given in Table 6.1.

Table 6.1. Material properties of standard values for Al 2024-T4 and via wave velocity measurements. Loss factors are also experimentally obtained.

Material Properties	E (GPa.)	G (GPa.)
Standard value	73.0	28.0
Flexural Wave	73.361704	27.990861
Loss Factors	0.004955 (η_E)	0.0003264 (η_G)

6.4 *Analytical Procedure*

6.4.1 *Modeling the Response of the System*

The modeling of the system is done using a wave propagation approach based on continuum mechanics. The beam elements are treated as one dimensional waveguides and they are modeled using Timoshenko's beam theory for bending and flexural motion and

the rod equation for longitudinal motion. This method treats the mass and rotational inertia exactly and it is assembled in a similar manner as semidiscretation methods, such as the Finite Element. A derivation of this method and the element matrix formulation of the dynamic stiffness has been previously presented in chapter 5 and in Reference [131], and it will not be reproduced here. To model the structure under study, only a total of 10 elements were needed, as shown in Figure 6.3. Element 2 contains the pair of PZT-actuators acting out-phase and therefore its dynamics are included properly into the formulation accounting for the electro-mechanical effects as derived in Reference [132]. The model of the joint connection was done assuming the bolts to be approximated with linear mass-spring-dash pot systems, and acting at the locations shown in Figure 6.3. Reasonable values for the stiffness coefficients and damping coefficients of the bolts are taken from a similar experiment previously presented [132]. Analysis of the first 18 modes is done by measuring the gain of the structure as the ratio of the voltage recorded at any of the PZT-sensors located after the bolted joint, and the constant driven voltage fed in by the PZT-actuator pair. This ratio can be reproduced analytically after including the electro-mechanical effect of the PZT-actuator pair and PZT-sensor as described in the literature [132]. The experimentally obtained resonant frequencies are given in Table 6.2; these were measured with the experimental set-up previously described in Figure 6.1.

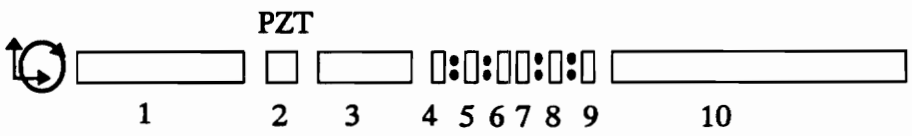

• Linear joint systems with lumped mass

Figure 6.3. Model of infinitely long beam: three degrees of freedom per node, and a total of 10 elements. Also shown is the approximation of the bolts at the connection with linear systems and the inclusion of the PZT-actuator in element 2, where it creates a couple moment.

Table 6.2. Natural frequencies of the long beam. The analytical results are obtained with the numerical investigation of the determinant of the dynamic stiffness matrix.

Natural Frequencies	Experimental Results (Hz.)	Analytical Results via Determinant (Hz.)	Error %
1	57.0	51.1	5.6
2	102.0	105.4	3.3
3	143.5	140.6	2.0
4	270.0	276.3	2.3
5	341.0	307.5	9.8
6	429.0	453.3	5.7
7	514.0	514.7	0.1
8	539.0	562.0	4.3
9	639.0	669.7	4.8
10	721.0	796.8	10.0
11	876.0	929.7	6.1
12	937.0	955.7	2.0
13	1100.0	1076.9	2.1
14	1442.5	1424.0	1.3
15	1842.0	1871.5	1.6
16	2230.0	2258.4	1.3
17	2752.0	2779.1	1.0
18	2920.0	2922.1	0.7

The analytical determination of the natural frequencies of the beding modes is obtained with the use of the globally assembled dynamic stiffness matrix corresponding to a finite set of displacements for the described model. When the force vector is set to zero, the natural frequencies can be found from:

$$[\mathbf{K}]\{\upsilon\} = 0 \tag{6.9}$$

For cases when the natural frequencies can be determined from $\{\upsilon\} = 0$, rather than from $[\mathbf{K}] = 0$, the displacement happens to coincide with the nodes of the modes of vibration [133,134]. For the case under study and the frequency range of interest, the natural

frequencies are found solving the determinant of the dynamic stiffness matrix with the use of a systematic iteration technique to obtain the frequency values for which $[\mathbf{K}] = 0$. The results are also given in Table 6.2.

6.4.2 *Measurement of the Specific Damping Capacity*

Once the natural frequencies are analytically identified, we could proceed with the formulation derived in chapter 5 to obtain a measurement of the damping in the structure. Damping is defined with the notion of specific damping capacity, which is the ratio between the energy dissipated during one cycle of strain and the maximum strain energy stored in the material [135]. By introducing the loss tangent as the angle, ϕ, by which the stress leads the strain in a steady state harmonic excitation, one could express the specific damping capacity as:

$$\varphi = 2\pi \tan\phi = 4\pi \frac{\omega''}{\omega'} \tag{6.10}$$

The right most expression was previously derived in chapter 5. To implement Equation (6.10), a Taylor's series approximation of the analytically derived function, containing the viscoelastic effect of material damping, was also presented. After some simplifications, the final expression for the specific damping capacity can be found from the determinant evaluation of the following expression:

$$\left(\omega - \omega^{*}\right) = \frac{\left(\left(E^{*} - E\right)\frac{\partial f}{\partial E} + \left(G^{*} - G\right)\frac{\partial f}{\partial G}\right)}{\left(\frac{\partial f}{\partial \omega}\right)} \tag{6.11}$$

The partial derivatives of the function describing the dynamic behavior of the system are taken in terms of the elastic material properties. Therefore, the global dynamic stiffness matrix is assembled by assuming the material to be perfectly elastic. The viscoelastic material properties (indicated with a superscript asterisk) are obtained from the dispersive curve of the wave velocity previously measured. The evaluation of the derivatives is approximated with finite difference, and the total matrix obtained from the right hand side of Equation (6.11) is evaluated to find its determinant. By assuming the real part of the frequency to be much larger than the imaginary part, an expression for ω'' is found, and substituted into Equation (6.10), to obtain a measurement of the energy loss. A flow chart of this numerical procedure is given in Figure 6.4.

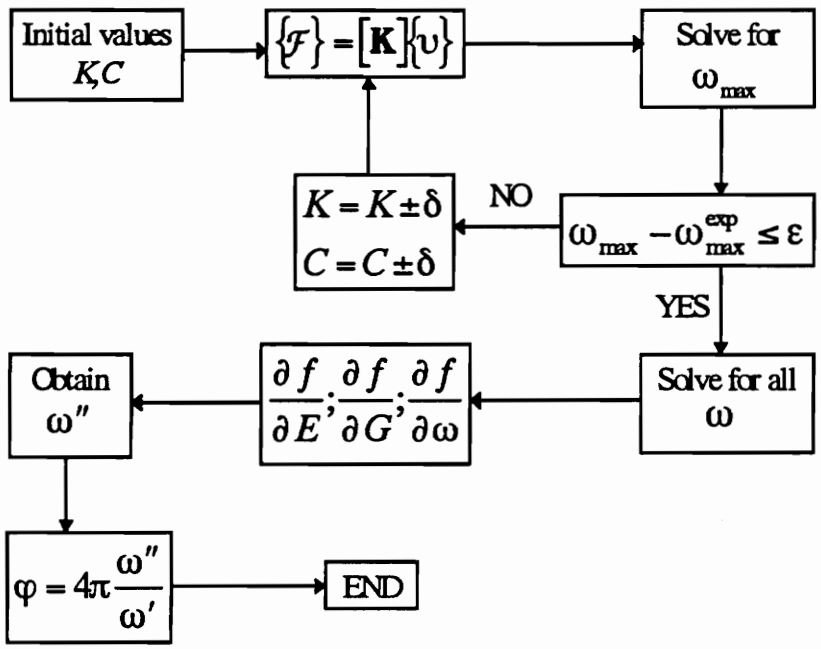

Figure 6.4. Flow chart of the numerical procedure used to obtain the average specific damping capacity of a structure for a given frequency.

This procedure is done for the 18 first natural frequencies of the system to account for the maximum energy dissipation possible given the frequency range of analysis (up to

3000 Hz.). The average value of the specific damping capacity of the system under study was found to be 0.0231, which it is within the order of typical aluminum structures [136-138]. For the sake of completeness, an experimental measurement of the energy dissipated was done in the frequency domain for harmonically excited systems using the half-power method. For this procedure, the specific damping capacity is related to the inverse quality factor, Q^{-1}, with the use of the following relation:

$$\varphi = 2\pi Q^{-1} = 2\pi \frac{\omega_2 - \omega_1}{\omega_n} \tag{6.12}$$

where ω_n is the resonant frequency found at the maximum amplitude of the response for a given peak, and ω_1 and ω_2 are the frequencies at which the amplitude of the response is 0.7071 of the maximum amplitude. Due to the extensive use of this method, details on the experimental procedure will be omitted [48]. The inverse quality factor was obtained from all the resonant peaks in the frequency range of interest, and after substitution into Equation (6.12), the average specific damping capacity of the system was found to be 0.02423. Therefore, the analytically measured energy dissipated was calculated with an error of 4.65 %, reassuring the accuracy of the numerical procedure derived in chapter 5.

6.5 *Comparison of the Energy Dissipation Mechanisms*

In studying the effects of localization of the propagating wave, we have concluded that the sensing region of a PZT actuator-sensor is concentrated in the near vicinity of the supplying source. This fact has been experimentally demonstrated, and through the use of one dimensional modeling, the phenomenon of localization has been related to the behavior of energy dissipation mechanisms [131]. Other factors typically considered, such as defects in assembly and manufacturing of the materials, are excluded due to the random

behavior of their nature. The energy dissipation mechanisms that we have considered are material damping and nonconservative joints, such as the bolted connection studied in this work.

To compare the contribution of energy dissipation of the two mechanisms under investigation, and thereby the propagation of the energy of vibration to a limited area from the inducing source, we have investigated the amplitude of the response as a function of distance for a given resonant frequency of the bolted beam modeled in this study. The results are graphically shown in Figure 6.5; distance 0 corresponds to the location of the PZT-actuator out-phase (see Figure 6.3), and it covers the segment from 0 to the right end of the beam. The amplitude of vibration is considerably larger before the joint than when the wave has encountered the discontinuity, after which, the wave sharply attenuates. At the bolted connection, the multiple reflections and the small size of the elements distort the smoothness of the propagating wave. By looking at the close-up of the vibration amplitude after the joint, we could see the uniformity of the response which, due to the short distance (86.0 cm.) and material properties of aluminum, does not show a significant attenuation of the propagating wave.

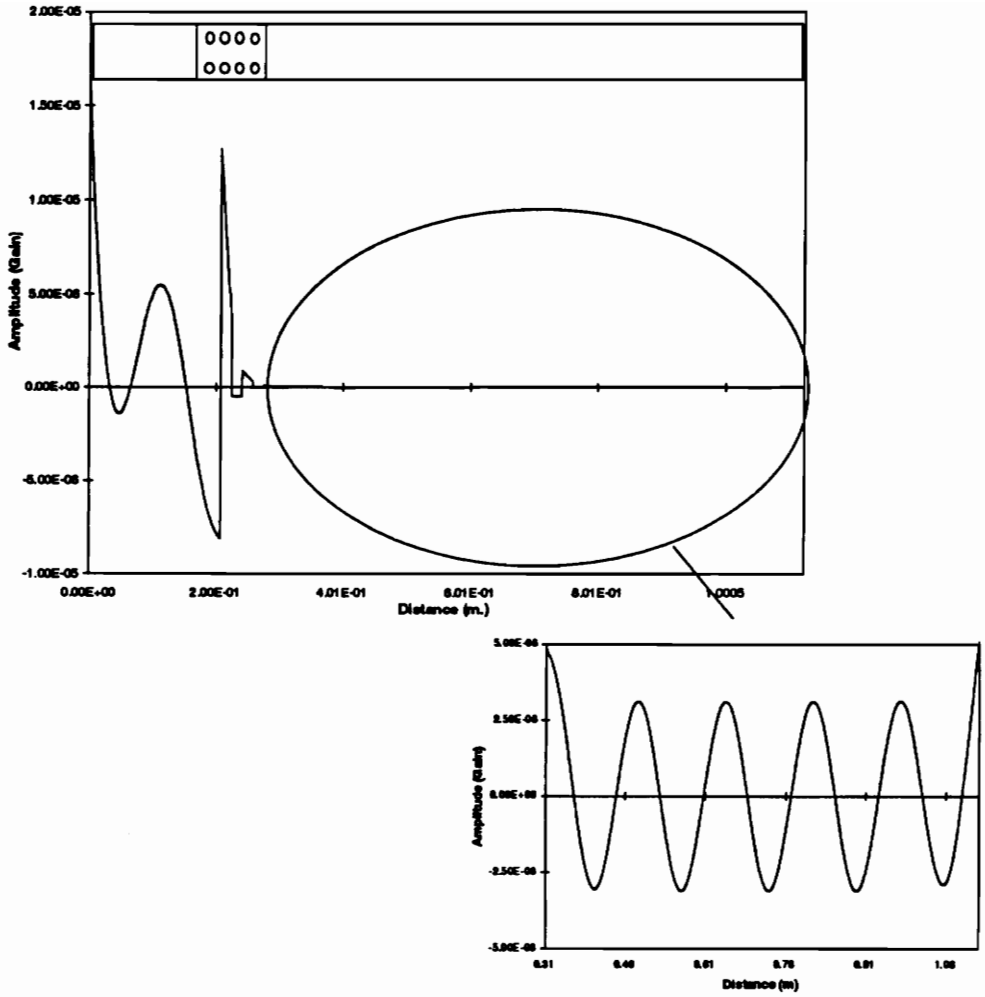

Figure 6.5. Attenuation of the propagating wave generated by the PZT actuator pair acting out of phase.

6.6 *Conclusions*

The motivation of this research is to analyze the effect of wave attenuation to have a better understanding of the phenomena of localization in the sensing region of a disturbance driven by a PZT actuator-sensor, which gives the point impedance of the structure and can be relied on to observe the incipient damage occurred in the system to which it is bonded. For this purpose, a methodology to study the effect of structural

damping in the dissipation of vibrational energy in structures has been here verified in an effort to correlate the energy dissipated and the sensing region localization phenomena.

The dynamics of a long bolted beam has been modeled at high frequency, using a spectral approach based on continuum mechanics. This methodology accounts for structural discontinuities, such as bolted connections, and lightly damped materials. The viscoelastic material properties are experimentally derived, using the wave speed of the propagating signal, and added into the formulation. The energy dissipated is given in terms of the specific damping capacity of the structure, which gives a measurement of energy dissipation. A scheme based on the correspondence principle to obtain an estimation of the specific damping capacity was derived in chapter 5 and it has been successfully applied and corroborated here. Introducing an effective analytical procedure to approximate the energy losses on one-dimensional structures.

A comparison of the importance of energy dissipation due to material damping and due to structural joints has been also addressed. For the system under study, the effects of material damping are hardly visible, while the energy dissipated due to the bolted connection is easily observed. For material damping to become a more significant contributor to the energy dissipation of the propagating wave, a longer and highly damped beam should be considered. But material damping need to be accounted for to obtain a realistic response of the structure. The specific damping capacity obtained is a combination of energy dissipation due to the factors encountered in the modeling of the structure; that is material damping and structural joints. It has been shown that energy localization of the induced propagating wave is most clearly manifest at structural bolted connections.

Chapter 7

Parametric Study on the Sensing Region of a Driven PZT Actuator-Sensor

7.1 *Introduction*

A health monitoring technique, which uses integrated piezoceramic (PZT) actuator-sensors to track the high frequency point impedance of the structure to identify incipient type damage, has been studied at the Center for Intelligent Material Systems and Structures, and introduced in earlier chapters. It has been shown that the sensing area of the PZT actuator-sensor is localized to its near vicinity, and therefore making this technique very reliable to detect damage within a given region, without being affected by the far field loading or the boundary conditions. An extensive modeling effort has been carried out to understand this localization phenomena, which has been attributed to the high frequency content of the technique, and the energy dissipation and attenuation mechanisms contributing to the weakening of the propagating wave's transmission.

A methodology has been derived for one dimensional structures with the use of a wave propagation approach based on continuum mechanics to model the high frequency vibrations of the structure with added energy dissipation mechanisms. Analytical and experimental procedures has been jointly implemented in order to obtain the necessary parameters needed to model the attenuation of the vibrational energy. Qualitative assessments on the PZT's low power induced wave, and its interaction with the structure and the dissipative and attenuating mechanisms considered in this study, will be here addressed.

Therefore, the purpose of this work is to apply the one dimensional model, previously developed [131,132,139,140], to the study of the various factors needed to be considered when attaching the integrated PZT actuator-sensor to a real structure for health monitoring. Factors that will be addressed in this parametric study are related to the material of the structure (thickness, stiffness, density, and internal damping), to the mass loading effect, to multi-member junctions, to discontinuities in cross-section, to material discontinuity, and to bolted connections. Of these factors, material damping and bolted joints are dissipative mechanisms, while the rest of the considered factors are attenuating mechanisms, due to their reflective nature. The effect of these factors on the interaction of the PZT actuator-sensor with the monitored structure will be reproduced through calculations of the electrical impedance of the system and the electrical gain across structural discontinuities. This parametric study will aid in the understanding of the PZT's induced wave behavior in the inspected structure, and the range of its sensing region. An impedance metric will be presented to compare the undamaged structure with that when damaged is present. Also, an attenuation metric, to quantify the decay of the propagating wave when attenuating mechanisms are present, will be here introduced. Simple experiments to corroborate the analytical findings will then follow.

7.2 *Interaction of PZT Actuator-Sensor with the Structure*

7.2.1 *Introduction*

After setting up, in the previous chapters, all the formulation needed to reproduce the PZT-host structure interaction, an extensive study of the factors that can affect the range of the PZT's sensing region will be here presented. These factors will be qualitatively observed with calculations of the electrical impedance and electrical gain of reproduced scenarios that can be encountered in real structures. By evaluation of one dimensional structures, good assessments on the wave behavior, excited by the PZT

source, could be attained. No additional information would be gained with the elaboration of more complex structures, not to count the analytical effort.

Since it is not possible to analyze all the circumstances that arise in practice, only the most common cases will be discussed through the introduction of attenuation and dissipation mechanisms. In this study only rectangular cross-sections would be taken into account, since true applicability of the PZT's geometry would be lost if any other type of cross-section was considered, that is for the one dimensional analysis. Beam elements of various lengths, cross-sectional dimensions and material properties with various elements that can influenced the localization of the PZT's induced wave, such as multi-member junctions, cross-sectional discontinuities, and bolted joints, will be presented. The reason to introduce such discontinuities is to observe the degree of reflection and energy dissipation of the incoming wave, and thus the energy propagating past the discontinuities. This wave-discontinuity interaction effect is responsible for the localization of the wave's energy and consequently the limitation of the PZT's sensing range.

7.2.2 *Material of the Structure*

The first factor to consider when bonding a PZT to a structure is the behavior of the impedance due to material properties; stiffness and density. Internal friction in the material is added into the formulation by assuming the material to be a Lovell-Kimball solid [126]. It is necessary to add material damping to the analysis to avoid infinite transmissibility of the response. Table 7.1 gives the material properties and loss factors coefficients for some of the most widely used materials in construction.

The rectangular cross-section of the free-free beams modeled has dimensions 5.08x1.27 cm., and a length of 3m., while the PZT actuator-sensor, bonded at a free-end, has dimensions 5.00x5.08x0.019 cm. Analytically, the low-power (approximately 6-8 mW) driven PZT actuator-sensor, which excites the structure at a constant voltage of 1 V rms., calculates the response translated to electrical quantities with the use of the

equations derived in chapter 4. The properties for the PSI-5A-S2 PZTs were used for this study, and they are given in Table 7.2.

Table 7.1. Mechanical properties of some of the most commonly used materials in construction [141].

Material	E (GPa)	Density (Kg/m^3)	Loss Factor	Poisson Ratio
Al 6061-T6	68.95	2715.0	0.001	0.33
Al 7075-T6	71.71	2795.0	0.001	0.33
Cast Iron (G.)	90.00	7550.0	0.001	0.2
Cast Iron (M.)	172.00	7550.0	0.001	0.2
Steel	210.00	7857.0	0.001	0.27
Oak	10.00	1000.0	0.010	-
Glass	60.00	2500.0	0.002	-
Light Concrete	3.80	1300.0	0.015	-
Plexiglas	5.60	1150.0	0.040	-
Dry Sand	0.03	1500.0	0.120	-
Dense Concrete	26.00	2300.0	0.008	-
Plywood	5.40	600.0	0.013	-
Cork	0.025	120.0	0.130	-
Graphite epoxy	80.00	1500.0	0.030	0.3
Brick	16.00	1900.0	0.020	-

Table 7.2. Properties of PSI-5A-S2.

Density (Kg/m^3)	Y_{11} (N/m^2)	η $\bar{Y}_{11} = Y_{11}(1+i\eta)$	d_{31} (m/V)	g_{31} (Vm/N)	ε_{33} (f/m)	δ $\bar{\varepsilon}_{33} = \varepsilon_{33}(1-i\delta)$
7650.0	63.00	0.001	-171.0e-12	-11.4e-3	1.5e-8	0.012

The pattern of the electrical impedance is first demonstrated with the selected metals on Table 7.1. The results are given in Figure 7.1: As expected, the largest amplitude of the electrical impedance corresponds to the stiffest material. Also, as the stiffness of the material increases, the impedance shifts to the right. The difference in density between aluminum and iron, is the cause of two distinct patterns, but since the stiffness, inertial and damping properties are included in the dynamic stiffness matrix, the effect of changing the stiffness and density is shown together in Figure 7.1.

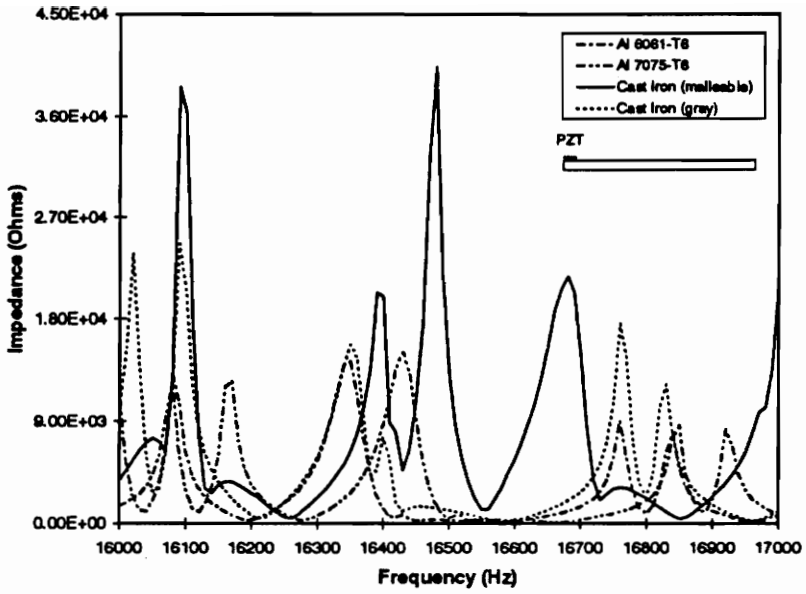

Figure 7.1. The Impedance shifts up and to the right for stiffer materials.

Due to the broad differences between the properties of some of the other materials given in table 7.1, similar results to those presented for the metals are given in two separate plots. Figure 7.2 shows the results for the materials with largest modulus of elasticity, the behavior of the impedance is as described before for the metals. But for the materials presented in Figure 7.2, the loss factors are different, this explains the different sharpness on the pattern of the impedance. Accordingly, the lower the loss coefficient, the sharper the response. For completeness, the rest of the materials used in this study are compared in Figure 7.3, similar findings can be deduced from these results. The frequency range for these plots is totally arbitrary. It has been shown that to significantly change the pattern of the impedance response, drastic changes in the properties of the material are required. This effect is due to the increase of internal reflection, which could be similarly observed, to a lesser degree, with a change in the cross-section.

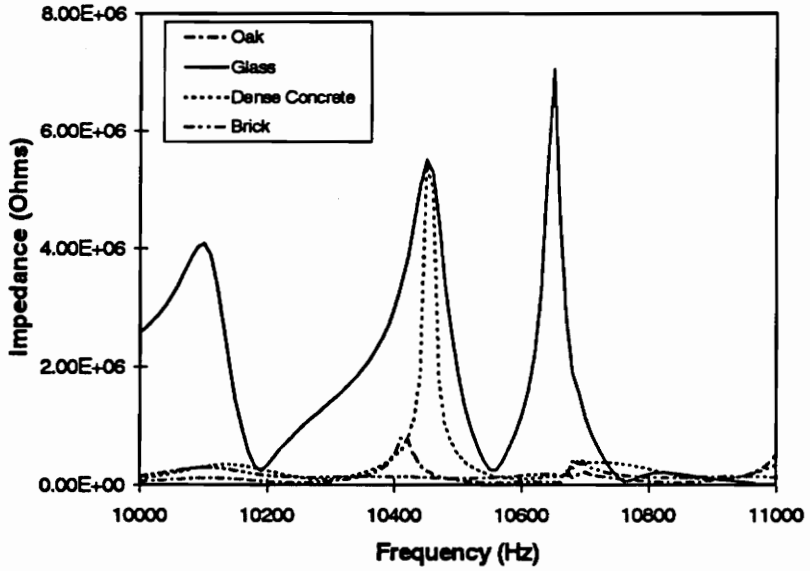

Figure 7.2. Sharper impedance is related to materials with lower loss factor.

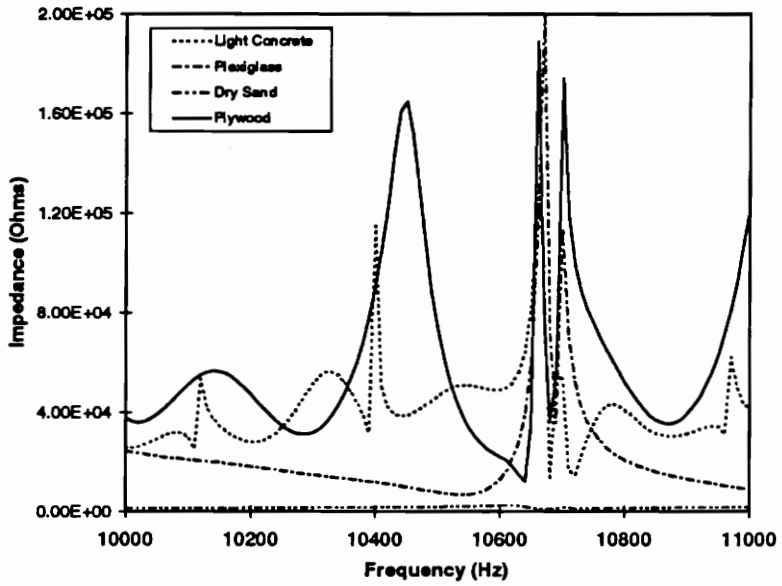

Figure 7.3. Dry sand is a highly damped material, giving a very shallow response.

To visualize the dissipative effect that material damping has on the PZT's induced wave, leading to the localization of the PZT's sensing region, the amplitude of the response for selected materials is calculated as a function of distance along the 3 m. long beam specimens used in this analysis. Figure 7.4 shows the amplitude of the response at

distance intervals along beam specimens of various materials having different loss factor coefficients. For more heavily damped materials such as plexiglas, brick, and graphite epoxy, the amplitude of the propagating wave decays more rapidly than for the other materials shown. For metals, such as steel, the attenuation is not noticeable. These plots are helpful to identify the dissipation of the PZT's energy in a material with no other retarding mechanism that the dissipation delivered by the internal friction. With these findings, one could have a better insight on how many PZTs would be needed to monitored structural members with no discontinuities.

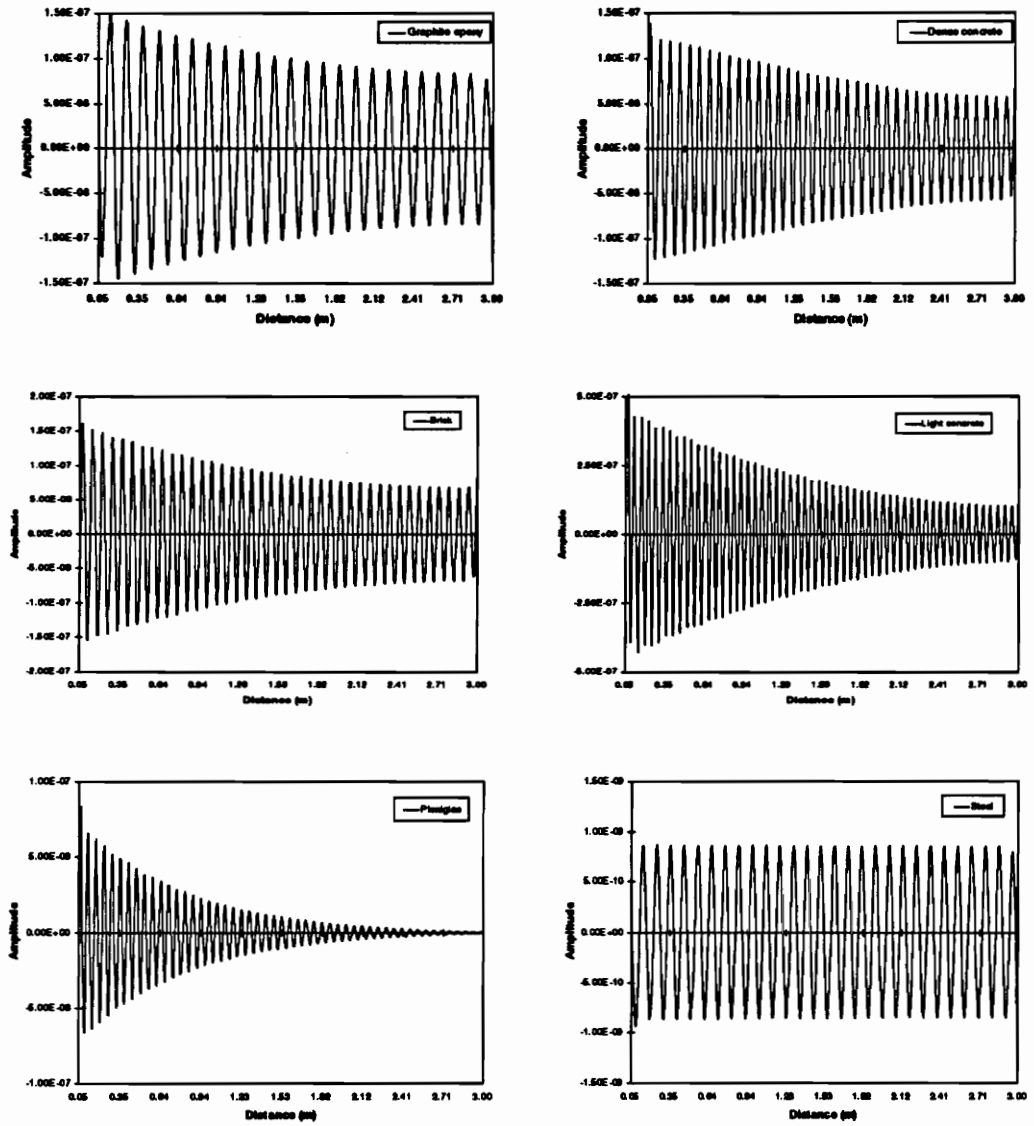

Figure 7.4 Gain vs. distance for selected materials of various loss factor coefficients.

7.2.3 *Material Discontinuity*

A concrete beam of length 65 cm is connected to another concrete beam of length 60 cm by an intermaterial 20 cm long compose of different materials, all having a cross-sectional area of 5.08x1.27 cm. A PZT (PSI-5A-S2), 5x5.08x0.019 cm, is bonded at one end of the free-free arrangement. The connection of this structural arrangement is considered to be perfectly welded. The results are shown in Figure 7.5, where soft intermaterials, such as cork and dry sand, and a hard intermaterial, such as steel, are compared with the response of the structure if the intermaterial was a continuation of the concrete structure. As expected, the soft materials provided a large attenuation in comparison with steel, which actually increased the amplitude of the impedance with respect to the full concrete beam. This effect is clearly due to the increase in stiffness that the steel provides to the system. The two insulating materials, cork and dry sand, have similar stiffness, but cork has a much larger loss factor coefficient than sand (see Table 7.1), and therefore it has an even larger attenuating effect on the propagation of the excitation, and thus showing a shallower impedance.

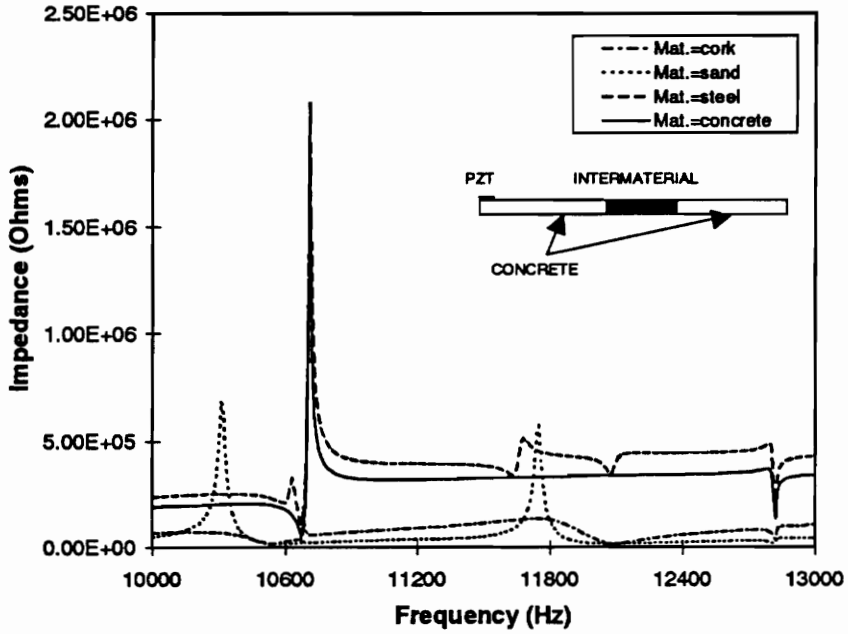

Figure 7.5. Impedance of a concrete beam with different intermaterials.

7.2.4 *Effect of Mass Loading*

The effect of mass addition in the structural response is the combined action of adding a rigid joint that blocks the propagating wave and adding a lumped mass into the structure. By adding a rigid joint, reflection and transmission of the incident wave at the mass discontinuity will occur, but the mass-joint will also act as a source of new waves, thus generating new longitudinal, bending, flexural and even torsional waves. In this study, we are just interested on impedance and gain calculations based on the strain computed at the PZT location, and therefore no distinction of the generated waves at the joint will be made. The main parameters to consider when adding a lumped mass into the model is the density of the material and its geometry. For a frequency of 100 kHz the wavelength would roughly be 1.6 cm, a considerable size, and therefore very little additional information would be gained by including the exact shape of the joint into the analysis.

The effect of an end-mass, for the clamped-free beam used in this study, is shown in Figure 7.6. It has a PZT bonded at a distance 20 cm from the fixed-end, and a lumped ball-mass at the free-end. The total length of the beam is 60 cm and its cross-section is 40x6 mm. The material used for the beam is Al 7075-T6 and the PZT properties and geometry are as described in section 7.2.2. Calculations of the electrical impedance when there is no mass are first made, then by adding mass the amplitude of the response decreases. This vertical effect suffered by the electrical impedance with the addition of mass can at first sight be explained by the fact that mass addition into the system lowers the diagonal terms of the dynamic stiffness matrix, reducing the amplitude of the response. Also, it should be noticed that this shift is frequency dependent and that at higher frequencies the addition of mass becomes more significant.

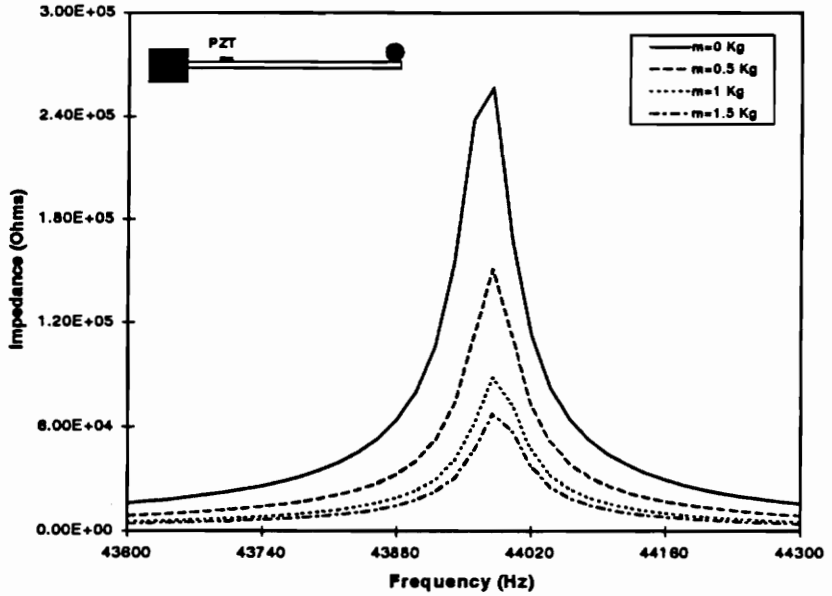

Figure 7.6. Effect of an end-mass on the impedance.

To observe the blocking effect of rigid conservative joints in the attenuation of the wave, a ball-mass was encrusted in a 1.5 m. clamped-free beam at a distance of 0.5 m. from the free-end. A PZT-actuator was located 0.2 m. from the clamped-end, and the response was calculated by a PZT-sensor, placed after the ball-mass at 0.3 m. from the free-end, as the gain of the structure across the added concentrated mass. Figure 7.7 shows the gain calculated after the added ball-mass discontinuity when it has a radius of 1.25 cm. and a total mass of 1 Kg, and then when it has a radius of 1.35 cm. and a mass of 2 Kg. The attenuation of the transmitted wave is appreciable. Due to the frequency dependence of the added concentrated mass, this attenuation becomes even more significant at higher frequency.

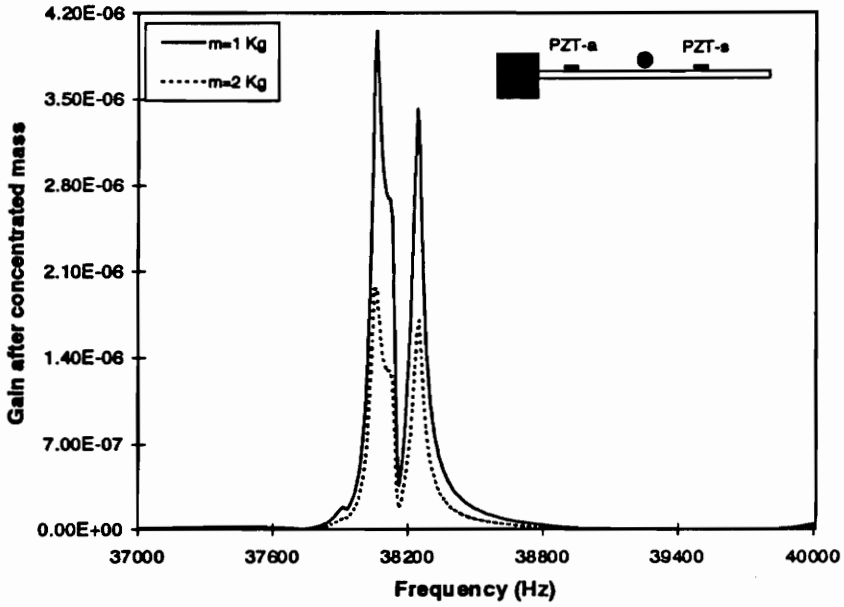

Figure 7.7. Wave attenuation observed by a concentrated mass.

The addition of mass, as the loading effect that it has on a structure, is a source of incipient damage, that could lead to catastrophic failure. To identify this source of damage, an impedance damage metric has been presented [1-3]; it consist on evaluating the difference squared of the vibrational response of a healthy structure with that when damage is present. The same configuration as that shown in Figure 7.7 is used to introduce this measuring tool. Figure 7.8 gives the damage metric as a function of the ball/beam mass ratio. A metric value of 0 corresponds to no damage, no mass added, while a value of 1 corresponds to the maximum damage considered, that is when the added mass has the same weight than the beam member inspected. In this manner, when the impedance damage metric reaches a threshold value, replacement of the component is necessary.

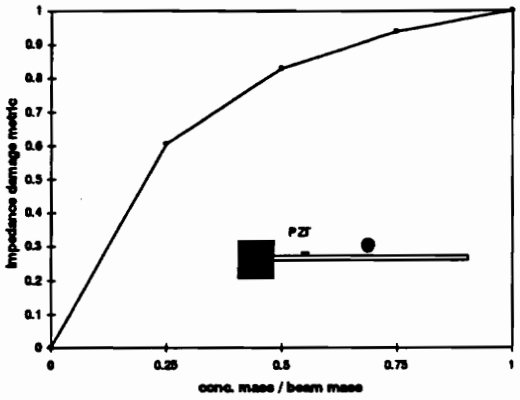

Figure 7.8 Impedance damage metric curve for mass addition in a structure.

7.2.5 *Discontinuity of Cross-Section*

Changes in cross-section have a direct effect on the impedance, such discontinuities act as a source of reflected waves, localizing the sensing range of the induced wave. The beam elements used are Al 7075-T6, perfectly welded together at the middle, with free-free boundary conditions, and each having a length of 50 cm. A PZT actuator-sensor is bonded at the free-end of the smallest cross-sectional beam element. Figure 7.9 shows calculations of the impedance for discontinuities having cross-sectional ratios of 2,4, and 16. Beam 1 has an unchanged cross-section of 40x6 mm, while beam 2 varies cross-sections accordingly. As the ratio increases, the amplitude of the impedance increases, more clearly observable by the baseline of the response. This effect is due to the fact that as the cross-sectional ratio becomes larger, the reflection at the conservative massless discontinuity increases, and therefore more energy flow will be calculated by the PZT as strain energy flow reflected from the perfectly welded junction.

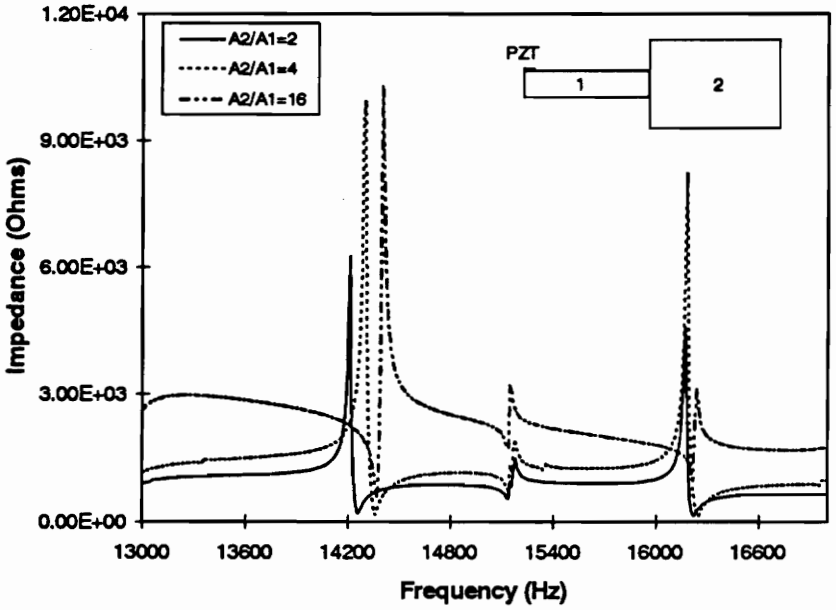

Figure 7.9. Impedance for different ratios of cross-sectional discontinuities.

To observe the blocking effect that a discontinuity in cross-section has on the propagating wave, calculations of the gain before and after the discontinuity for a cross-sectional ratio of 2 are given in Figure 7.10: The attenuation is clearly appreciable even for a small cross-sectional ratio difference. Therefore, reinforcing the fact that discontinuities in cross-sections are sources of multiple reflections, thereby affecting the transmission of the propagating wave across the discontinuity. When placing PZTs for health monitoring in areas of cross section difference, care need to be taken about the degree of reflection at the discontinuity; therefore an attenuation metric is here introduced as a measuring tool of the induced wave's transmission. Figure 7.11 shows the curve for such metric; a value of 0 corresponds to no cross sectional discontinuity, while a value of 1 is the highest ratio that one could encountered in most common case scenarios, a cross-sectional ratio of 4. The values used to represent this curve are taken from the difference squared of the gain after the discontinuity when there is no cross-section change, full transmission case, with that when there is cross-sectional difference, for a frequency range of 20-30 kHz. Due to reflections at the perfectly welded junction, the sensing range of the PZT actuator-sensor

is attenuated to different degrees depending on the cross sectional difference at the discontinuity.

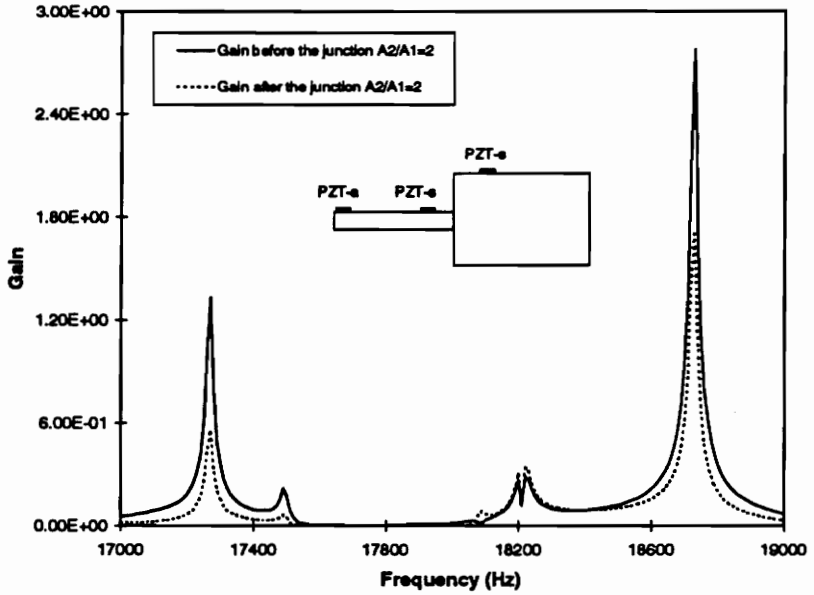

Figure 7.10. Gain calculations to show the attenuation of the transmitted wave due to cross-sectional discontinuity.

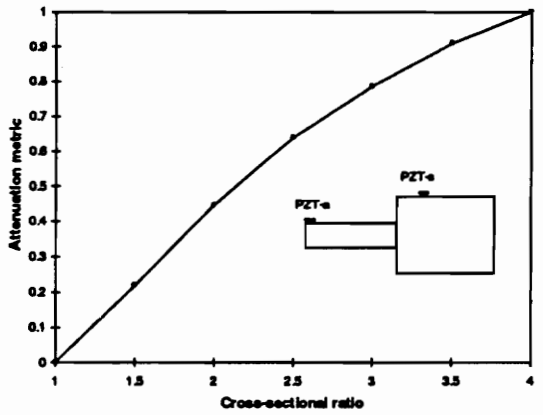

Figure 7.11. Attenuation metric of a stepped beam. The maximum cross-sectional discontinuity considered is 4.

7.2.6 *Multi-Member Junctions*

A study of the wave behavior at multi-member junctions will be here presented. A special interest will be emphasized on the gain of the structure obtained by varying the angle of orientation of the respective members in reference to a fix member.

7.2.6.1 *Junctions with Two-Members*

For this case a member is fixed flat and the other is oriented at different angles theta; 180°, 135°, 90°, and 45°, with respect to the flat member. A PZT, 3 cm long, is placed at one end of the free-free two-members configuration. The material properties of Al 6061-T6 was assumed for the beam elements. The flat beam has a length of 1.03 m and the oriented beam a length of 1.9 m, both having cross-sectional areas of 2.54x0.635 cm. The junction is assumed to be a rigid mass joint. The gain of the structure is calculated at a location 10 cm from the junction in the angled beam member. The results are shown in Figure 7.12. The gain, as calculated on beam 2, gives an estimate of the influence of the angle orientation on the transmission of the propagating wave. From Figure 7.12 it could be concluded that at an angle theta of 180° the wave has the best transmission, while at acute angles of member 2 with respect to the incoming propagating wave is the worst case scenario for wave transmission. Furthermore, the theory shows that as beam 2 is oriented at angles deviating from the horizontal line, the transmitted longitudinal waves attenuates rapidly, this effect is even more pronounced for angles theta ranging between 0°-120° with respect to the incoming wave. Therefore, the energy transmitted at a two-member angled junction is affected by the transmission of the longitudinal waves. The effect of angle orientation on the propagating wave could be use to detect a sort of incipient damage based on the bending of a member. This aspect will be treated in section 7.3 with the aid of a simple experiment to reproduce a damage metric.

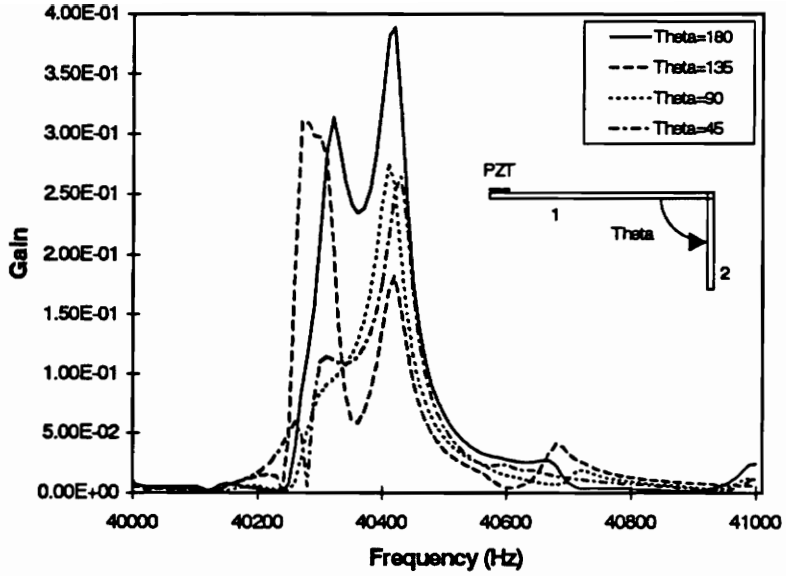

Figure 7.12. Effect of angle orientation on the wave's transmission of a two-members junction.

7.2.6.2 *Junctions with Three-Members*

The three-members configuration is done with the same beam elements as those described in section 7.2.6.1, but an extra member, of length 1.2 m and same cross section, is added at an angle theta. Beam 1 and 2, see Figure 7.13, are flat, while beam 3 assumed a 135° and 90° angle orientation. The gain of the structure 10 cm from the junction on beam 3 is calculated, and the results are shown in Figure 7.13 for two different angle orientations of beam 3. At theta 90° the wave is most optimally transmitted for three-member junctions, and attenuates away from the right angle orientation. The theory predicts that the 0° orientation of beam 2 with respect to beam 1 shows greater orientation effects (more interaction) for any angle orientation of beam 3, than when beam 2 is at 90° angle with respect to beam 1.

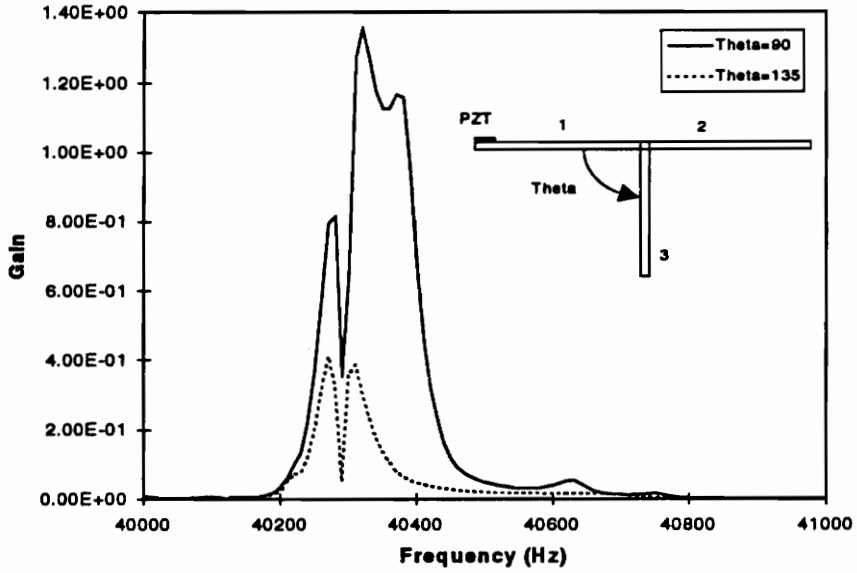

Figure 7.13. Effect of angle orientation on the wave's transmission of a three-members junction.

7.2.7 *Effect of Bolted Joints*

Unlike the previously discussed conservative joints, bolted joints are considered to be the major source of energy dissipation in a structure. Therefore, besides the localization of the propagating wave due to the multiple reflections that occur at attenuating mechanisms, bolted joints add a dissipative effect, which localized even further and to a greater degree, the PZT's induced wave. The nonlinear joint model described in chapter 3 will be used in this study, and the boundary conditions involving frictional energy dissipation will be considered. Impedance and gain calculations are made for different bolt materials and diameters, bolted at different tangential shearing forces at the interface to investigate the dynamic response of the structure influenced by the transfer behavior of bolted joints.

7.2.7.1 *Two-Members Bolted Joint*

Two Al 6061-T6 beam elements of cross section 7.62x2.54 cm are bolted together with a single bolt; one member, of length 1.05 m, assumes a flat orientation, and the other

beam, 1.9 m long, is lifted at an angle 45° from the zero axis. The free-free configuration has a 5 cm long PZT bonded at the free-end of the shorter beam. The inertial properties of the bolt are approximated by its density and geometry; therefore the mass of the bolt is given by $\rho_b \pi d_b^2 l_b/4$, and the mass moment of inertia is given by $m_b l_b^2/8$; therefore knowledge about the density and size of the bolt used is needed to obtain these parameters. The stiffness of the surfaces in contact represented by the Coulomb stiffness term, K_j, is defined in terms of the stiffness of the bolt itself, which can be approximated by $\pi d_b^2 E_b/4L$, where L is the total transverse length of the bolted section, and it depends on the strength of the bolt used for the joint. The clearance stiffness was approximated using a cubic nonlinearity as shown in Figure 3.3a; due to the cubic relation between the force and displacement, for small values of K_{CF} close correlation with the nonlinear piece-wise behavior of the clearance at the bolt-hole section can be attained, thereby a value of 10 N/m^3 is assumed for all the cases. The clamping pressure is given as a function of the normal clamping force, f_N, and the surface roughness of the interface is given according to the coefficient of friction, μ.

The material of the bolt is first compared by assuming a fix value for the tangential force at the matting surface given by the clamping force and the coefficient of friction, and a bolt diameter of 1.27 cm. The impedance values are given in Figure 7.14 for the frequency range shown. The material of the bolt does not significantly affect the impedance, even for the drastic difference on stiffness and density of the bolt materials shown. To observe the effect of bolt diameter on the attenuation of the propagating wave, calculations of the gain 25 cm before and 25 cm after the bolted joint are made for two different sizes of bolts made of the same material; one having a diameter of 1.27 cm and the other joint made of two bolts each 2.54 cm of diameter and bolted in parallel. The results are given in Figure 7.15; as it can be clearly deduced from this plot, the amplitude of the response after the joint is much lesser than before the joint, but this effect is even more pronounced for larger size of bolts; in which case, the amplitude of the response

before the joint increases as the effect of larger reflection, while the amplitude after the joint decreases as less energy of the wave is transmitted through.

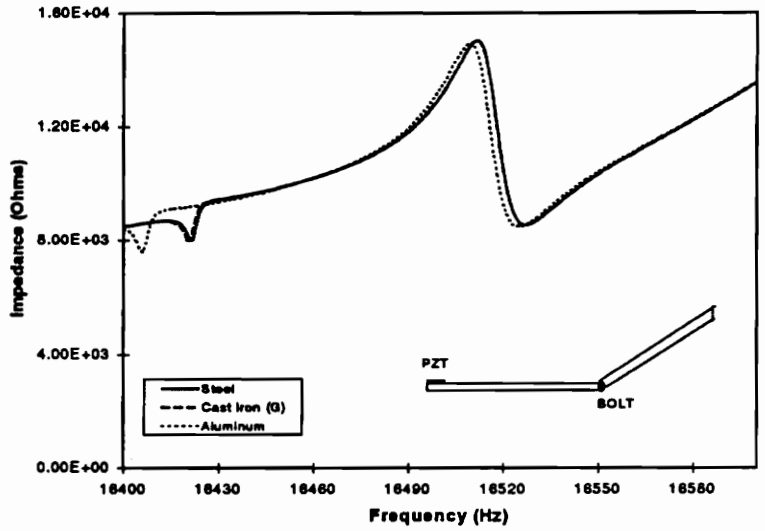

Figure 7.14. The effect of bolt material on the impedance of a two-member bolted joint.

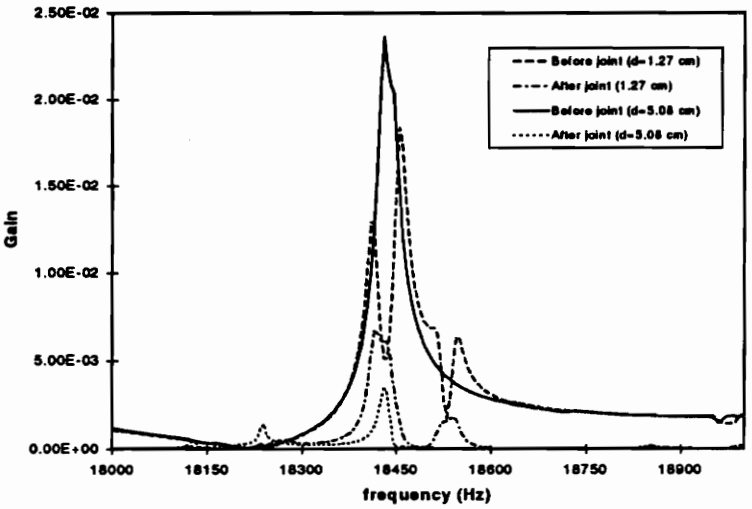

Figure 7.15. The effect of bolt diameter on the gain before and after the bolted joint of a two-member structure.

Another factor to consider is the finishing of the surfaces in contact. It should be understood that tracking the coefficient of friction when the bolt is subjected to dynamic loading is a tremendous task even if frequencies contained in the first mode of vibration are only considered. A more slippery surface finishing is related to a lower coefficient of

friction value, thus encouraging sliding. For fix clamping forces: Assuming the same coefficient of friction, the greater energy dissipation is related to the higher cyclic peak; for varying coefficient of friction, and a given cyclic peak, the greater energy loss is related to the lower μ. Calculations of the impedance for varying μ with fix bolt tension and the other way around, gave inconclusive results on the true effect of each of these factors for separate on the wave behavior. Accordingly, the coefficient of friction and the clamping force can not be possibly separated when the bolted structure is under cyclic loading, and therefore knowledge of the shearing forces at the joint interface should only be considered to account for both; normal clamping force of the bolt and coefficient of friction of the matting surface. Therefore, the energy dissipation at the bolted joint is proportional to the product of the shearing force and the relative tangential motion. When the joint is under high pressure, the relative motion is small, and under low pressure, the shear force is small.

An important source of incipient damage arises from the weakening of bolted connections, which is hardly detected with the use of conventional NDE techniques. Therefore, to stress this factor, an impedance damage metric is here presented: The two-members bolted configuration previously described is analyzed for three different size of bolts. The impedance is first calculated, for each bolt size, when the bolt is fully tight, then the tightness of the bolt is progressively reduced, and the impedance is computed for each case. The effect of loosening the bolts is simulated by decreasing the Coulomb stiffness and the shearing force: 10% reduction is considered to be maximum damage, while 0% is no damage (full tightness). The metric is computed in the same fashion as before: Difference squared of the impedance calculated for fully tight bolt with that when the bolt is being loosen. Figure 7.16 shows the curves representing the damage metric for three different size of bolts. The larger the bolt, the lesser effect that a loose bolt has on this damage metric. When monitoring bolted connections, measurements of the bolted section are made for a full tight bolt scenario, any posterior reading that shows any deviation from the healthy case recordings would be compared with the damage metric shown in Figure

7.16, and conclusions on whether the weakening of the inspected bolt has gone to far can be drawn based on a pre-set threshold value.

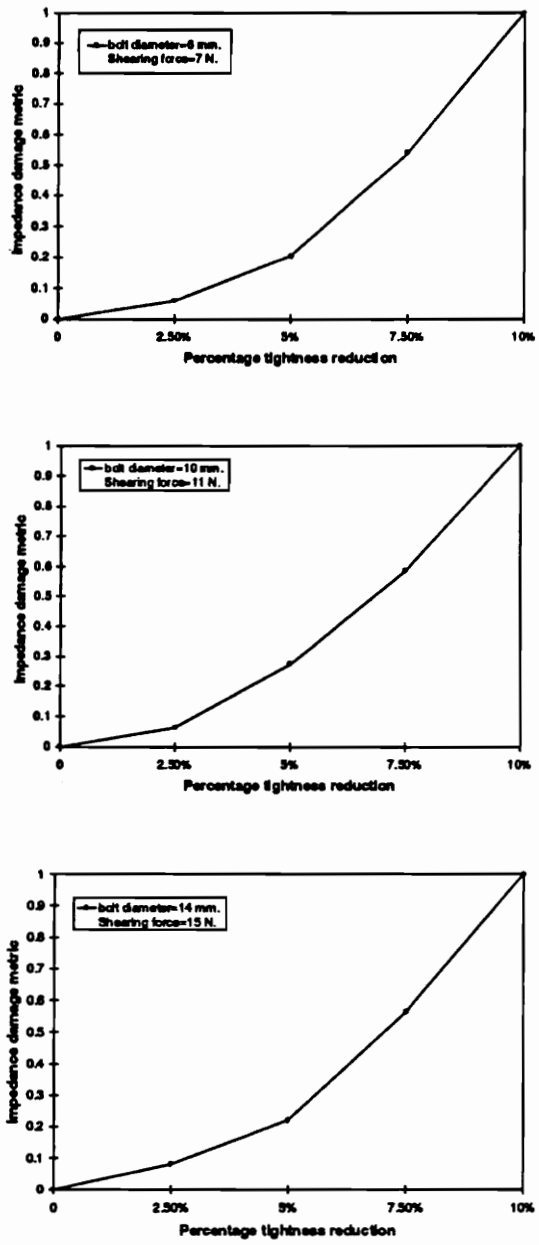

Figure 7.16. Damage metric for different size of bolts having different degree of tightness. 10% reduction from the fully tight case is considered maximum permissible damage 1.

7.2.7.2 *Three-Member Bolted Joint*

The three-member bolted joint is arranged in the form of an equilateral triangle. The material used for the 1 m long beam elements is Al 6061-T6, and the cross-sectional area is 7.62x2.54 cm. The junction is made with single steel bolts having each a diameter of 1.27 cm, and a total shearing force at the matting section of 22 N. The results are shown in Figure 7.17: The impedance was calculated when the bolts were all tight and then when bolt 2 and bolt 3 were separately loosen, reducing the tangential shearing force and the coulomb stiffness by 5%. By loosening bolt 2, the impedance decreases, indicating that larger amount of energy is been dissipated through the bolted joint, and this effect is readily detected by the PZT actuator-sensor due to its proximity to this bolted junction. On the other hand, by loosening bolt 3, the change in impedance is not observable (it follows the same pattern as if no bolts have been loosen), indicating the insensitivity of the PZT actuator-sensor to far field activity. To visualize the energy losses occurred when bolt 2 is been loosen, Figure 7.18 shows the gain of the structure at beam 3 (10 cm from bolt 3) when bolt 2 is tight and when it has been loosen. The attenuation of the wave in beam 3, when bolt 2 is been loosen, is considerable. This attenuation can be translated into a localization of the induced wave, which is highly influenced by the tightness of bolt 2.

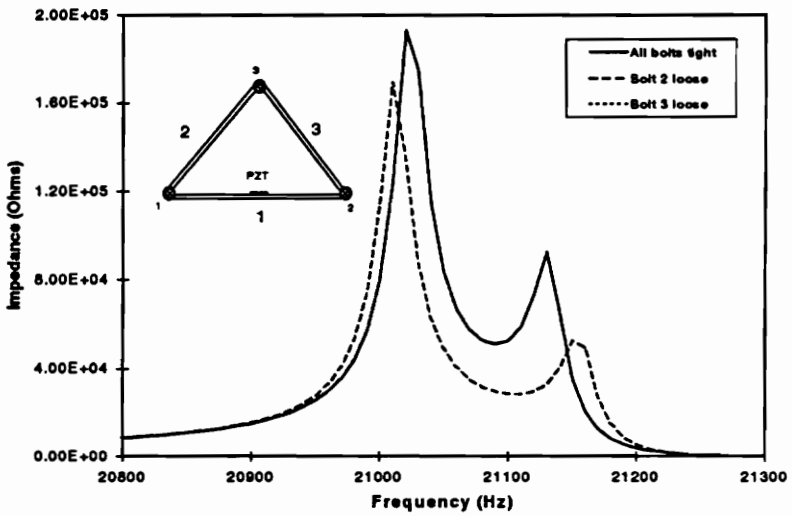

Figure 7.17 Impedance of a three member structure. When bolt 3 is loosen, the impedance response follow the same pattern as if all the bolts were tight due to the insensitivity of the PZT.

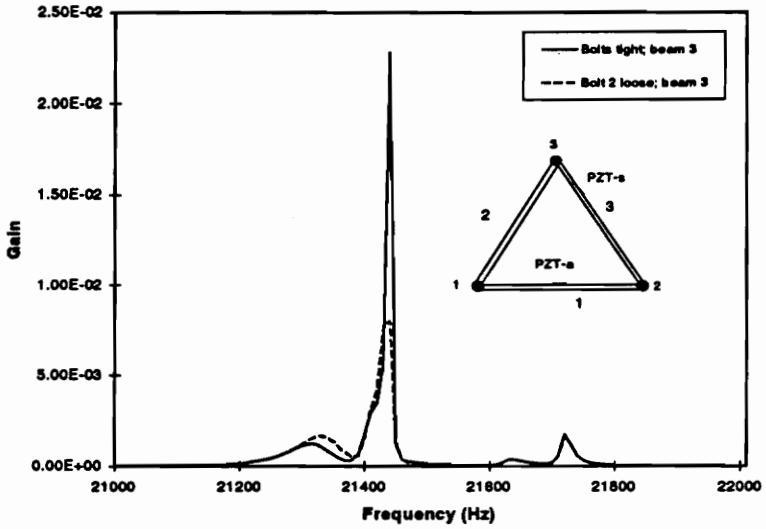

Figure 7.18. Gain of beam element 3 when all the bolts are tight and when bolt 2 is loosen.

7.2.7.3 *Four-Member Bolted Joint*

The four-member bolted joint is arranged in a square configuration, bolted at each corner with two steel bolts in parallel. Each bolt has a diameter of 2.54 cm, and the same parameters as described in section 7.2.7.2. The beam elements are also assumed to be Al 6061-T6 and each has a length of 1 m. and a cross section of 7.62x2.54 cm. Impedance of the square-bolted system when all the bolts were tight and when all the bolts were loosen by 5% (in the same manner as described in section 7.2.7.2) are shown in Figure 7.19. The decrease in impedance amplitude is primarily due to the effect of loosening bolts 1 and 2 and in less proportion due to the two right angle junctions. Due to the size of the bolts and the close-loop of the square configuration, large reflections occurred, explaining the small change in impedance, besides the fact that the bolts were slightly loosen. To look at the energy dissipated through the bolted joints, a calculation of the structural gain, when all the bolts were tight, at beam 1 (10 cm from joint 2), at beam 2 (10 cm from joint 3), and at beam 3 (10 cm from joint 4), was done for the same frequency range as that shown in Figure 7.19. It was found that the average total amplitude of the response at beam 1 is 50 times higher than for beam 2 and 3170 times higher than for beam 3. Therefore in a close-

square-bolted structure, the energy dissipation is indeed very large and the propagating wave is severely attenuated at each bolt and right angle junction, even though the reflections at the joints made the impedance to vary to a lesser degree.

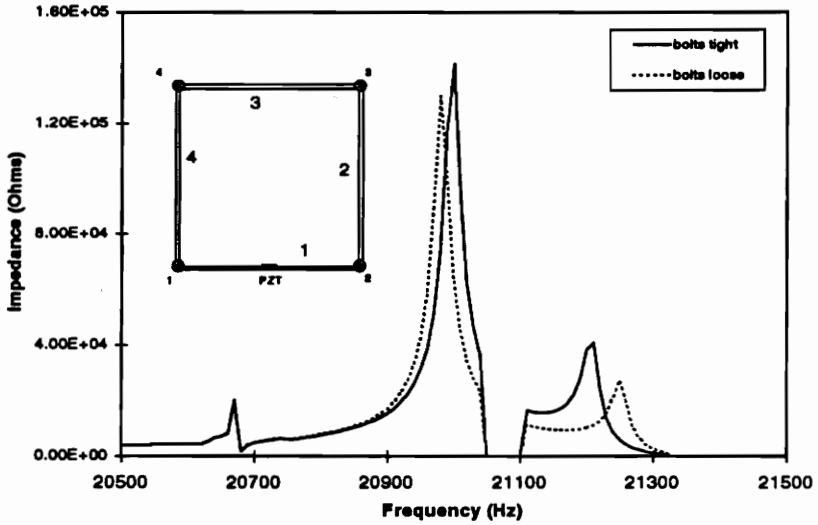

Figure 7.19. Impedance of a four member structure.

7.2.7.4 *Sensing Range of Multi-Member Bolted Configuration*

To effectively visualize the sensing region of a PZT actuator-sensor, three multi-member configurations have been assembled and compared. These structures are shown in Figures 7.20a-c; all are made of Al 6061-T6 and have a cross-section of 2x1.5 cm. The PZT actuator-sensor is placed at the free-end of the cantilevered structures and it has dimensions 3x2x0.19 cm and the material properties given in table 7.2. The structure shown in Figure 7.20a is first analyzed; in which three beam elements each of length 50 cm are bolted together. The bolts used have a diameter of 1.5 cm, and a total shearing force of 26 N. To demonstrate the sensitivity of the PZT to damage, a crack is simulated at a distance 25 cm from the clamped end. The presence of the crack adds flexibility to the structure; this localized change in stiffness has been approximated with a torsional spring, given in terms of the crack-length versus beam-depth ratio and material properties, and having the correct limits that the torsional stiffness is infinite for zero crack-length and zero for a crack-length of the same size as the beam-depth. Details of the torsional spring

coefficient used for this analysis are given in [142]. The same limit behavior is considered when assembling the model of the crack into the dynamic stiffness matrix.

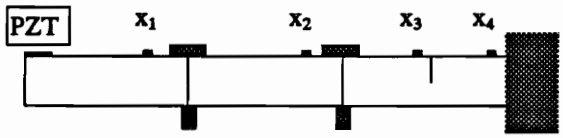

Figure 7.20a. Cracked structure with two bolts.

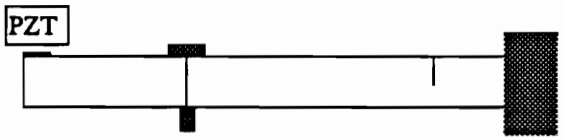

Figure 7.20b. Cracked structure with one bolt.

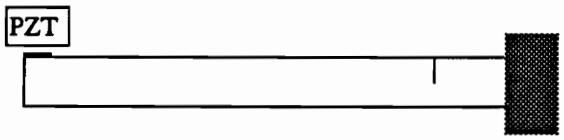

Figure 7.20c. Cracked structure with no bolts.

Gain calculations on the arrangement shown in Figure 7.20a were done 10 cm before the bolt closest to the free-end, x_1, and 10 cm before the inner bolt, at x_2. The response at these two locations was calculated using a crack-depth ratio, a/h, of 0.1. The results are given in Figure 7.21; the attenuation of the propagating wave across the joint is consistent with the findings of section 7.2.7.3 (one order of magnitude for the first bolt).

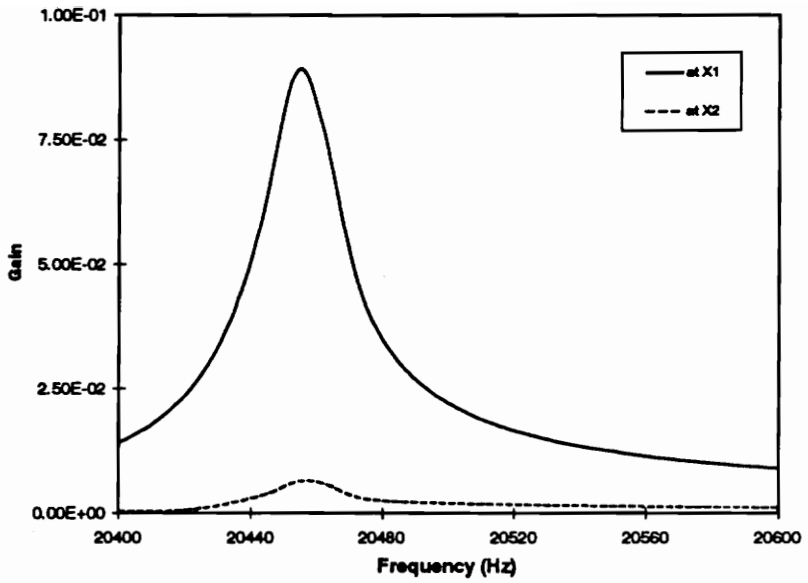

Figure 7.21. Gain of the structure at the locations shown in Fig. 7.20a.

Further calculations of the response at a location 10 cm from the clamped-end, x_4, were also made for different crack-depth ratios, the results are shown in Figure 7.22. The attenuation of the propagating wave after two bolts, even when compared to a relatively small crack length of 0.1, is very significant (as it was concluded from the gain calculations of the square-bolted configuration), this can be observed by comparing the magnitude of the gain in Figure 7.22 with that in Figure 7.21. The PZT's induced wave is largely localized not only due to the two bolts, but also due to the increase in crack size, being this a large source of multiple reflections. This fact is further addressed in Figure 7.23, this time and for comparative purposes, a smaller bolt of 0.75 cm. diameter and a total shearing force of 16 N was used. The use of weaker bolts can be visualized in the larger amplitude of the response when compared with the results of the same crack sizes shown in Figure 7.22. Calculations of the gain at x_4 and at the location 10 cm before the crack, x_3, are shown for two different crack sizes. As expected, with a larger crack size, the reflections would increase and therefore the gain calculated at x_3, while the gain at x_4 would decrease due to a lesser transmission of the incident wave's energy.

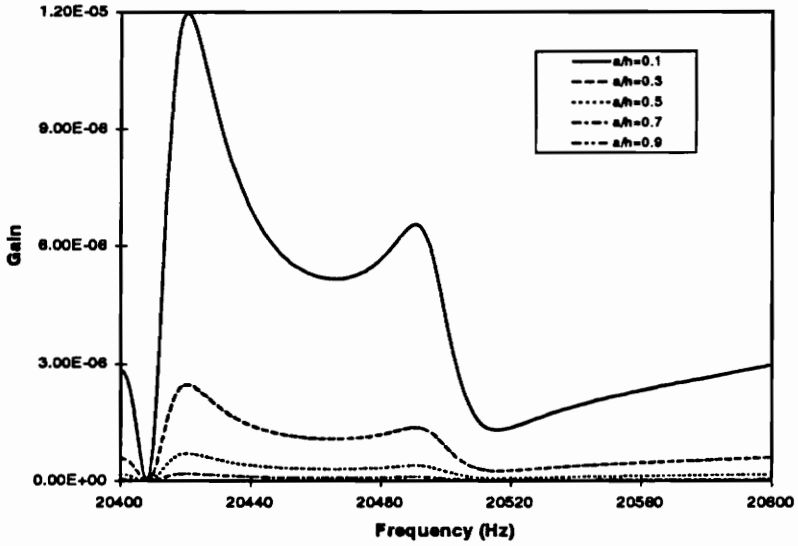

Figure 7.22. Gain of the structure at x_4 (Fig. 7.20a) for different crack sizes.

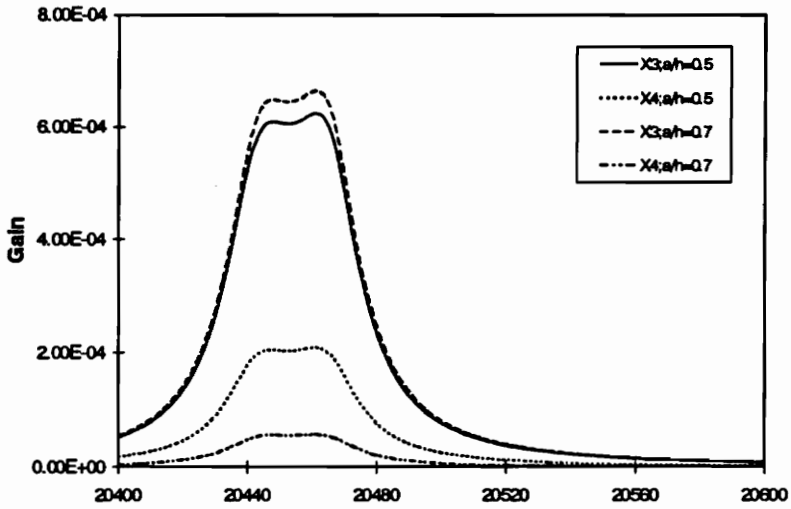

Figure 7.23. Gain of the structure at the locations shown (Fig. 7.20a) for two different crack size.

After a brief visualization of the energy losses due to the attenuation of the propagating wave interacting with the discontinuities presented in the structure shown in Figure 7.20a, calculations of this system's impedance are now presented. Figure 7.24 shows the calculated electrical impedance of this structure for different crack sizes and using bolts of 1.5 cm diameter and a shearing force of 26 N. The impedance calculated

from the PZT is not sensibly altered by the damage occurred two bolts away, that is the increase in crack size. This striking result is backed with the impedance given in Figure 7.25 for the structure shown in Figure 7.20b and in Figure 7.26 for the structure shown in Figure 7.20c. In Figure 7.25, the effect of crack size still hardly visible, even though there is just one bolt between the PZT actuator-sensor and the origin of the damage (note that a strong bolt is used in the connection). But, nevertheless small variation in the impedance amplitude is observed when the crack size is drastically increased. On the other hand, Figure 7.26 shows the variation of the impedance with crack size when no bolts are present in the structure: As it can be seen, variations in the crack size are detected by the observed change in impedance, which actually decreases with an increase in crack size. These plots show the sensitivity range of a PZT actuator-sensor and the localization of the induced wave when encountering an energy dissipating joint. Moreover, an impedance damage metric was constructed from the effect that the crack size has on the impedance. Accordingly, a crack-depth ratio of 0 is considered no damage and a ratio a/h of 0.9 is considered failure of the member. As before, this damage metric was calculated as the square difference of the impedance when there is no damage with that when the crack is present. The impedance were calculated assuming the system shown in Figure 7.20c; the damage metric curve is plotted in Figure 7.27. It could be observed that after a crack depth ratio of 0.3 the damage sharply increase, and replacement of the cracked member would be necessary to avoid its failure.

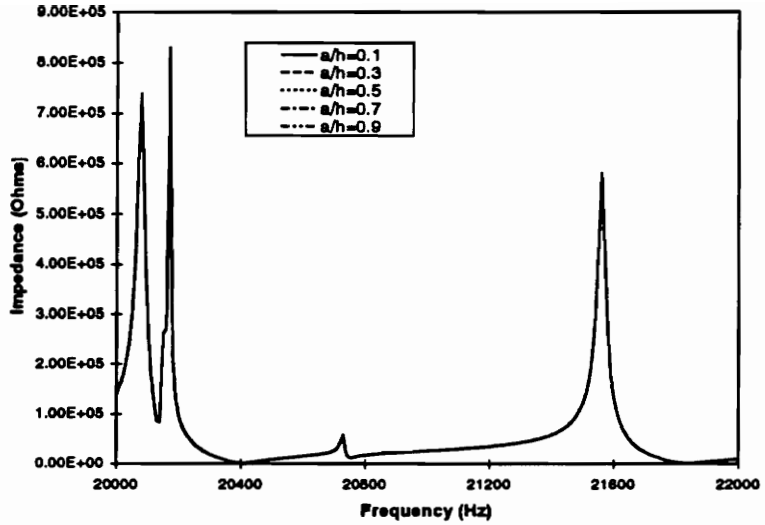

Figure 7.24. Impedance for the structure in Figure 7.20a for different crack sizes. The crack is not detected by the PZT.

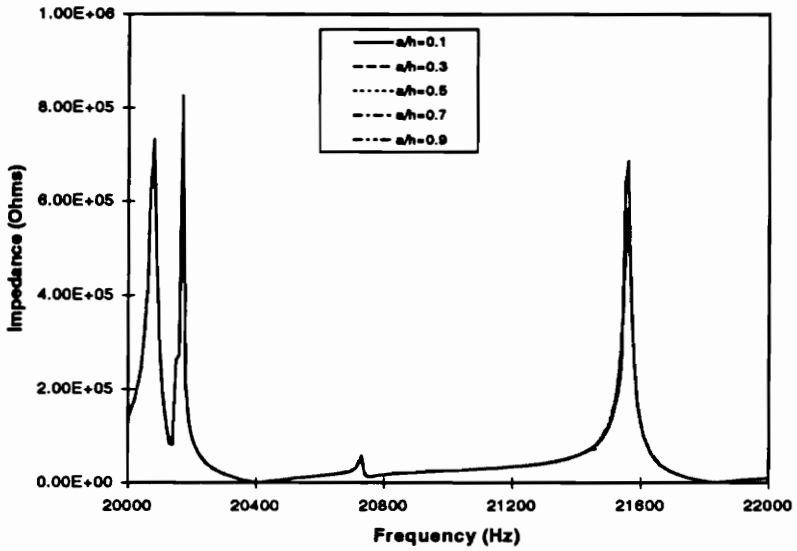

Figure 7.25. Impedance for the structure in Figure 7.20b for different crack sizes. Small impedance variation when the crack size is drastically increased.

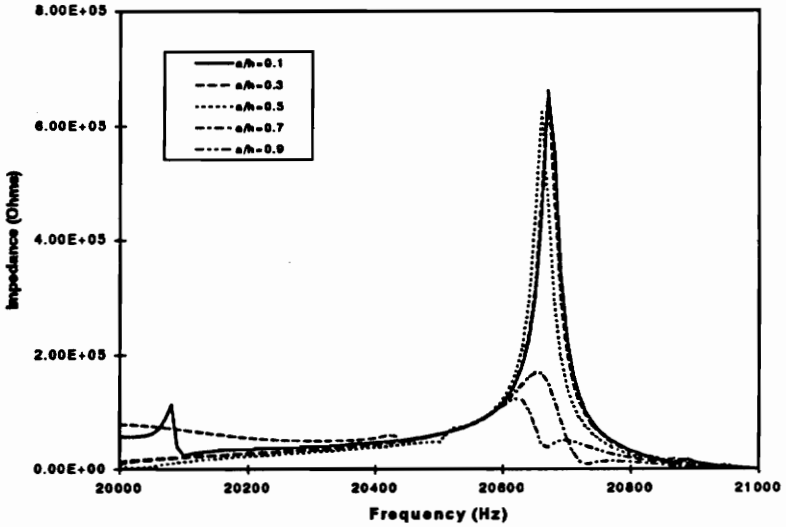

Figure 7.26. Impedance for the structure in Figure 7.20c for different crack sizes. The crack is identified by the PZT.

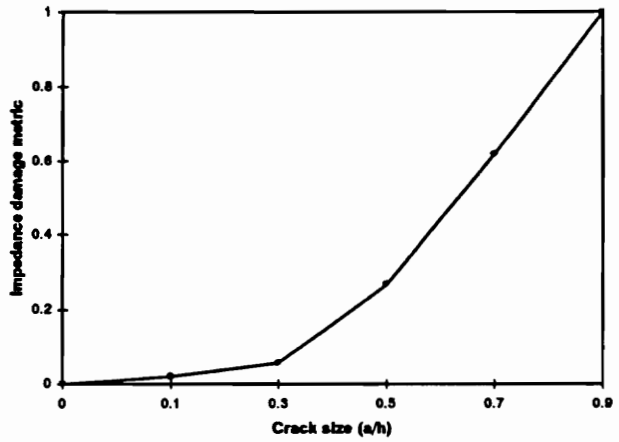

Figure 7.27. Impedance damage metric for different crack sizes. A crack-depth ratio of 0.9 was considered maximum damage.

7.3 *Experimental results*

To verify the validity of the analytical calculations presented in previous sections, a set of simple experiments have been performed on some of the most important factors discussed in this parametric study. Therefore, impedance measurements on the effect of end-mass loading will be presented. Followed by impedance and gain measurements of a two-members junction and three-members junction to corroborate the effect of member

orientation on the propagation of the induced wave. Gain measurements of multi-bolted beams has also been performed to observe the attenuation of the wave at bolted connections.

The effect of an end-mass loading on the amplitude of the impedance, to corroborate the findings presented in Figure 7.6, will be presented with the aid of a simple experiment: A 0.8x4x56 cm clamped beam is excited 8 cm from its fix end with a 0.19x20x25 mm. PSI-5A-S2 PZT actuator-sensor. The impedance is first recorded when no load is present, then by adding a load mass of 1, 2, and 5 lb., respectively, new measurements are acquired. The results are shown in Figure 7.28; as it was concluded in section 7.2.4, the addition of mass shifts the impedance measurements down, thus localizing the propagating wave. This fact should be taken into account when observing up-down shifts in recorded measurements while monitoring a structure in which there is mass loading present.

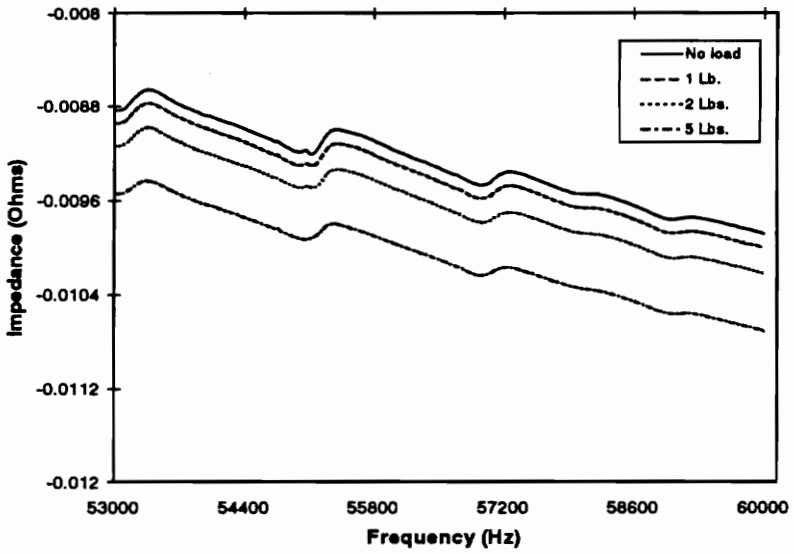

Figure 7.28. Effect of end-mass loading on the impedance. Experimental results.

A free-free two-members junction configuration is first investigated, impedance measurements are recorded for different angle orientations of beam 2 as shown in Figure

7.29. Beam 1 is 60 cm long, while beam 2 is 26.75 cm long, both having a 22.2x3.1 mm cross section. Beam 2 is overlapped and bolted to beam 1 with a bolt 6.1 mm diameter, tighten with a nut and a spring washer to provide the necessary tension, all having a mass of 9.83 gr. (the diameter, weight, and full tightness torque of the various bolts used in these experiments are given in table 7.3). A T107-A45-501 PZT actuator-sensor of dimensions 22.8x22.2x0.19 mm is bonded to the free end of beam 1 and wired to a multipurpose HP4194A gain/impedance analyzer to record the impedance at a given frequency range (the experimental set-up is extensively underlined in section 4.2). Different frequency bands were chosen to corroborate the pattern of results shown in Figure 7.29, the larger amplitude of the impedance is observed when beam element 2 makes a 180° angle with beam 1, while the amplitude is smallest when beam 2 makes a 90° angle with beam 1. Showing that at theta 180° the junction is at the most optimal position for the transmission of the incident wave. These results are reinforced with measurements of the gain at beam 2 (4 cm. from the joint) for different angle orientation. The results are shown in Figure 7.30, the 180° angle position gives the largest amplitude of the response on beam 2, and it decreases sharply as the angle becomes acute with respect to the incoming PZT's induced wave. These results corroborate the analytical findings described in section 7.2.6.1.

Table 7.3 Dimensions and torque of the bolts used in these experiments.

BOLT	Diameter (mm.)	Weight (gr.)	Max. torque (Nm)
Small	6.1	9.83	21
Medium	7.68	17.13	25
Large	9.17	26.25	29

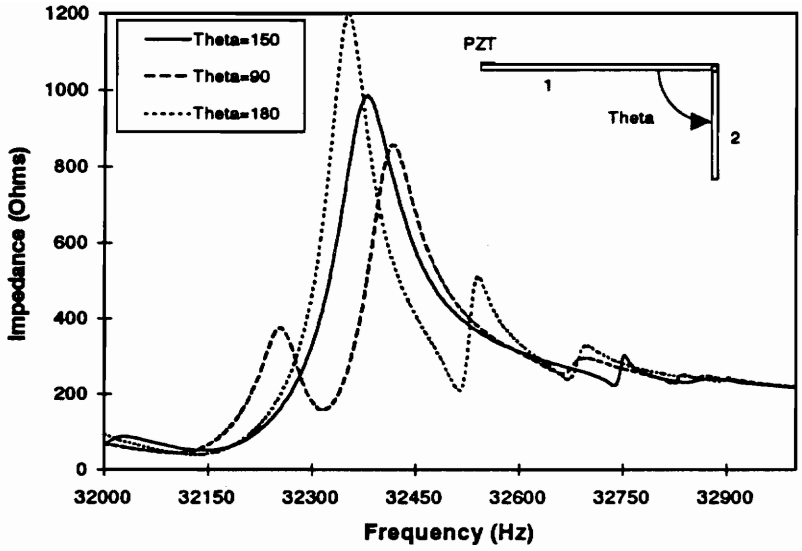

Figure 7.29. Impedance measurements of different angle orientation of a two-member junction. Experimental results.

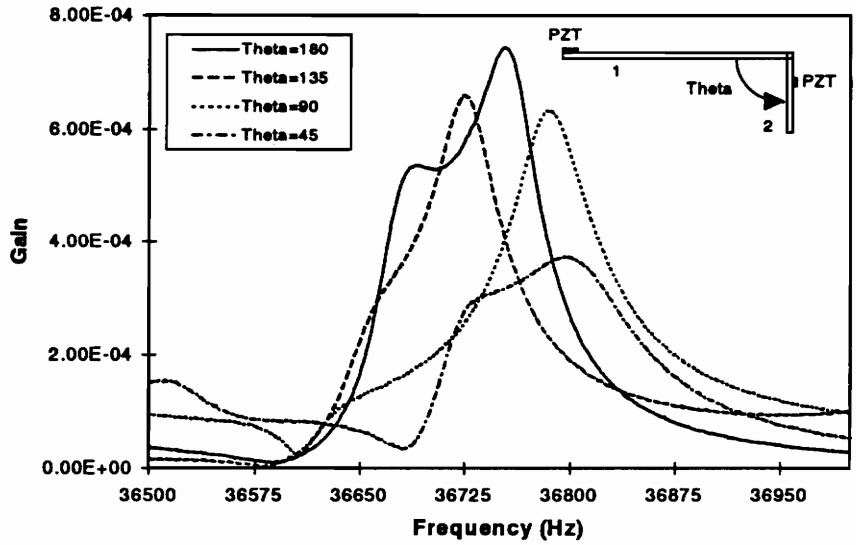

Figure 7.30. Gain measurements at beam 2 for different angle orientation of a two-member junction. Experimental results.

The effect that angle orientation has on the impedance could be utilized as a barometer to detect incipient damage due to bend in members, that could lead to failure of the member. Therefore, a damage metric could be constructed from impedance

measurements of a beam bent at different angles. The metric is taken from the difference squared of the impedance recorded when the bar is straight, and that when the bar is bent at a certain angle. A 20° angle bent is considered to be the maximum angle to which a beam member could be bent before failure occurred. The experimental data was taken at different frequency ranges, and no frequency dependence was noticed. Figure 7.31 shows the curve representing the impedance damage metric due to bend in a member.

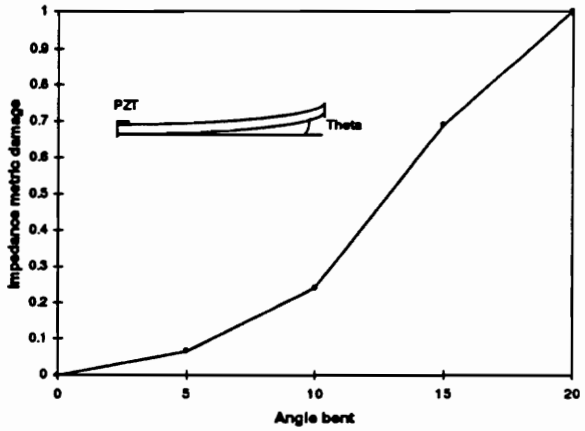

Figure 7.31 Impedance damage metric due to bend in a member. Experimental results.

A three-members junction was also analyzed with the use of a free-free T-beam configuration as shown in Figure 7.32. Beam elements 1 and 2 each has a length of 30 cm, while beam 3 is 26.75 cm long. Beam 3 is overlapped and bolted to beams 1 and 2 with the small bolt (see table 7.3). The PZT actuator-sensor has the same dimensions and material properties as the one used for the two-members configuration. Beams 1 and 2 remain at 0°, while beam 3 varies orientation. Figure 7.32 shows the effect of angle orientation on the impedance at a resonance; the largest effect of orientation is observed when beam 3 is at 90°, thus recording the largest amplitude of the impedance. This behavior was repeatedly observed for various frequency ranges. To visualize the transmission of the propagating wave affected by the angle orientation of beam 3, Figure 7.33 shows the gain measured at beam 3 for two angles; as it was predicted in section 7.2.6.2, the 90° angle orientation gives the optimal position of beam 3 for the transmission of the propagating wave. For the purpose of completeness, another three-member junction

structure was also investigated. This time, a thick Al 6061-T6511 beam of cross-section 50.74x25.58 mm and 50 cm long is bolted through its thickness at the middle to a transverse beam having the same cross sectional dimensions and 30 cm long. There are two transverse beams; one making a 90° angle and another making a 135° angle. A 38.18x50.74x0.19 mm T107-A45-501 PZT actuator-sensor is used to excite the structure. The impedance recorded is shown in Figure 7.34; due to the thickness of the beam, small interaction is observed, but nevertheless, it is proven that there is a larger effect on the impedance measurement for a 90° angle orientation of a three-members junction configuration than at any other angle orientation, 45° in this case, as it was also shown in Figure 7.32.

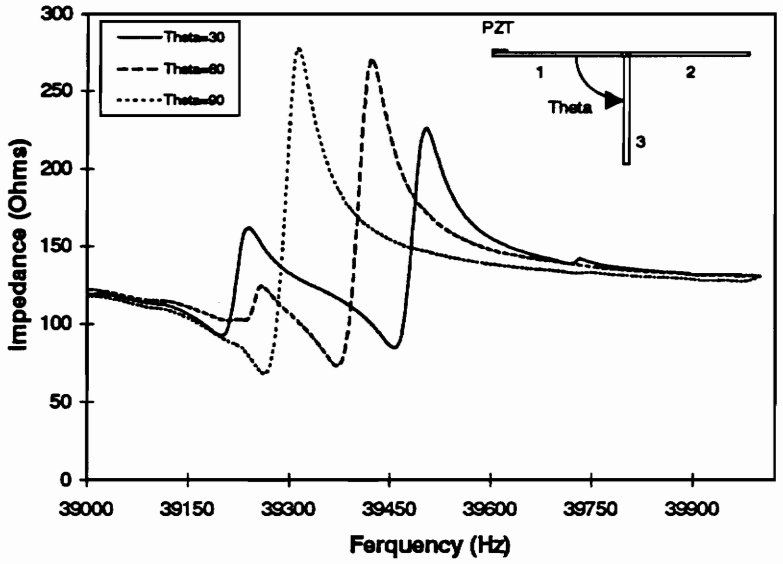

Figure 7.32. Impedance measurements of different angle orientation of a three-member junction. Experimental results.

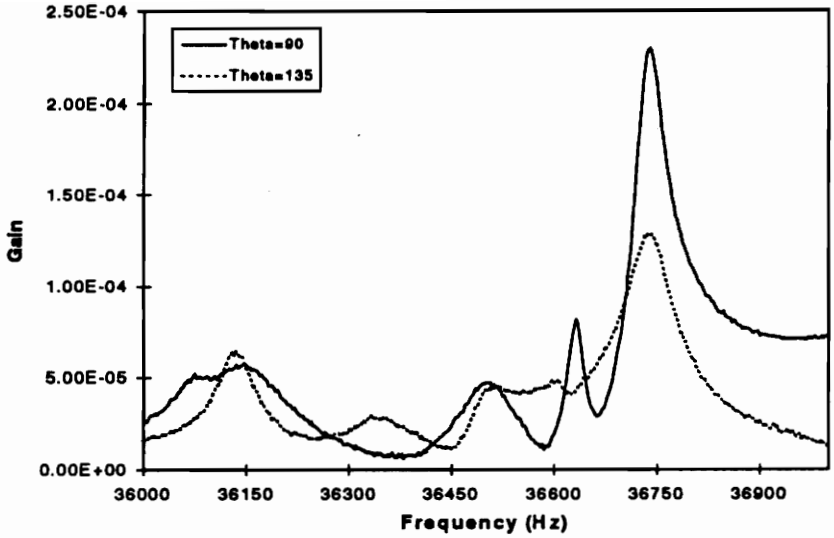

Figure 7.33. Gain measurements at beam 3 for different angle orientation of a three-member junction. Experimental results.

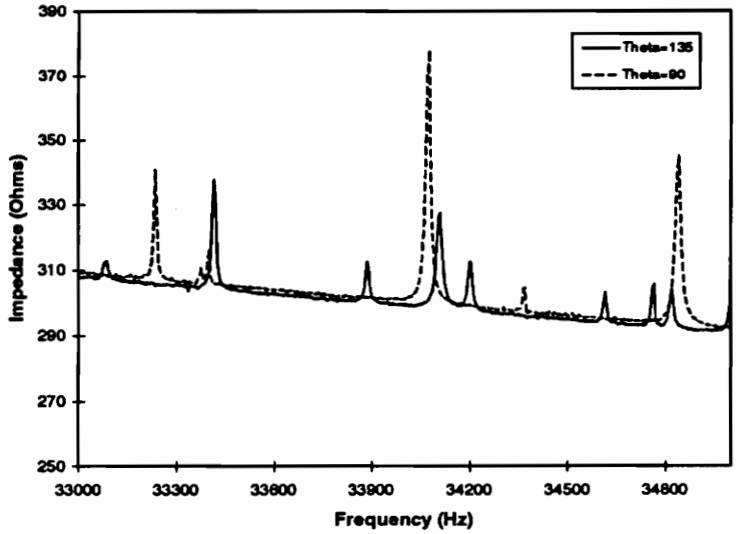

Figure 7.34. Impedance measurements of different angle orientation of a three-member junction using a thick cross-section beam, bolted through its thickness. Experimental results.

To investigate the attenuation of the propagating wave due to the effect of bolt size, the three-member structure with members having a 22.2x3.1 mm cross-section, previously described, is used with different size of bolts. The results are shown in Figure

7.35, the dimensions and tightness of the various bolts are given in table 7.3. The free-free T-beam bolted structure is excited with a PZT-actuator at the free end, and the response is recorded at a PZT-sensor, which is located 4 cm from the joint. As it was demonstrated in Figure 7.15, the induced wave is more largely attenuated with the presence of a larger bolt, as it can be deduced from the smallest response recorded at the sensor location, across the joint.

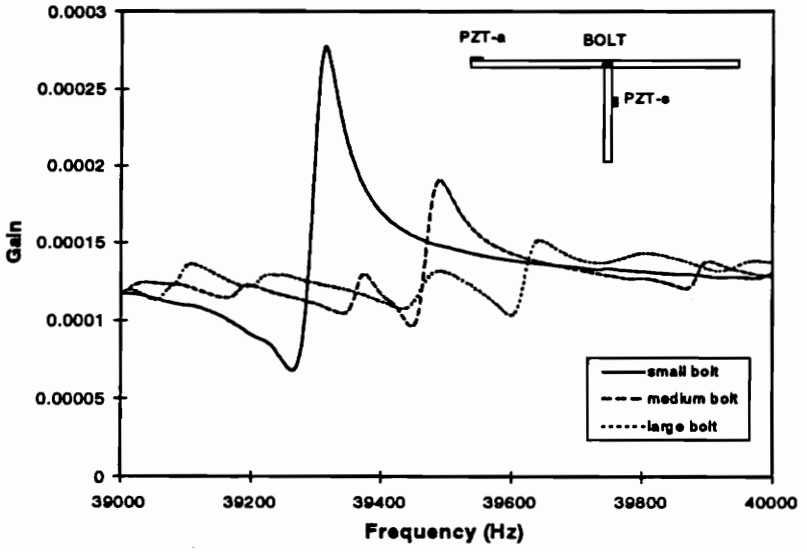

Figure 7.35. Gain measurements, at beam 3, for a 90° angle orientation of a three-member junction to observe the wave attenuation due to bolt size. Experimental results.

The energy attenuation due to bolted connections is further investigated with the use of this three-members configuration, by bolting an additional 26.75 cm long beam to the free end of beam 2, as shown in Figure 7.36. The gain of the structure is again measured by the PZT-sensor bonded at bar 3 a distance 4 cm from the bolted connection, and also by the PZT-sensor at bar 4, 4 cm from the joint. The results shown in Figure 7.36 are consistent with the findings presented in this parametric study; there is a large localization of the propagating wave after the first bolted connection. To observe the attenuation of the wave after two bolted connections, three Al 6061- T6511 beams, 26.5 cm long, are bolted together with two large bolts (refer to Table 7.3) as shown in Figure 7.37. The gain of this arrangement is measured before the first bolt, at sensor 1, after the

first bolt, at sensor 2, and after the second bolt, at sensor 3. Again the energy dissipated after the first bolt, clearly attenuates the incident wave at the joint, but after the second bolted connection the transmitted wave is localized even further, and very little of the vibration energy is transmitted across the second bolted discontinuity.

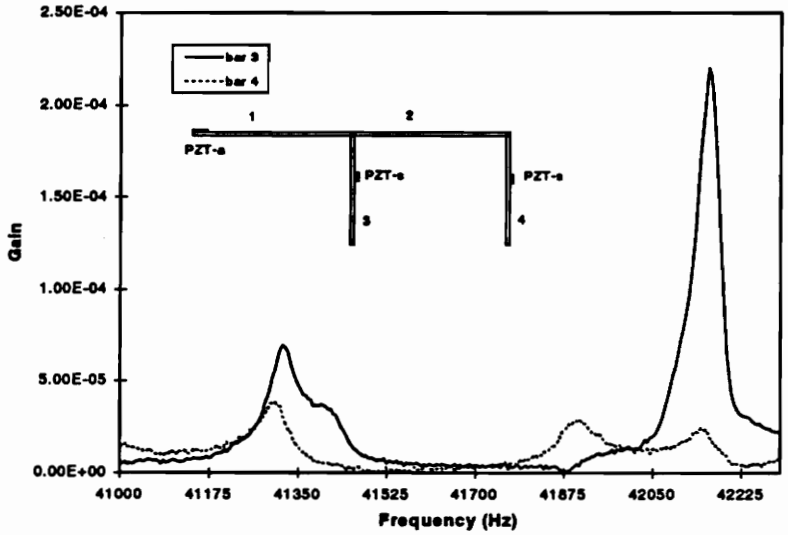

Figure 7.36. Gain measurements on multi-bolted structures to observe the effect of bolts on the attenuation of the propagating wave. Experimental results.

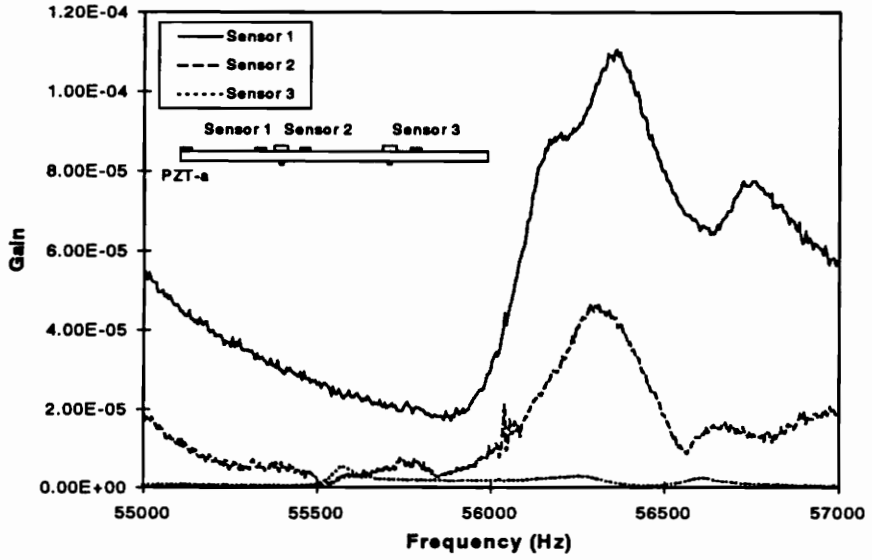

Figure 7.37. The attenuation of the propagating wave is greatly localized after two bolted connections. Experimental results.

The results shown with the use of these simple experiments, aid in the understanding of the effects that some of the various factors, addressed in this parametric study, have on the localization of the PZT's driven propagating wave, and in the successful corroboration of the analytical findings.

7.4 *Conclusions*

The motivation of this parametric study is to have a better understanding on "how to go about" when attaching PZT patches to a structure for health monitoring with the use of the impedance-based NDE technique and to have a better insight on the level of incipient damage that an inspected member can sustained before more catastrophic failure can occurred. Various real life scenarios have been reproduced and investigated to have a feeling of the PZT's induced wave interaction at critical areas to account for in a structure. Thereby, a thoroughly analysis of certain factors has been presented and grouped as attenuating mechanisms, such as the effect of end-mass and concentrated mass, discontinuity of cross-section, material discontinuity and multi-member junctions considering several orientations, and dissipative mechanisms, such as internal damping and bolted connections.

The results of this parametric study will be here summarized. It was found that impedance would shift to the right and would have an increase in amplitude for stiffer materials, while most damped materials would tend to give more shallow signals. These factors should be taken into account when attaching PZTs close to areas of different materials. For this reason, further investigation of material effect on the propagating wave was done with the use of material discontinuity in structures; it was observed that for intermaterials softer than the PZT's host transmitted material, the area of material discontinuity acts as an energy absorbent, bringing the amplitude of the response down. The opposite effect is observed when a harder material is encrusted into the sandwiched region. Also, the sensing range of the PZT will be affected by the internal damping of the

monitored structure's material, therefore the number of PZTs needed to inspect the system would vary accordingly. An interesting conclusion was drawn from the analysis of cross-sectional discontinuities; it was found that such discontinuities are a source of reflections and that even for relatively small cross-sectional differences, the wave transmitted across the discontinuity is attenuated. To show this effect, an attenuation metric was introduced in order to visualize the transmission of the PZT's induced wave at stepped beams. Another blocking effect of the propagating wave was observed when attaching a concentrated mass in the structure: First, an analysis of end-mass loading showed that addition of mass has a down shifting effect of the impedance. Then, a concentrated mass was attached in order to block the propagation of the induced wave; a large attenuation, due to multiple reflections at the point of attachment, was observed. The loading effect on a structure is treated as a source of incipient damage, and therefore an impedance damage metric curve was plotted to indicate when failure may occurred.

An extensive analysis of multi-members junctions followed: It was observed that junctions of two members at right angles and for orientations making an acute angle with the incoming disturbance tend to transmit more poorly the PZT's induced wave. While for 180° orientations, the wave was most optimally transmitted. Other interesting conclusions were drawn when attaching three members into a junction. A more realistic scenario was reproduced by introducing nonconservative bolted joints: A nonlinear approximation of the dynamics of such joints was implemented to reproduced the wave interaction with dissipative mechanisms in the structure, other than the inherited material damping. At a first glance, it was observed that the size of the bolt plays a great role in the attenuation of the propagating wave, while the bolt material was less crucial. On the other hand, surface finishing and clamping force at the matting section are the most important factors to consider when evaluating the energy dissipated at the bolted joint, but due to the invariability of the coefficient of friction, both factors are given in terms of the shearing force at the interface. Triangular and square bolted configurations were treated to observe the attenuation in close bolted structures. It was observed that, besides the wave reflections suffered at the angled junctions, great energy losses are sustained at the bolted

connections. Moreover, the sensing range of the PZT's induced wave is greatly localized after one bolted joint, regardless of its size. These findings were corroborated with a multi-member bolted structure, in which a crack was simulated to observe the impedance for various bolted arrangements. It was concluded that the sensing region of the induced wave was mostly concentrated before the first strong bolted connection, and that no changes in impedance were observed after a second strong bolted connection. The effect of using a weaker bolt at the joint sensibly ameliorates these results, but still the energy concentration is largely localized before the first bolted junction. The weakening of bolted joints is a source of incipient damage. For this reason, a damage metric for different size of bolts at different reduce tightness have been reconstructed. With this metric, inspection of a bolted section can be made with knowledge about the tightness of the monitored bolt. A decrease in impedance was observed for increasing crack size. Also, an impedance damage metric was elaborated based on the size of the crack.

A set of simple experiments were performed and presented to corroborate the analytical results obtained in this parametric study. An impedance damage metric based on the angle orientation due to bend of a member was also experimentally reconstructed. To summarize the findings presented in this parametric study, Table 7.4 gives a brief description of the most important effects that the different factors considered in this study have on the sensing region of a PZT, and a rating of the factor's importance; 0 corresponds to a factor of no importance, while 5 would be the most important factor. With the guidelines here presented, a more precise manner to go about when attaching PZT patches to structures for health monitoring implementation is made possible. Due to the qualitative information obtained about incipient damage with the use of the impedance based NDE technique, this study only pretends to give a feeling about the wave interaction with the monitored structure, other than real quantification of the energy dissipation and exact sensing range. Moreover, exact calculations become an impossible task due to the high frequency range of operation of this NDE technique (30-150 kHz), and very little additional information would be gain. Also, wave attenuation due to damping in the

structure coming from energy dissipative mechanisms, are highly frequency dependent, and thereby the difficulty to track the impedance signal behavior.

Table 7.4. Factors to consider when attaching PZT actuator-sensors to structures for health monitoring. Rating 0 to 5 in order of least important to most important.

Factors	Important effects	Rating
Material stiffness and density	Impedance shifts to the right and up for stiffer materials.	1
Energy absorbent intermaterials	Decrease in amplitude for softer intermaterials. Significantly larger for highly damped materials.	2
Material damping	More damped materials give shallower peaks, greater localization of the induced wave.	3
Mass loading	Blocking effect on the wave; significant for large mass size. End-mass shifts impedance down.	3
Discontinuity in cross-section	Source of reflections: important attenuation at large cross-section discontinuities.	3
Two-member junction	Decrease in impedance with increase in angle away from flat position.	3
Bolted joints	Size of the bolt more important than its material. Shearing force at the interface is the most important factor. Major source of energy losses.	5

Chapter 8

Conclusions and Recommendations

8.1 Conclusions

In this dissertation, a continuum mechanics based wave propagation model has been applied to investigate the interaction of a PZT's induced wave with the structure to which it is bonded for health monitoring purposes. It has been presented that the sensing region of the PZT actuator-sensor patch is limited to the close vicinity of the source. This phenomena has been related to the high frequency content of the low-power supply PZT's excitation, and the presence in the monitored structure of energy dissipation mechanisms, such as structural joints and material damping, and attenuation mechanisms acting as sources of multiple reflections. Therefore, an extensive analytical effort has been first carried out to model energy dissipation mechanisms and to include their describing parameters into the formulation, together with the electromechanical coupling of the PZT-structure interaction. Once these models has been corroborated a parametric study, including these energy dissipation mechanisms and other structural discontinuities acting as reflection boundaries, has been presented to acquire a better knowledge of the various factors needed to be considered when attaching PZT actuator-sensors to structures for monitoring purposes.

The principal conclusions of this dissertation are:

- A methodology to model one-dimensional bolted structures' high frequency vibration has been developed. The bolted junctions were modeled using a set of linear mass-spring-dash pots systems and also using a more unique nonlinear system, which consisted of Coulomb friction and clearance fit elements.

- Since measurements of the structural properties are given in terms of the mechanical response of the structure, there is a need to make this information compatible with the electrical readings acquired by the PZT. A previously derived impedance based model has been borrowed to describe the electromechanical interaction of the PZT-structure and obtain meaningful results.
- It was experimentally proven that torsional modes are too sensitive to be relied on for health monitoring at high frequency.
- It has been shown that the wave interaction at a dissipative bolted discontinuity is highly frequency dependent, and thus it depends on the deflection of a particular mode. Nevertheless, qualitative assessments on the energy losses occurring at bolted connections were carried out to show that there is a decrease in reflection and transmission with an increase in dissipation when the wave acted upon a joint at a resonant frequency.
- An analysis showing the effect of loosening a bolted connection was also carried out. For the linear joint model this effect was simulated by reducing the spring stiffness and increasing the damping at the dash pots, while for the nonlinear case this was reproduced by reducing the tangential shearing force and the Coulomb stiffness.
- A method to obtain the average energy losses of a structure in terms of its specific damping capacity, has been also successfully applied: Once an implicit function, describing the dynamics of the system, has been derived, an analytical procedure is carried out, coupled with experimental measurements of the viscoelastic properties of the material, to calculate the specific damping capacity of the structure, as a quantification of its energy losses, at a given resonant frequency.
- It has been shown that the energy dissipated due to structural joints is much more significant than that due to internal friction.

Important conclusions could be drawn from the parametric study:

- It was found that impedance measurements would shift to the right and would have an increase in amplitude for stiffer materials, while most damped materials would tend to give more shallow signals.
- It was observed that for intermaterials softer than the transmitted material, the sandwiched area acts as an energy absorbent, bringing the amplitude of the response down, while the opposite effect is observed when a harder material is encrusted into the sandwiched region.
- From the analysis of cross-sectional discontinuities; it was found that such discontinuities are a major source of reflections and that even for relatively small cross-sectional differences, the wave transmitted across the discontinuity is attenuated.
- An analysis of end-mass loading showed that addition of mass has a down shifting effect of the impedance measurements, localizing the propagating wave. Then, a concentrated mass was attached in order to block the propagation of the induced wave; a large attenuation, due to reflections at the point of attachment, was observed.
- It was observed that junctions of two members at right angles and for orientations making an acute angle with the incoming disturbance tend to transmit more poorly the PZT's induced wave. On the other hand, for 0° angle orientation the wave was most optimally transmitted.
- Analysis of three-member junctions showed that there is a larger wave interaction when two of the members were fixed at 90°. Moreover, optimum transmission was achieved when the third member was at 0° with one of the members, while the other two remained at 90°.
- A more realistic scenario was reproduced by introducing nonconservative bolted joints. It was observed that the size of the bolt plays a great role in the attenuation of the propagating wave, while the bolt material was less crucial. On the other hand, surface finishing and clamping force at the matting section are the most important parameters to consider when evaluating the energy dissipated at the bolted joint. Due to the uncertainty of the coefficient of friction when a bolted structure is under cyclic

loading, it was concluded that knowledge about the shearing force at the interface should be considered to account for the two parameters.

- Triangular and square bolted configurations were treated to observe the attenuation in close-bolted structures. It was observed that, besides the wave reflections suffered at the angled junctions, great energy losses are sustained at the bolted connections. Moreover, the sensing range of the PZT's induced wave is greatly localized after one bolted joint, regardless of its size, reducing the amplitude of the transmitted wave by roughly one order of magnitude and even further for the second bolted joint.
- These findings were corroborated with a multi-member bolted structure, in which a crack was simulated to observe impedance measurements for various bolted arrangements. It was concluded that the sensing region of the induced wave was mostly concentrated before the first strong bolted connection, and that no changes in impedance measurements are observe after a second strong bolted connection. There was also observed a large attenuation of the propagating disturbance due to an increase in the crack size.
- Plots of the response as a function of distance for various beam specimens have been reconstructed to have a better knowledge on the number of PZTs needed to monitor structural members with no discontinuities.
- The effect of loading on monitored structures has been addressed with the aid of an impedance damage metric. The metric curve has been reproduced analytically to aid in the detection of this sort of incipient damage before it leads to more catastrophic failure.
- An attenuation metric has been introduced to observe the degree of transmission at cross-sectional discontinuities.
- The weakening of bolts is a significant source of incipient type damage. Therefore, an impedance damage metric was analytically reconstructed for three different size of bolts and tightness reduction.

- Another source of incipient damage can arise from the bent of a member, and a damage metric curve to account for this factor was experimentally reconstructed. When the member has exceeded a safety level of damage, the member is replace.
- An impedance damage metric was reconstructed based on the effect that crack size has on the impedance.
- These parametrics were corroborated with simple experiments based in some of the most important factors considered in this study.

8.2 Recommendations

With the guidelines here presented, a more precise manner to go about when attaching PZT patches to structures for health monitoring implementation is made possible. Due to the qualitative information obtained about incipient damage with the use of the impedance based NDE technique, this research only pretend to give a feeling about the wave interaction with the monitored structure, other than real quantification of the energy dissipation and exact sensing range. Moreover, exact measurements and energy losses quantification become an impossible task due to the high frequency range of operation of this NDE technique (30-150 kHz), and very little additional information would be gained. Also, wave attenuation due to damping in the structure coming from energy dissipation mechanisms, are highly frequency dependent, and thereby the difficulty to track the exact impedance signal behavior. A two-dimensional analysis could be carried out to observe the wave propagation in plates and shells, but the additional information about the PZT's wave interaction with the structure would not be sufficient to justify the analytical effort.

Bibliography

1. Sun, F. P., Chaudhry, Z., Liang, C. and Rogers, C. A., "Truss Structure Integrity Identification Using PZT Sensor-Actuator", Proceedings 1994 International Conference on Intelligent Materials, June 5-8, 1994, Williamsburg, VA. pp. 1210-1222.
2. Lalande, F., and Rogers C. A., "Solid-State Active Sensing for In-situ Health Monitoring," Society for Machinery Failure Prevention Technology Showcase, Mobile, AL, April 22-26, 1996; in press
3. Chaudhry, Z., Joseph, T., Sun, F., and Rogers, C. A., "Local Area Health Monitoring of Aircraft via Piezoelectric Actuator/Sensor Patches," Paper No. 2443-29, SPIE 1995 North American Conference on Smart Structures and Materials, San Diego, CA, 26 Feb.-3 Mar., 1995, pp. 268-276.
4. Cawley and R. D. Adams, "The location of Defects in Structures from Measurements of Natural Frequencies," Journal of Strain Analysis, Vol. 14, no. 2, 1979, pp. 49-57.
5. Adams, D. Walton, J. Flitcroft and D. Short, "Vibration Testing as a Non-Destructive Test Tool for Composite Materials," Composite Reliability, ASTM STP 580, 1975, pp. 159-175.
6. Adams, P. Cawley, C. Pye and B. Stone, "A Vibrational Technique for Nondestructively Assessing the Integrity of Structures", Journal of Mechanical Engineering Science, Vol. 20, 1978, pp. 93-100.
7. Agbadian, S. Masri, R. Miller and T. Caughey, "System Identification Approach to Detection of Structural Changes", Journal of Engineering Mechanics, Vol. 117, no. 2, 1991, pp. 370-390.
8. Baruh and S. Ratan, "Damage Detection in Flexible Structures", Journal of Sound and Vibration, Vol. 166, 1993, pp. 21-30.

9. Peterson, K. Alvin, S. Doebling and K. Park, "Damage Detection Using Experimentally Measured Mass and Stiffness Matrices", AIAA Journal, V. 1482, 1993, pp. 1518-1528.
10. Silva and A. Gomes, "Experimental Dynamic Analysis of Crack Free-Free Beams," Experimental Mechanics, Vol. 30, 1990, pp. 20-25.
11. Nokes and G. Cloud, "The Application of Interferometer Techniques to the Nondestructive Inspection of Fiber-Reinforced Materials", Experimental Mechanics, Vol. 33, 1993, pp. 314-319.
12. Martin and J. Doyle, "Crack Detection in Framed Structures", Proceedings 1994 SEM Conference, June 6-8 1994, Baltimore, MD.
13. Banks, D. Inman and Y. Wang, "An Experimentally Validated Damage Detection Theory in Smart Structures", Journal of Sound and Vibrations, Vol. 191, No. 5, 1996, pp. 859-880.
14. MacLellan, P. T., Stubbs, D. A. and Karpur, P., "Monitoring Fatigue Damage in Metal Matrix Composites, in Situ, Using Ultrasonic Surface Waves", Proceedings 1994 SEM Spring Conference, June 6-8, 1994, Baltimore, MD.
15. Ho, C. L., "Ultrasonic Surface Wave Detection Technique", Chap. 3, Experimental Techniques in Fracture Mechanics, 2, 1975, ed. A. S. Kobayashi, Iowa State Press.
16. Maginnes, M. G., "The Reconstruction of Elastic Wave Fields from Measurements over a Transducer Array", Journal of Sound and Vibration, Vol. 20, no. 2, 1972, pp. 219-240.
17. Doyle, J. F., "A Generic Algorithm for Determining the Location of Structural Impacts", Experimental Mechanics, Vol. 33, 1993, pp. 37-44.
18. Beards, C. F. and Williams, "The Damping of Structural Vibration by Rotational Slip in Joints", Journal of Sound and Vibration, Vol. 53, No. 3, 1977, pp. 333-340.
19. Beards, C. F., "The Damping of Structural Vibration by Controlled Interfacial Slip in Joints", Journal of Vibration, Acoustics, Stress and Reliability in Design, Vol. 105, 1983, pp. 369-373.

20. Earles, S. W., "Theoretical Estimation of the Frictional Energy Dissipation in a Simple Lap Joint", Journal of Mechanical Engineering Science, Vol. 8, 1966, pp. 207-214.
21. Masuko, M., Ito, Y. and Yoshida, K., "Theoretical Analysis for a Damping Ratio of a Jointed Canti-Beam", Bulletin of the JSME, Vol. 16, No. 99, 1973, pp. 1421-1432.
22. Richardson, R. S. and Nolle, H., "Energy Dissipation in Rotary Structural Joints", Journal of Sound and Vibration, Vol. 54, no. 4, 1977, pp. 577-588.
23. Metherel, A. F. and Diller, S. V., "Instantaneous Energy Dissipation Rate of Lap-Joint Uniform Clamping Pressure", Journal of Applied Mechanics, Vol. 35, 1968, pp. 123-128.
24. Den Hartog, J. P., Mechanical Vibrations, McGraw-Hill, New York, 1956.
25. Ferri A. A. and Bindemann, A. C., "Damping and Vibration of Beams with Various Types of Frictional Support", Journal of Vibrations and Acoustics, Vol. 114, 1992, pp. 289-296.
26. Crandall, S. H., "Nonlinearities in Structural Dynamics", The Shock and Vibration Digest, Vol. 6, No. 8, 1974, pp. 2-14.
27. Pratt, T. K. and Williams, R., "Nonlinear Analysis of Stick-Slip Motion", Journal of Sound and Vibration, Vol. 74, No. 4, 1981, pp. 531-542.
28. Menq, C. and Griffin, J. H., "A Comparison of Transient and Steady State Finite Element Analysis of the Response of a Frictionally Damped Beam", Journal of Vibration, Acoustics, Stress and Reliability in Design, Vol. 107, 1985, pp. 19-25.
29. Earles, S. W., "Linearized Analysis for Frictionally Damped Systems", Journal of Sound and Vibration, Vol. 24, no. 4, 1972, pp. 445-458.
30. Iwan, W. D., "A Generalization of the Concept of Equivalent Linearization", International Journal of Nonlinear Mechanics, Vol. 8, 1973, pp. 279-287.
31. Dowell, E. H., "The Behavior of a Linear, Damped Modal System with a Nonlinear Spring-Mass-Dry Friction Damper System Attach", Journal of Sound and Vibration, Vol. 89, no. 1, 1983, pp. 65-84.

32. Gaul, L., "Wave Transmission and energy Dissipation at Structural and Machine Joints", Journal of Vibration, Acoustics, Stress and Reliability in Design, Vol. 105, 1983, pp. 489-504.
33. Miller, R. K., "An Approximate Method of Analysis of the Transmission of Elastic Waves Through a Frictional Boundary", Journal of Applied Mechanics, Vol. 44, 1977, pp. 652-656.
34. Vakakis, A. F., "Scattering of Structural Waves by Nonlinear Elastic Joints", Journal of Vibration and Acoustics, Vol. 115, 1993, pp. 403-410.
35. Nayfeh, A. H., Vakakis, A. F. and Nayfeh, T. A., "A Method for Analyzing the Interaction of Nondispersive Structural Waves and Nonlinear Joints", Journal of the Acoustical Society of America, Vol. 93, no. 2, 1993, pp. 849-856.
36. Wang, J. and Sas P., "A Method for Identifying Parameters of Mechanical Joints", Journal of Applied Mechanics, Vol. 57, 1990, pp. 337-342.
37. Yoshimure, M., "Measurement of Dynamic Rigidity and Damping Property of Simplified Joint Models and Simulation by Computer", Annals of the CIRP, Vol. 25, no. 1, 1977, pp. 193-198.
38. Yoshimura, M., "Computer-Aided Design Improvement of Machine Tool Structure Incorporating Joint Dynamics Data", Annals of the CIRP, Vol. 28, no. 1, 1980, pp. 241-246.
39. Plunkett, R., "Damping Analysis: An Historical Perspective," M3D: Mechanics and Mechanisms of Material Damping, ASTM, 1992, pp. 562-569.
40. Kolsky, H., "Stress Waves in Solids," Dover Publications, New York, 1963.
41. Goodman, L. E., "A Review of Progress in Analysis of Interfacial Slip Damping," ASME Colloquium on Structural Damping, Atlantic City, 1959, pp. 35-48.
42. Biot, M. A., "Theory of Stress-Strain Relations in Anisotropic Viscoelasticity and Relaxation Phenomena," Journal of Applied Physica, Vol. 25, No. 11, 1954, pp. 1385-1391.
43. Hunter, S. C., "Viscoelastic Waves," Progress in Solid Mechanics, Vol. 1, 1961.

44. Morrison, J. A., "Wave Propagation in Rods of Voight Material and Viscoelastic Materials with 3-Parameter Models," Quarterly of Applied Math., Vol. 14, 1956, pp. 153-169.

45. Arenz, R. J., "Uniaxial Wave Propagation in Realistic Viscoelastic Materials," Journal of Applied Mechanics, 1964, pp. 17-21.

46. Arenz, R. J., "Two-Dimensional Wave Propagation in Realistic Viscoelastic Materials," Journal of Applied Mechanics, 1965, pp. 303-314.

47. Valalis, K. C., "Exact and Variational Solutions to a General Viscoelasto-Kinetic Problem," Journal of Applied Mechanics, 1966, pp. 888-892.

48. Bert, C. W., "Material Damping: An Introductory Review of Mathematical Models, Measures, and Experimental Techniques," Journal of Sound and Vibration, Vol. 29, 1973, pp. 129-153.

49. Lazan, B. J., "Damping on Materials and Members in Structural Mechanics," Pergamon Press, Great Britain, 1968.

50. Hillier, K. W., "The Measurement of Dynamic Elastic Properties," Progress in Solids Mechanics, Vol. 2, 1961, pp. 199-243.

51. Bishop, J. E. and Kinra, V. K., "Some Improvements in the Flexural Damping Measurement Technique," M3D Mechanics and Mechanisms of Material Damping, ASTM, Philadelphia, 1992, pp. 457-470.

52. Kimball, A. L. and Lowell, D. E., "Internal Friction in solids," Physical Review Series, Vol. 2, 1927, pp. 948-959.

53. Santini, P., Casteilani, A., and Nappi, A., "An Introduction to the Problem of Dynamic Structural Damping," AGARD Report No. 663, Sept. 1977.

54. Gaul, L., Bohlen, S., and Kempfle, S., "Transient and Forced Oscillation of Systems with Constant Hysteretic Damping," Mechanics Research Communications, Vol. 12, No. 4, 1985, pp. 187-201.

55. Tseitlin, A. I. and Kusainov, A. A., "Role of Internal Friction in Dynamic Analysis of Structures," Rotterdam, 1990.

56. Banks, H. T. and Inman, D. J., "On Damping Mechanisms in Beams," Journal of Applied Mechanics, Vol. 58, 1991, pp. 716-723.

57. Banks, H. T., Wang, Y., Inman, D. J. and Cudney, H. H., "Parameter Identification Techniques for the Estimation of Damping in Flexible Structure Experiments," Proc. of the 26th IEEE Conf. on Decision and Control, Vol. 2, 1987, pp. 1392-1395.

58. Banks, H. T., Wang, Y., Inman, D. J. and Cudney, H. H., "Spatial vs. Time Hysteresis in Damping Mechanisms," Proc. of the 27th IEEE Conf. on Decision and Control, Vol. 2, 1988, pp. 1674-1677.

59. Nakao, T., Okano, T. and Asano, I., "Theoretical and Experimental Analysis of Flexural Vibration of the Viscoelastic Timoshenko Beam," Journal of Applied Mechanics, Vol. 52, 1985, pp. 728-731.

60. Lisieutre, G. A. and Mingori, P. L., "Finite Element Modeling of Frequency Dependent Material Damping Using Augmenting Thermodynamic Fields," Journal of Guidance, Vol. 13, No. 6, 1990, pp. 1040-1050.

61. Lesieutre G. A., "Finite Element for Modeling Frequency Dependent Material Damping Using Internal State Variables," M3D Mechanics and Mechanisms of Material Damping, ASTM, Philadelphia, 1992, pp. 344-357.

62. Golla, D. F. and Hughes, P. C., "Dynamics of Viscoelastic Structures-A Time Domain, Finite Element Formulation," Journal of Applied Mechanics, Vol. 52, 1985, pp. 897-906.

63. Padovan, J., "Computational Algorithms for Finite Element Formulations Involving Fractional Operators," Computational Mechanics, Vol. 2, 1987, pp. 271-287.

64. Bagly, R. L. and Torvik, P. J., "Fractional Calculus-A different Approach to the Analysis of Viscoelastically Damped Structures," AIAA Journal, Vol. 21, No. 5, 1983, pp. 741-748.

65. Sorokin, E. S., "On the Theory of Internal Friction in Vibrations of Elastic Systems," Moscow, 1960.

66. Reznikov, L. M., "Accounting for Internal Non-Elastic Resistance While Investigating Random Vibration of Structures," SMiRS, No. 4, 1974, pp. 48-53.

67. Gaul, L., Klein, P. and Plenge, M., "Continuum Boundary Element and Experimental Model of Soil Foundation Interaction," Proc. 6th Int. Conf. in Numerical Methods in Geomechanics, Innsbruck, 1985, pp. 1649-1661.

68. Brillouin, L., "Wave Propagation in Periodic Structures," New York, Dover Publications, 1953.

69. Mead, D. J., "Free Wave Propagation in Periodically Supported, Infinite Beams," Journal of Sound and Vibration, Vol. 11, No. 2, 1970, pp. 181-197.

70. Mead, D. J., "Wave Propagation and Natural Modes in Periodic Systems: I. Mono-Coupled Systems," Journal of Sound and Vibration, Vol. 40, No. 1, 1975, pp. 1-18.

71. Mead, D. J., "Wave Propagation and Natural Modes in Periodic Systems: II. Multi-Coupled Systems, with and without Damping," Journal of Sound and Vibration, Vol. 40, No. 1, 1975, pp. 19-39.

72. Mead, D. J., "A New Method of Analyzing Wave Propagation in Periodic Structures; Applications to Periodic Timoshenko Beams and Stiffened Plates," Journal of Sound Vibration, Vol. 104, No. 1, 1986, pp. 9-27.

73. Ziegler, F., "Wave Propagation in Periodic and Disordered Layered Composite Elastic Materials," International Journal of Solids Structures, Vol. 13, 1977, pp. 293-305.

74. Li, D., and Benaroya, H., "Waves, Normal Modes and Frequencies in Periodic and Near Periodic Rods. Part I," Wave Motion, Vol. 20, 1994, pp. 315-338.

75. Li, D., and Benaroya, H., "Waves, Normal Modes and Frequencies in Periodic and Near Periodic Rods. Part II," Wave Motion, Vol. 20, 1994, pp. 339-358.

76. Cai, G., and Lin, Y., "Localization of Wave Propagation in Disordered Periodic Structures," AIAA Paper 90-1216-CP, 1990.

77. Roy, A. K., and Plunkett, R., "Wave Attenuation in Periodic Structures," Journal of Sound and Vibration, Vol. 104, No. 3, 1986, pp. 395-410.

78. Pierre, C., Tang, D., and Dowell, E., "Localized Vibrations of Disordered Multispan Beams: Theory and Experiment," AIAA/ASME/ASCE/ 27th Structural Dynamics and Materials Conference, San Antonio, TX, May 19-21, 1986.

79. Castanier, M. P., and Pierre, C., "Individual and Interactive Mechanisms for Localization and Dissipation in a Mono-Coupled Nearly Periodic Structure," Journal of Sound and Vibration, Vol. 168, No. 3, 1993, pp. 479-505.

80. Bouzit, D., and Pierre, C., "An Experimental Investigation of Vibration Localization in Disordered Multi-Span Beams," AIAA Paper 93-1487-CP, 1993.

81. Cai, G. Q., and Lin, Y. K., "Localization of Wave Propagation in Disordered Periodic Structures," AIAA Journal, Vol. 29, No. 3, 1990, pp. 450-456.

82. Wei, S., and Pierre, C., "Localization Phenomena in Mistuned Assemblies with Cyclic Symmetry Part II: Forced Vibrations," Journal of Vibrations, Acoustics, Stress, and Reliability in Design, Vol. 110, 1988, pp. 439-449.

83. Yong, Y., and Lin, Y., "Propagation of Decaying Waves in Periodic and Piecewise Periodic Structures of Finite Length," Journal of Sound and Vibration, Vol. 129, No. 2, 1989, pp. 99-118.

84. Kissel, G., "Localization Factor for Multichannel Disordered Systems," Physical Review A, Vol. 44, No. 2, 1991, pp. 1008-1014.

85. Li, D., and Benaroya, H., "Wave Localization in Disordered Periodic Laminated Materials," AIAA Paper, 95-1169-CP, 1995.

86. Xie, W., and Ariaratnam, T, "Numerical Computation of Wave Localization in Large Disordered Beam-Like Lattice Trusses," AIAA Journal Vol. 32, No. 8, 1994, pp. 1724-1732.

87. Xie, W., and Ariaratnam, T, "Wave Localization in Randomly Disordered Nearly Periodic Long Continuous Beams," Journal of Sound and Vibration, Vol. 181, No. 1, 1995, pp. 7-22.

88. Wei, S., and Pierre, C., "Effects of Dry Friction Damping on the Occurrence of Localized Forced Vibrations in Nearly Cyclic Structures," Journal of Sound and Vibration, Vol. 129, No. 3, 1989, pp. 397-416.

89. Langley, R. S., "On the Forced Response of One-Dimensional Periodic Structures; Vibration. Localization by Damping," Journal of Sound and Vibration, Vol. 178, No. 3, 1994, pp. 411-428.

90. Schreiber, E., and Anderson, O. L., "Elastic Constants and their Measurement," McGraw Hill, New York, 1974.

91. Nashif, A. D., Jones, D. I., and Henderson, J. P., "Vibration Damping," Wiley Interscience, 1985.

92. Yew, C., and Chen, C., "Study of Linear Wave Motions Using FFT and its Potential Application to Non-Destructive Testing," International Journal of Engineering Science, Vol. 18, 1980, pp. 1027-1036.

93. Amrane, M., Jezequel, L., and Chaiyaporn, S., "Identification of the Complex Young and Coulomb Moduli of a Sandwich Beam," Materials Chemistry and Physics, Vol. 33, 1993, pp. 266-270.

94. Elishakoff, I., Elisseeff, P., and Glegg, S., "Nonprobabilistic, Convex-Theoretic Modeling of Scatter in material Properties," AIAA Journal, Vol. 32, No. 4, 1994, pp. 843-849.

95. Doyle, J. F., Wave Propagation in Structures, Verlag-Springer, New York, 1989.

96. Reismann, H. and Lee, Y., "Force Motion in Rectangular Plates", Developments in Theoretical and Applied Mechanics, Vol. 4, Pergamon Press, Oxford and New York, 1970.

97. Graff, K., Wave Motion in Elastic Solids, Ohio State University Press, Ohio, 1975.

98. Doyle, J. F. and Kamle, S., "An Experimental Study of the Reflection and Transmission of Flexural Waves at Discontinuities", Journal of Applied Mechanics, Vol. 52, 1985, pp. 669-673.

99. Doyle, J. F. and Kamle, S., "An Experimental Study of the Reflection and Transmission of Flexural Waves at an Arbitrary T-Joint", Journal of Applied Mechanics, Vol. 54, 1987, pp. 136-140.

100. Mace, B. R., "Wave Reflection and Transmission in Beams", Journal of Sound and Vibration, Vol. 97, no. 2, 1984, pp. 237-246.

101. Atkins, K. J. and Hunter, S. C., "The Propagation of Longitudinal Elastic Waves Around Right-Angled Corners in Rods of Square Cross-Section", Quarterly Journal of Mechanics and Applied Mathematics", Vol. 28, 1975, pp. 245-260.

102. Lee, J. P. and Kolsky, H., "The Generation of Stress Pulses at the Junction of Two Noncollinear Rods", Journal of Applied Mechanics, Vol. 39, pp. 809-813.

103. Ripperger, E. A. and Abramson, H. N., "Reflection and Transmission of Elastic Pulses in a Bar at a Discontinuity in Cross Section", Proceedings of the Third Midwestern Conference on Solid Mechanics, pp. 135-145.

104. Desmond, T. P., "Theoretical and Experimental Investigation of Stress Waves at a Junction of Three Bars", Transactions of the ASME, Vol. 48, 1981, pp. 148-154.

105. Anagnostides, G., "Frame Response to a Harmonic Excitation, Taking into Account the Effects of Shear Deformation and Rotatory Inertia", Computers and Structures, Vol. 24, no. 2, 1986, pp. 295-304.

106. Cheng, F. Y., "Vibrations of Timoshenko Beams and Frameworks", Journal of Structural Division, ASCE, Vol. 96, 1970, pp. 551-571.

107. Cheng, F. Y., "Dynamic Matrix of Timoshenko Beam Columns", Journal of Structural Division, ASCE, Vol. 99, 1973, pp. 527-549.

108. Spyrakos, C. C. and Beskos, D. E., "Dynamic Response of Frameworks by Fast Fourier Transform", Computers and Structures, Vol. 15, no. 5, 1982, pp. 495-505.

109. Gopalakrishnan, S., Martin M. and Doyle, J. F., "A Matrix Methology for Spectral Analysis of Wave Propagation in Multiple Connected Timoshenko Beams", Journal of Sound and Vibration, Vol. 158, no. 1, 1992, pp. 11-24.

110. Farris, T. N. and Doyle, J. F., "Wave Propagation in a Split Timoshenko Beam", Journal of Sound and Vibrations, Vol.130, no. 1, 1989, pp. 137-147.

111. Stephen, N. G., "On the Variation of Timoshenko's Shear Coefficient with Frequency", Journal of Applied Mechanics, Vol. 45, 1978, pp. 695-697.

112. Cowper, G. R., "The Shear Coefficient in Timoshenko's Beam Theory", Journal of Applied Mechanics, Vol. 33, 1966, pp. 335-340.

113. Yoshimura, M., "Computer Aided Design Improvement of Machine Tool Structure Incorporating Joint Dynamics Data," Annals of the CIRP, Vol. 28, 1979, pp. 241-246.

114. Yoshimura, M., "Measurement of Dynamic Rigidity and Damping Property for Simplified Joint Models and Simulation by Computer," Annals of the CIRP, Vol. 25, 1977, pp. 193-198.

115. Bert, C. W., and Stricklin, J. D., "Comparative Evaluation of Six Different Numerical Integration Methods for Nonlinear Dynamic Systems," Journal of Sound and Vibration, Vol. 127, No. 2, 1988, pp. 221-229.

116. Gelb, A. and Vander Velde, W. E., "Multiple Input Describing Functions and Nonlinear Systems Design", McGraw-Hill, New York, 1968.

117. Liang, C., Sun, F. P., and Rogers, C. A., "An Impedance Method for Dynamic Analysis of Active Material Systems," Proceedings of the 34th SDM Conference, La Jolla, CA, April, 1993, pp. 3587-3599.

118. Sun, F. P., Liang, C., Rogers, C. A., "Modal Analysis Using Collocated PZT Actuator/Sensor-An Electromechanical Approach," Proceedings of the 1994 North American Conference on Smart Structures and Materials, February, 1994, Orlando, FL.

119. Wang, J., and Sas, P., "A Method for Identifying Parameters of Mechanical Joints," Journal of Applied Mechanics, Vol. 57, June, 1990, pp.-337-342.

120. Green, W. A., "Dispersion Relations for Elastic Waves in Bars," Progress in Solid Mechanics, Vol. 1, 1961, pp. 223-261.

121. Huang, T. C. and Huang C. C., "Free Vibrations of Viscoelastic Timoshenko Beams," Journal of Applied Mechanics, 1971, pp. 515-521.

122. Snowdom, J. C., "Transverse Vibration of Beams with Internal Damping, Rotatory Inertia, and Shear," The Journal of the Acoustical Society of America, Vol. 35, No. 12, 1963, pp. 1997-2006.

123. Henshell, R. D. and Warburton, G. B., "Transmission of Vibration in Beam Systems," International Journal for Numerical Methods in Engineering, Vol. 1, 1969, pp. 47-66.

124. Spyrakos, C. C. and Beskos, D. E., "Dynamic Response of Frameworks by Fast Fourier Transform," Computers and Structures, Vol. 15, No. 5, 1982, pp. 495-505.

125. Graesser, E. J. and Wong, C. R., "The Relationship of Traditional Damping Measures for Materials with High Damping Capacity: A Review," M3D: Mechanics and Mechanisms of Material Damping, ASTM, 1992, pp. 316-343.

126. Tseitlin, A. I. and Kusainov, A. A., "Role of Internal Friction in Dynamic Analysis of Structures," Rotterdam, 1990.

127. Schapery, R. A., "Viscoelastic Behavior and Analysis of Composite Materials," Composite Materials, Vol. 2, Edited by Sendeckyj, G. P., 1974, pp. 85-168.

128. Kinra, V. K. and Yapura, C. L., "A Fundamental Connection Between Intrinsic Material Damping and Structural Damping," M3D Mechanics and Mechanisms of Material Damping, ASTM, 1992, pp. 396-420.

129. Kalyanasundaram, S., Allen, D. H. and Schapery, R. A., "Dynamic Response of the Timoshenko Beam," Mechanics and Materials Center, Texas A&M University, College Station, TX, 1987.

130. Sato, Y., "Analysis of Dispersed Waves by Means of Fourier Transform," Bulletin of Earthquake Research Institute, Vol. 33, 1955, pp. 33-40.

131. Jaime Esteban, Frederic Lalande, Zaffir Chaudhry, and Craig A. Rogers, "Theoretical Modeling of Wave Propagation and Energy Dissipation in Joints," 37th AIAA/ASME/ASCE/AHS/ASC Structures, Structural Dynamics, and Materials Conference, Salt Lake City, UT., April 15-17, 1996.

132. Jaime Esteban, Frederic Lalande, Zaffir Chaudhry, and Craig A. Rogers, "Supporting Results on the Theoretical Modeling of Wave Propagation and Energy Dissipation in Joints," to be published.

133. Wittrick, W., H., and Williams, F. W., "Buckling and Vibration of Anisotropic or Isotropic Plate Assemblies Under Combined Loadings," International Journal of Mechanical Science, Vol. 16, 1974, pp. 209-239.

134. Wittrick, W., H., and Williams, F. W., "A General Algorithm for Computing Natural Frequencies of Elastic Structures," Quarterly Journal of Mechanics and Applied Mathematics, Vol. 24, 1971, pp. 263-284.

135. Entwistle, K. M., "The Damping Capacity of Metals," The Physical Examination of Metals, 2nd ed., B. Chalmers and A. G. Quarrell, Eds. Arnold Limited, London, Chapter 10, 1960.

136. Wren, G. G., and Kinra, V. K., "An Experimental Technique for Determining a Measure of Structural Damping," Journal of Testing and Evaluation, Vol. 16, No. 1, 1988, pp. 77-85.

137. Wren, G. G., and Kinra, V. K., "Modeling and Measurement of Axial and Flexural Damping in Metal Matrix Composites," Mechanics and Mechanisms of Material Damping, ASTM STP 1169, 1992, pp. 282-315.

138. Bishop, J. E., and Kinra, V. K., "Some Improvements in the Flexural Damping Measurement Technique," ," Mechanics and Mechanisms of Material Damping, ASTM STP 1169, 1992, pp. 457-470.

139. Esteban J., Lalande, F., and Rogers, G. A., "Theoretical study of wave localization due to material damping," SPIE's 1996 Symposium on Smart Structures and Materials," Feb. 26-29 1996, San Diego, CA.

140. Esteban J., Lalande, F., and Rogers, G. A., "Study of wave localization due to material damping: Results," to be published.

141. Cremer, L., and Heckl, M., "Structure-Borne Sound," 2nd edition, Heidelberg (Germany), 1988.

142. Okamura, H., Liu, H., Chu, C., and Liebowitz, H., "A cracked column under compression," Engineering Fracture Mechanics, Vol. 1, pp. 547-564, 1969.

Vita

Jaime Esteban was born in Cordoba, Spain on January 30 1969. He graduated from Putnam City High School in June 1987. He began his bachelor degree in Physics at the University of Central Oklahoma, which he completed in May 1990. He then finished his Master degree in Engineering Science and Mechanics at Virginia Polytechnic Institute and State University in December 1992 and he continued his Doctorate program at the department of Mechanical Engineering.